
[All ETDs from UAB](#)

[UAB Theses & Dissertations](#)

1983

A New Model For The Dielectric Breakdown Of Magnesium Oxide Crystals At High Temperatures.

King-Long Tsang
University of Alabama at Birmingham

Follow this and additional works at: <https://digitalcommons.library.uab.edu/etd-collection>

Recommended Citation

Tsang, King-Long, "A New Model For The Dielectric Breakdown Of Magnesium Oxide Crystals At High Temperatures." (1983). *All ETDs from UAB*. 4181.
<https://digitalcommons.library.uab.edu/etd-collection/4181>

This content has been accepted for inclusion by an authorized administrator of the UAB Digital Commons, and is provided as a free open access item. All inquiries regarding this item or the UAB Digital Commons should be directed to the [UAB Libraries Office of Scholarly Communication](#).

INFORMATION TO USERS

This reproduction was made from a copy of a document sent to us for microfilming. While the most advanced technology has been used to photograph and reproduce this document, the quality of the reproduction is heavily dependent upon the quality of the material submitted.

The following explanation of techniques is provided to help clarify markings or notations which may appear on this reproduction.

1. The sign or "target" for pages apparently lacking from the document photographed is "Missing Page(s)". If it was possible to obtain the missing page(s) or section, they are spliced into the film along with adjacent pages. This may have necessitated cutting through an image and duplicating adjacent pages to assure complete continuity.
2. When an image on the film is obliterated with a round black mark, it is an indication of either blurred copy because of movement during exposure, duplicate copy, or copyrighted materials that should not have been filmed. For blurred pages, a good image of the page can be found in the adjacent frame. If copyrighted materials were deleted, a target note will appear listing the pages in the adjacent frame.
3. When a map, drawing or chart, etc., is part of the material being photographed, a definite method of "sectioning" the material has been followed. It is customary to begin filming at the upper left hand corner of a large sheet and to continue from left to right in equal sections with small overlaps. If necessary, sectioning is continued again—beginning below the first row and continuing on until complete.
4. For illustrations that cannot be satisfactorily reproduced by xerographic means, photographic prints can be purchased at additional cost and inserted into your xerographic copy. These prints are available upon request from the Dissertations Customer Services Department.
5. Some pages in any document may have indistinct print. In all cases the best available copy has been filmed.

**University
Microfilms
International**

300 N. Zeeb Road
Ann Arbor, MI 48106

8320601

Tsang, King-Long

A NEW MODEL FOR THE DIELECTRIC BREAKDOWN OF MAGNESIUM
OXIDE CRYSTALS AT HIGH TEMPERATURES

The University of Alabama in Birmingham

PH.D. 1983

**University
Microfilms
International** 300 N. Zeeb Road, Ann Arbor, MI 48106

PLEASE NOTE:

In all cases this material has been filmed in the best possible way from the available copy. Problems encountered with this document have been identified here with a check mark .

1. Glossy photographs or pages _____
2. Colored illustrations, paper or print _____
3. Photographs with dark background
4. Illustrations are poor copy _____
5. Pages with black marks, not original copy _____
6. Print shows through as there is text on both sides of page _____
7. Indistinct, broken or small print on several pages _____
8. Print exceeds margin requirements _____
9. Tightly bound copy with print lost in spine _____
10. Computer printout pages with indistinct print _____
11. Page(s) _____ lacking when material received, and not available from school or author.
12. Page(s) _____ seem to be missing in numbering only as text follows.
13. Two pages numbered _____. Text follows.
14. Curling and wrinkled pages _____
15. Other _____

University
Microfilms
International

A NEW MODEL FOR THE DIELECTRIC BREAKDOWN
OF MgO CRYSTALS AT HIGH TEMPERATURES

by

KING-LONG TSANG

A DISSERTATION

Submitted in partial fulfillment of the requirements for the degree of
Doctor of Philosophy in the Department of Physics
in The Graduate School, University of Alabama in Birmingham

BIRMINGHAM, ALABAMA

1983

ABSTRACT OF DISSERTATION
GRADUATE SCHOOL, UNIVERSITY OF ALABAMA IN BIRMINGHAM

Degree Ph.D. Major Subject Physics
Name of Candidate King-long Tsang
Title A New Model for the Dielectric Breakdown of MgO Crystals at
High Temperatures

The phenomenon of dielectric breakdown of MgO crystals at high temperatures (1500 K) has been investigated with the use of moderate electric fields (1500 V/cm). The effect of various physical parameters associated with the breakdown, such as temperature, various impurity concentrations, sample thickness, electrode material, atmospheric conditions, types of electric field, and electric field strength, have been determined.

The current transients induced by constant and alternating fields as well as by field reversals, and open- and short-circuit conditions are investigated. Activation energies, obtained from the temperature dependence of current parameters, are also obtained. Impurities and their concentrations have been found to play an important role in determining the lifetime of MgO crystals used as an electric insulator at high temperatures.

Inasmuch as the experimental data exclude applications of traditional models to the breakdown of MgO, a new model -- double injection with drift of ionic species or vacancies -- is proposed for the breakdown of MgO crystals at high temperatures. This model provides an excellent explanation of the main features of the experimental results.

Abstract Approved by: Committee Chairman

T. J. Toland

Program Director

C. A. Hanson

Date

6/3/83

Dean of Graduate School

D. J. Kozen

TO
MY PARENTS

ACKNOWLEDGEMENTS

The author wishes to express his appreciation to his major advisor Dr. H. Tiit Tohver and his supervisor in the Solid State Division of Oak Ridge National Laboratory, Dr. Yok Chen, for their professional guidance and assistance throughout this study. For the personal encouragement they gave, and the stimulating and friendly atmosphere they provided, I am deeply grateful.

Appreciation is also expressed to the other committee members Dr. John H. Young, Dr. Edward L. Wills, Dr. Ivan A. Brezovich, and Dr. Dimitry Zessermann, and the dean of the graduate school, Dr. Kenneth J. Roozen, for their comments during the preparation of this thesis. Special thanks are given to Dr. Colin A. Pearson, Chairman of the Physics Department, for his encouragement and support during my study at Oak Ridge National Laboratory.

Thanks are also extended to Dr. Marvin M. Abraham, Dr. Frank A. Modine, Dr. John J. O'Dwyer, Dr. Edward Sonder, Dr. J. C. Wang, and Dr. Robert A. Weeks for many pertinent discussions concerning this study. Sincere thanks are also extended to Mrs. Anne M. Keesee for her excellent assistance in typing both the draft and the final copy of the manuscript.

Appreciation is also extended to the staff in the Solid State Division of Oak Ridge National Laboratory for their willingness to help and for an atmosphere of warmth, interest, and encouragement, thus making my stay in the Oak Ridge National Laboratory very enjoyable.

Special gratitude is expressed to my parents and family, especially my wife Jean (Shu-Tz), and to all my friends who have continually supported me with their patience, sacrifices, and encouragement.

Finally, appreciation is extended to the Graduate School for the fellowship provided during the past years which has enabled me to more effectively concentrate my efforts on my research.

This research is sponsored by the Division of Materials Sciences, U.S. Department of Energy under contract W-7405-eng-26 with Union Carbide Corporation.

TABLE OF CONTENTS

	page
ABSTRACT	ii
ACKNOWLEDGEMENT	iii
LIST OF TABLES	vii
LIST OF FIGURES	viii
 Chapter	
1 INTRODUCTION	1
2 THEORY REVIEW	4
2.1 Conduction Mechanisms	4
2.1.1 Ionic Conduction	4
2.1.2 Current Injection	5
a) One-Carrier Injection	5
b) Double Injection	11
2.1.3 Field Emission	12
2.1.4 Schottky Emission	13
2.1.5 Impurity Conduction	13
2.2 Breakdown Mechanisms	14
2.2.1 Thermal Breakdown	14
2.2.2 Intrinsic Breakdown	18
2.2.3 Avalanche Breakdown	20
a) Field Emission	20
b) Forty-Generations	21
c) Avalanche-Enhanced Cathode Emission	22
2.2.4 Space-Charge-Enhanced Breakdown	22
3 EXPERIMENTAL PROCEDURES	26
3.1 Sample Preparation	26
3.1.1 Sample for Current Measurement	30
3.1.2 Sample for Potential Profile Measurement	30
3.2 Measurement System	30
4 EXPERIMENTAL RESULTS	36
4.1 Nickel Doped and Undoped MgO Crystals	36

TABLE OF CONTENTS (continued)

Chapter	page
4.1.1 Current Behavior	36
a) Field Reversal	37
b) Instantaneous Current after Time Interval with $E=0$.	44
c) Short-Circuit Current	47
d) Alternating Electric Field	49
4.1.2 Activation Energy	51
a) Time Constants of $I(t)$	51
b) Short-Circuit Current	53
c) Alternating Current	53
4.1.3 The Effect of Sample Thickness	53
4.1.4 Field Strength Effect	57
4.1.5 Current-Voltage Characteristics	61
4.1.6 Potential Profile	66
a) An As-Grown $MgO:Ni$ Sample	66
b) Field Reversal	71
4.1.7 Atmospheric Effect	74
4.1.8 Electrode Effect	79
4.2 Other Doped MgO Crystals	82
4.2.1 Effect of Impurity on Breakdown	82
4.2.2 Effect of Impurity Concentrations	82
a) Suppression of Breakdown: Cu and Co	84
b) Enhancement of Breakdown: Cr and Ni	84
4.2.3 Current Behavior	88
a) Field Reversal	88
b) Reversed Current	94
4.2.4 Activation Energy	95
5 DISCUSSION AND CONCLUSION	98
5.1 Comparison with the Existing Models	98
5.2 A New Model for the Dielectric Breakdown of MgO Crystals at High Temperatures	100
5.3 Summary	108
5.4 Suggestions for Future Work	108
APPENDIX A	110
LIST OF REFERENCES	114
VITA	121

LIST OF TABLES

Table		Page
3.1	Impurity concentrations of MgO crystals obtained by neutron activation analysis.	27
3.2	The relationship between impurity concentration and optical absorption of coefficient, $n = c\alpha$, in doped MgO crystals, where n is the concentration of dopant impurity, α the optical absorption coefficient, and c constant.	28
4.1	The current levels at which the potential profiles were obtained for an as-grown MgO:Ni crystal. The curve number corresponds to that shown in Fig. 4.19.	67
4.2	The current levels at which the potential profiles were obtained after the reversal of the applied voltage. The sample is the same as mentioned in Table 4.1. The curve number corresponds to that shown in Fig. 4.21.	72
4.3	The characteristic times for breakdown, t_c , of MgO crystals in different atmospheres. The measurements were performed at 1473 K using an electric field of 1500 V/cm.	78
4.4	The characteristic times for breakdown, t_c , and the activation energies, Q , of MgO:Ni crystals using different electrode material. The measurements were performed at 1473 K using an electric field of 1500 V/cm in flowing dry nitrogen atmosphere.	81
4.5	Characteristic times for the breakdown of MgO crystals at 1473 K and 1500 V/cm. Column 2 corresponds to the concentration of dopants tabulated in column 1. Column 3 lists the characteristic times for breakdown in the first cycle, while column 4 tabulates subsequent characteristic times which had reached to a minimum value.	93
4.6	Activation energies for the breakdown of MgO crystals. Activation energies shown were measured by three methods, short-circuit current I_{SC} , time constant τ_2 , and alternating current I_{AC}	97

LIST OF FIGURES

Figure		Page
2.1	The Lampert triangle showing limiting current-voltage relationship for space-charge-limited current in an insulator (ref. 44).	10
2.2	Diagram of notation for infinite dielectric slab. . .	17
2.3	Field strength varying across the dielectric. The increase of field strength near cathode is due to the drift of holes (ref.71).	24
3.1	Diagram of sample configuration for the measurement of potential profile.	31
3.2	Photograph of MgO:Ni sample prepared for the measurement of potential profile. Five individual Pt wires were wrapped around the central part of the sample.	32
3.3	Sample holder and electrode configuration.	33
3.4	Circuit diagram for the experiment of the dielectric breakdown.	35
4.1	Current vs time at 1473K with $E = 1500$ V/cm applied to a MgO:Ni crystal for several polarity reversals. At $t = 31$ h, fuse was burned out at $I \sim 35$ mA; field was reapplied after 13 h. Upon reapplication of the same field, less time is required to reach a certain current level if the time interval without the field is short.	38
4.2	Characteristic time for breakdown vs the nth field reversal.	40
4.3	Log of current vs time. The current was obtained after 10th field reversal. The line associated with τ_1 was obtained by subtracting the line associated with τ_2 from the original curve.	41
4.4	Current behavior when the field is reversed at different stages of a given cycle.	43

LIST OF FIGURES (continued)

Figure		Page
4.5	Current behavior after a time increment without field ($\Delta t_{E=0}$). The instantaneous current I_i is the current obtained immediately (< 1 sec) after reapplication of the field, either in the same or reversed direction.	45
4.6	Instantaneous current, I_i , as a function of time interval without field, $\Delta t_{E=0}$, for three different initial currents.	46
4.7	Top curve: Instantaneous current vs $\Delta t_{E=0}$. Bottom curve: Short-circuit as a function of time.	48
4.8	(a) Five points along a typical current curve before and after the field reversal. (b) Short-circuit current vs time. Those currents were measured at points shown in (a).	50
4.9	Current vs time with application of alternating field for (a) an as-grown MgO:Ni crystal, and (b) a similar crystal having experienced a current increase due to a dc field.	52
4.10	Log of the time constants τ_1 and τ_2 were plotted against $1000/T$. The activation energies determined from the slopes for τ_1 and τ_2 were 3.7 ± 0.3 eV and 2.3 ± 0.2 eV, respectively.	54
4.11	Log of the short-circuit current vs $1000/T$ for both MgO:Ni and nominally pure MgO crystals. Activation energy 2.4 ± 0.1 eV was obtained.	55
4.12	Log of the alternating current vs $1000/T$ for MgO:Ni crystal. Constant field 1500 V/cm (rms) was used. Activation energy 2.4 ± 0.1 eV was calculated from the slope.	56
4.13	Time constant τ_2 vs sample thickness.	58
4.14	Time required for current to reach 18 mA vs sample thickness.	59
4.15	Time constant τ_2 vs electric field strength. The measurements were made on as-grown MgO:Ni crystals.	60
4.16	Time constant τ_2 vs electric field strength. The measurements were performed after 10th field reversal. Two temperatures 1473 and 1673 K were used.	62

LIST OF FIGURES (continued)

Figure		Page
4.17	I-V characteristics of a MgO:Ni crystal. The sample was treated at 1473 K using an electric field of 200 V/cm. The I-V measurements were performed at various stages during treatment.	63
4.18	I-V characteristics of a MgO:Ni crystal after a constant current of 1 mA for the first 5 h and then 10 mA for another 15 h had been applied to the crystal.	65
4.19	Potential profiles of MgO:Ni crystal at 1475 K using an electric field of 1000 V/cm. The profiles were measured at various stages during the current growth. The current levels at which the measurements were made were shown in Table 4.1.	68
4.20	Residual potential profiles after the removal of the applied field. The top curve was measured when the field was removed at $I = +1.15$ mA. The lower three curves were measured at 0, 40 sec, and 30 min after the removal of the field when current reached +18 mA.	70
4.21	Potential profiles after the field reversal. The profiles were measured after the field was reversed at $I = 18$ mA. The current levels at which measurements were made were shown in Table 4.2.	73
4.22	Residual potential profiles measured after $I = -3.7$ mA. The profiles were measured at 0, 20 sec, 1.5 min, and 20 min after the field removal.	75
4.23	Residual potential profiles measured after $I = -17.5$ mA. The profiles were measured at 0, 40 sec, 1 min, and 20 min after the field removal.	76
4.24	The effect of atmospheric conditions on the current behavior of MgO:Ni crystals. The log of current is plotted vs time. Three different atmospheres were used: pure oxygen, pure nitrogen, and air.	77
4.25	The effect of electrode material on the current behavior of MgO:Ni crystals. Samples were treated at 1473 K with the use of an electric field of 1500 V/cm in flowing dry N_2 . Four different electrodes were investigated: Ir, Graphite, Rh, and Pt.	80

LIST OF FIGURES (continued)

Figure		Page
4.26	Current vs time at $T = 1473$ K with $E = 1500$ V/cm applied to doped and undoped MgO crystals. Crystals with V, Fe, or Ni have lower characteristic time for breakdown than the undoped one, but the crystals doped with Co, H, or Cu have higher characteristic time for breakdown.	83
4.27	Log of the characteristic time for breakdown of MgO:Cu crystals vs dopant concentration.	85
4.28	Log of the characteristic time for breakdown of MgO:Co crystals vs dopant concentration.	86
4.29	Log of the characteristic time for breakdown of MgO:Cr crystals vs dopant concentration.	87
4.30	Log of the characteristic time for breakdown of MgO:Ni crystals vs dopant concentration.	89
4.31	Current vs time at 1473 K with $E = 1500$ V/cm applied to MgO:Cu (30 ppm) crystal for several polarity reversals.	91
4.32	Log of the characteristic time for breakdown vs the nth field reversal for doped and undoped MgO crystals.	92
4.33	The behavior of the first reversed currents of doped and undoped MgO crystals. The applied field was reversed at $I = 18$ mA.	96
5.1	(a) Thermal equilibrium of charge carriers. The dielectric contains n_0 relatively mobile-free electrons, and an equal number of p_0 of high immobile (trapped) holes. (b) Diagram of notations used in the injection model. The injection rates of the charge carriers from the electrodes are denoted as n_i for electrons and p_i for holes. Charge carriers are driven out of the dielectric with drift rates of n_d for electrons and p_d for holes.	103

Chapter 1

INTRODUCTION

Dielectric breakdown is a subject which has received considerably less attention than its technological and scientific importance warrants. In ionic insulators, which are the subject of this research, breakdown at room temperature takes place only under very high applied electric fields. However, as the temperature increases breakdown begins to occur at relatively low applied fields (72). This poses a serious materials problem in certain applications such as energy conversion devices (41), which generally work more efficiently at elevated temperatures. From a fundamental viewpoint, there is no generally accepted model of breakdown. One reason for this is the lack of consistent, reproducible experimental data on which theories could be based. The lack of work in this area has left a large gap in our understanding of dielectric breakdown.

The research that has been performed here involved the dielectric breakdown of MgO crystals at elevated temperatures. MgO crystals were chosen as a prototype refractory material for an investigation on breakdown, because of the availability of well-characterized high-quality crystals and the simple crystal structure.

As a group the alkali halides have received the most attention although there is no evidence that the breakdown process is simplest and therefore more easily understood in these materials than other materials.

In spite of this interest there is currently no completely satisfactory theory for the dielectric breakdown even in the case of alkali halides. A partial reason for this is that most measurements have been made at or near room temperature using high electric field (~ 1 MV/cm). Under these conditions the breakdown occurs very rapidly -- in microseconds (11-14,27-30, 84,93). Consequently, it is experimentally difficult to monitor the rapid increase in electrical current and other physical factors which lead to the breakdown. In the present experiment the measurements are made at elevated temperatures using an electric field which is small enough that the breakdown process occurred slowly and can be monitored in detail.

In the case of refractory materials such as MgO crystals, there are very few suggested mechanisms for breakdown. Lewis and Wright (51,52) studied MgO at moderate temperatures (~ 800 K) using high electric fields (~ 1 MV/cm) and suggested that the breakdown might correspond to the onset of trap-filled, space-charge controlled conduction. Sonder et al. (85) suggested that the breakdown which occurs at 1500K under moderate electric fields (~ 1500 V/cm) is due to conductivity increase along pathways of $a\langle 100 \rangle$ dislocations and small-angle grain boundaries. However, Narayan et al. (70) suggested that those $a\langle 100 \rangle$ -type loops may be a reflection of a large concentration of vacancies generated by the electric current. The idea of current pathways along $a\langle 100 \rangle$ dislocations was ruled out by field reversal experiments (94). Apparently, there is no acceptable mechanism which is applicable to the breakdown of MgO crystals.

In Chapter 2, the conduction mechanisms as well as the breakdown models, which have been suggested, are briefly discussed. Conduction

mechanisms such as ionic conduction, current injection, field emission, Schottky emission, and impurity conduction are discussed, because they may be involved in the breakdown process of MgO crystals. Three basic breakdown models, thermal, intrinsic, and avalanche breakdowns have been suggested for the breakdown of dielectrics. Those models are discussed and will be compared with the observed breakdown phenomena of MgO crystals at high temperatures.

The experimental procedure used in this research is described in Chapter 3. Several physical parameters governing the breakdown are identified and their effects are investigated individually. The experimental results related to those parameters are described in Chapter 4.

In Chapter 5, the experimental results are discussed in terms of the existing breakdown models. None of existing models can explain the observed breakdown phenomenon. A new model is proposed, which offers excellent explanations of most of the experimental results.

Chapter 2

THEORY REVIEW

The conduction and various possible breakdown mechanisms have been reviewed by O'Dwyer (72). Some of the conduction mechanisms, which are of interest in the present study, and all the the existing breakdown mechanisms will be briefly discussed in this chapter. The experimental results of the dielectric breakdown of MgO crystals will be discussed in terms of these mechanisms in Chapter 5.

2.1 Conduction Mechanisms

The conductivity of a dielectric may be either ionic, electronic or a combination of both (16,57-60,73,74,81-83,89). It is difficult to separate these components experimentally, but the basic theoretical ideas are quite distinct. Several possible conduction mechanisms, such as ionic conduction, current injection, field emission, Schottky emission, and impurity conduction, are briefly described next.

2.1.1 Ionic Conduction

In bulk material, ionic conduction is due to the migration of positive or negative ions under the influence of an applied electric field. The basic theoretical expression for all electrical conductivity is

$$\sigma = \sum_i n_i z e_i \mu_i \quad , \quad (2.1)$$

where n_i is the density of the i th species, and ze_i and μ_i the corresponding charges and mobilities. The ionic mobility and concentration of charge carriers are usually influenced by the applied field. Experimentally, the low-field ionic conductivity is temperature dependent and follows an Arrhenius-type law

$$\sigma = \sigma_0 \exp(-\Phi/k_0T) \quad (2.2)$$

where σ_0 and Φ are experimentally determined--usually constant within a given range of temperature, k_0 is the Boltzmann constant, and T the absolute temperature.

The ionic mobility is related to its diffusion coefficient D_i through the Nernst-Einstein relationship

$$\mu_i = zeD_i/k_0T. \quad (2.3)$$

The ionic conductivity can then be written as(42)

$$\sigma = \sum_i n_i z^2 e_i^2 D_i / k_0 T \quad (2.4)$$

2.1.2 Current Injection

The theory of current injection into solids was initiated by Mott and Gurney (66) and Rose (77,78), and further developed and reviewed by Lampert (44-47) and Lampert and Mark (48). Some of the basic results are described below.

a) One-Carrier Injection

A one-carrier injection current is a space-charge-limited current since each injected carrier contributes one excess electronic charge, negative for electrons and positive for holes, to the insulator. With

an ohmic contact, an electron or hole can be injected from metal into the conduction or valence band of insulator. The injected current which can flow through the insulator is limited by the injected space charges and reduced by the trapping sites (48).

Consider the problem as one dimensional and the electron as the injected charge carrier. The results are the same for injected hole. Assume that the electrons are injected at $x=0$ (cathode), and exit at $x=L$ (anode). The current is composed of two components, drift current and diffusion current, and is independent of position x , i.e.

$$J = en\mu E - eD(dn/dx), \quad (2.5)$$

and

$$\vec{\nabla} \cdot \vec{J} = dJ/dx = 0 \quad (2.6)$$

where \vec{J} is the current density, n charge carrier density, μ the mobility of charge carrier, E the applied electric field, and D the diffusion coefficient.

The Poisson equation can be written as (48)

$$(\epsilon/e)(dE/dx) = (n - n_0) + \sum_j (n_{tj} - n_{tj,0}) \quad (2.7)$$

where j denotes the j th set of traps. Here $n = n(x)$ and $n_{tj} = n_{tj}(x)$ are the actual, spatially varying free electron concentration and trapped electron concentration in the j th set of traps, respectively, and n_0 , $n_{tj,0}$ are the corresponding constant, thermal equilibrium values in the bulk, respectively.

The problem is further simplified by two assumptions: (i) The diffusion currents are neglected, and (ii) the cathode has an infinite

reservoir of electrons available for injection. The first assumption reduces Eq. (2.5) to

$$J = en\mu E \quad , \quad (2.8)$$

and the second assumption introduces an ohmic contact between cathode and insulator, which gives a boundary condition (48)

$$E(0) = 0 \quad . \quad (2.9)$$

For the case of a perfect trap-free insulator with no thermally generated carriers, i.e. n_0 and all the n_{tj} are identically zero, the Poisson equation can be written as

$$(\epsilon/e)(dE/dx) = n \quad . \quad (2.10)$$

Combining Eqs. (2.8) and (2.10), one obtains

$$E(dE/dx) = J/\epsilon\mu \quad . \quad (2.11)$$

With the boundary condition Eq.(2.9), Eq.(2.11) can be integrated to give

$$E(x) = (2J/\epsilon\mu)^{1/2}x^{1/2} \quad (2.12)$$

and

$$V(x) = \int_0^x E(x)dx = (8J/9\epsilon\mu)^{1/2}x^{3/2} \quad . \quad (2.13)$$

Taking $x=L$ and $V=V(L)$ in Eq. (2.13), one obtains the current-voltage characteristic

$$J = (9/8)\epsilon\mu(V^2/L^3) \quad . \quad (2.14)$$

Equation (2.14) is variously referred to as the trap-free square law, the Mott-Gurney square law, and Child's law for solids.

The above equation is the limiting form of the current-voltage characteristic for an imperfect insulator at applied voltage high enough that the total number of injected electrons (or holes) substantially exceeds the total number of initially empty electron (or hole) traps in the material. It represents the highest one-carrier injection current a given insulator with a given cathode-anode spacing can carry (48). If there are traps inside the dielectrics and the ratio of free to trapped carriers is $\theta = n(x)/n_t(x) < 1$, then Eq. (2.7) reduces to

$$(\epsilon/e)(dE/dx) = (n-n_0)[1+(1/\theta)] \sim (1/\theta)(n-n_0) \quad . \quad (2.15)$$

The current-voltage characteristic becomes (48)

$$J = (9/8)\theta\epsilon\mu(V^2/L^3) \quad . \quad (2.16)$$

The trap-free insulator with thermal free carriers can be considered as a solid free of traps but characterized by a finite conductivity of $\sigma_0 = en_0\mu$. In this case, all the $n_{tj} = 0$ and Eq. (2.7) becomes

$$(\epsilon/e)(dE/dx) = n(x) - n_0 \quad . \quad (2.17)$$

The thermally generated electrons, of concentration n_0 , contribute to the current but not to the space-charge.

Introducing dimensionless variables

$$\begin{aligned} u &= n_0/n(x) = en_0\mu E(x)/J \quad , \\ w &= e^2 n_0^2 \mu x / \epsilon J \quad , \text{ and} \\ v &= e^3 n_0^3 \mu^2 V(x) / \epsilon J^2 \end{aligned} \quad (2.18)$$

in Eqs. (2.8) and (2.17), one gets

$$udu/(1-u) = dw \quad . \quad (2.19)$$

The solution to Eq. (2.19) is

$$w = -u - \ln(1-u) \quad , \quad (2.20)$$

where $u=0$ at $w=0$, corresponding to the boundary condition Eq. (2.9).

The current-voltage characteristic is then shown to be (48)

$$J = \mu(w_a^3/v_a^2)(V^2/L^3) \quad , \quad (2.21)$$

where the subscript a corresponds to $x=L$ in Eq. (2.18).

There are two limiting regimes: (i) Ohm's-law regime ($u_a \sim 1$), when the injection level is small and does not contribute a significant increase of carriers to those generated thermally, and (ii) trap-free, square-law regime ($u_a \ll 1$), when the concentration of thermally generated charge carriers is small compared with that of the injected charge carriers.

Generally, the current-voltage characteristics in dielectrics is described by the Lampert triangle (45), as shown in Fig. 2.1. The lower curve corresponds to Ohm's law for the neutral crystal,

$$J = en_0\mu V/L \quad . \quad (2.22)$$

The actual current-voltage characteristic cannot lie below this curve, since the injection of electrons at the ohmic contact adds additional carriers to those already present thermally.

The upper curve is Child's law given by Eq. (2.14). The vertical curve corresponds to the trap-filled limit (TFL)--all the traps are filled prior to the application of voltage. The actual current-voltage

ORNL-DWG 82-19658

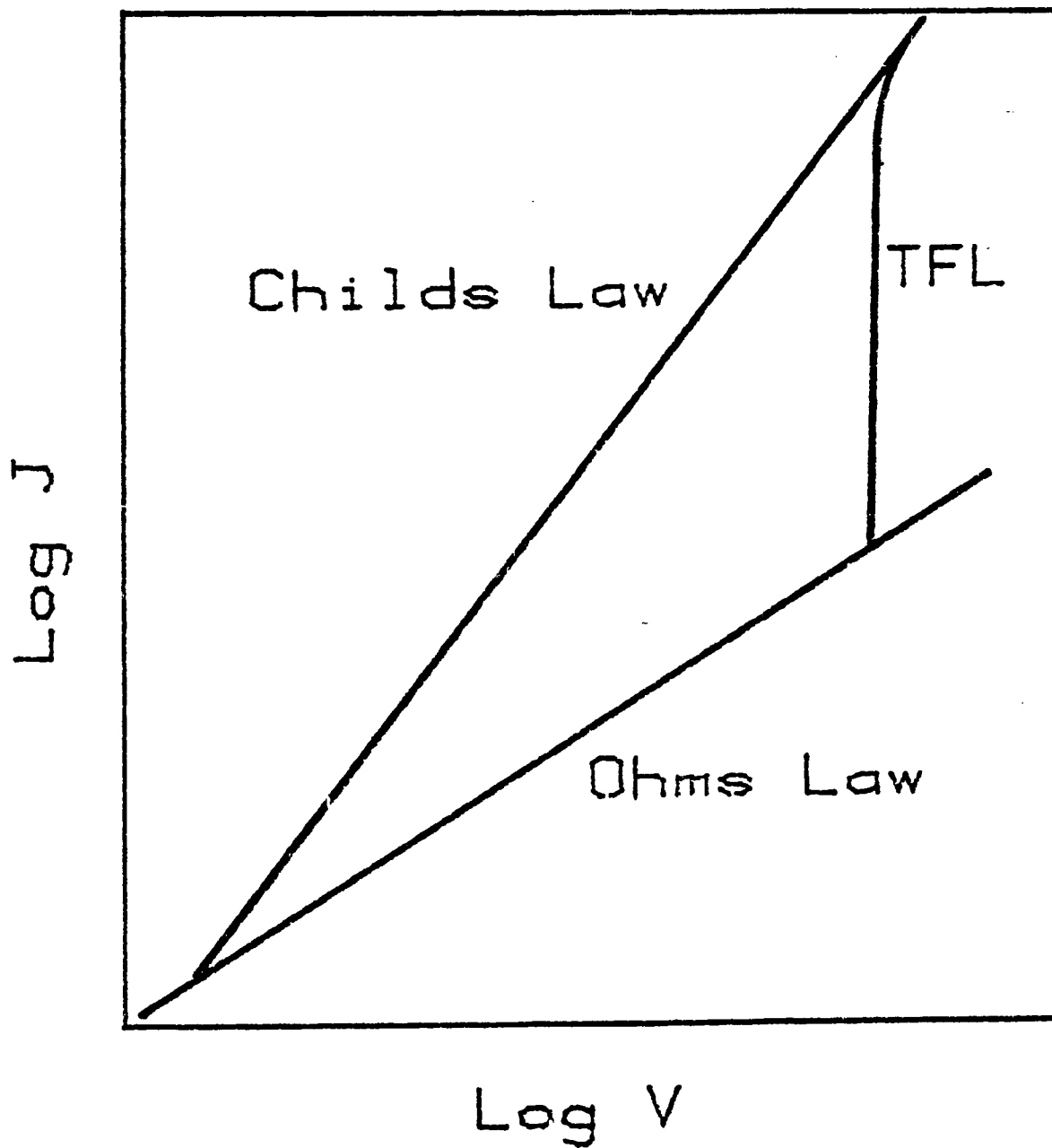


Figure 2.1 The Lampert triangle showing limiting current-voltage relationship for space-charge-limited current in an insulator(ref.44).

curve lies to the left of the trap-filled limit curve, below the Child's law curve and above the Ohm's curve.

b) Double Injection

In the case of double injection, both electrons and holes are simultaneously injected into the insulator from cathode and anode, respectively; the current is much greater than the one-carrier current since the injected electrons and holes can largely neutralize each other's charge. The double injection current is limited by the recombination of electrons and holes either directly from conduction to valence levels, or indirectly via recombination centers. Various aspects of the problem are discussed by Lampert and Mark (48). In the simplest double injection case, the trap-free constant lifetime plasma (49), the current-voltage characteristic has been obtained to be (48)

$$J = (125/8)\epsilon\bar{\tau}\mu_n\mu_p(V^3/L^5) \quad , \quad (2.23)$$

where $\bar{\tau}$ is the common average lifetime for the injected electrons and holes, μ_n and μ_p are their respective mobilities.

The above equation is based on the assumption that the lifetime of either injected charge carriers is longer than its transit time--the time required for the injected charge carrier to travel from one electrode to the other. On the other hand, if the lifetime is shorter than the transit time, the injected carriers will be recombined or annihilated before reaching their opposite electrodes and the insulator departs from the neutral condition. The current becomes space-charge limited, similar to that shown in Eq. (2.14).

In the practical situation, there are trapping centers and recombination centers inside the material. The lifetimes of the injected

carriers vary with the injection level (46,56). A higher injection level gives a longer lifetime of the carrier, since more trapping sites are filled and more carriers can survive in the face of recombination to achieve neutralization. Usually, at the lowest values of electric field the I-V characteristics are simply ohmic since there is no significant number of injected carriers added to that generated thermally. As the injection level increases, the lifetime of the injected carriers increases and the current becomes proportional to the square of the voltage and eventually to the cube of the voltage (56).

2.1.3 Field Emission

Field emission, or the quantum-mechanical tunnelling of electrons from a metal surface into a vacuum under the influence of a strong electric field, was first explained by Fowler and Nordheim (20). This theory was subsequently refined and reviewed by Good and Muller (26), Straton (88), and Lamb (43). The theory was supported by several experimental works (31,50). The field emission was found to be important only when the applied field is sufficiently high. This was shown to be valid by Good and Muller under the condition

$$E > \phi^{1/2} T / 100 \quad , \quad (2.24)$$

where E is the applied field in MV/cm, ϕ is the work function of electron in eV, and T in degrees Kelvin. For field strengths lower than those given by Eq. (2.24) thermionic emission would be expected to dominate. In the breakdown experiment of MgO crystals, $T = 1473$ K, $\phi > 2$ eV, Eq. (2.24) indicates that the emission current (if any) will be primarily thermionic.

2.1.4 Schottky Emission

Schottky emission is thermionic emission from a metal electrode into the conduction band of an insulator, with correction for image forces (17,43,72,76). This mechanism corresponds to the thermal activation of electrons over the metal-insulator interface barrier with the added effect that the applied field reduces the height of this barrier. The emission current is (43,72)

$$J = AT^2 \exp\{-(\phi - \Delta\phi)/k_0 T\} \quad , \quad (2.25)$$

where $A \sim 120 \text{ Amp-cm}^{-2}\text{K}^{-2}$ is the Richardson-Dushman constant, and $\Delta\phi = (e^3 E/\epsilon)^{1/2}$.

The thermionic emission can be also initiated from the colloidal particles in dielectric. The colloidal particles in alkali halides were found to increase the conductivity (35,38,40). This was explained on the basis that those colloids supply electrons to the conduction band by thermionic emission and therefore give rise to enhanced conductivity.

2.1.5 Impurity Conduction

In an impure insulator, an electron can occupy an isolated donor center with an energy slightly below the conduction minimum. When the electron moves between centers without activation into the conduction band, impurity conduction occurs. For low concentration of impurities, the impurity conduction requires the presence of both donor and acceptor centers. The acceptors remove the electrons from the donors. Thus, the electron can either tunnel through the potential barrier from the occupied impurity center to the unoccupied one (55) or jump over the potential barrier from the occupied to unoccupied sites (67). For high concentration of impurities, the interaction between centers is very

large and the conduction can transit from non-metallic to a metallic state (64,65). This is known as impurity band conduction.

2.2 Breakdown Mechanisms

When the temperature (i.e., thermal energy) of the lattice or its electrons reaches a value during the application of an electric field such that the conductivity increases rapidly and results in permanent damage to the material, dielectric breakdown occurs (92). Three basic types of mechanism have been currently suggested for the breakdown of dielectrics. They are thermal, intrinsic and avalanche breakdown. None of these have been found applicable to the breakdown observed in this work. These mechanisms are briefly described as follows:

2.2.1 Thermal Breakdown

All insulators undergo thermal breakdown at a sufficiently high temperature, since the electrical conductivity is usually an exponentially increasing function of the temperature and the thermal conductivity a slowly decreasing function of the temperature. Once breakdown begins, the material is unable to dissipate the heat generated and the breakdown process accelerates. For alternating electric fields the thermal breakdown strength, i.e., the maximum electric field strength the material can withstand before degradation, is lower than the d.c. breakdown strength, since the power loss in a dielectric generally increases with frequency.

The thermal breakdown theory is based on the energy balance between heat dissipated by the sample and the heat generated due to the Joule heating, dielectric losses, and discharges in the ambient. Hence, it is the lattice temperature and not the electron temperature that must reach

a critical level for breakdown to occur. If the heat is mainly generated by Joule heating and the heat-loss is due to thermal conduction, the lattice energy balance is given by

$$C_v \frac{dT}{dt} - \text{div}(k\Delta T) = \sigma E^2 \quad , \quad (2.26)$$

where C_v is the specific heat per unit volume, k is the thermal conductivity, σ is the electrical conductivity, E the field. Assuming there is no charge accumulation, then the current continuity is

$$\text{div}(\sigma \vec{E}) = 0 \quad . \quad (2.27)$$

With a given applied field

$$E = E(t, \vec{r}) \quad , \quad (2.28)$$

the solution of Eqs. (2.26) and (2.27) has the form

$$T = T(t, \vec{r}) \quad (2.29)$$

in which \vec{r} is an arbitrary point in the dielectric. The criterion for breakdown is that T exceeds some assigned critical value.

Because of the complexity of the problem, a general solution of Eq. (2.26) is impossible to address. Some simplified limiting cases have been considered by several authors (9,18,63,96). Most of the considerations have been concentrated on the calculation of the thermal breakdown strength as a function of temperature, sample thickness, etc. Although there is a certain degree of agreement between theoretical calculations and experimental results, we are only interested in the calculation of the maximum thermal voltage which is the applied voltage that a thick dielectric slab can withstand before thermal breakdown takes place (72).

The maximum thermal voltage can help to identify the type of breakdown in MgO crystals.

The maximum thermal voltage can be derived as a certain limiting case (96). An infinite dielectric slab of arbitrary thickness is constrained to the ambient temperature at its bounding electrode surfaces by a sufficient cooling capacity. The thermal insulation of the dielectric is then the limiting factor on the energy dissipation. The notation for the problem is shown in Fig. 2.2, in which z is measured from the central plane at which the temperature is, by symmetry, a maximum T_m . The temperature of the ambient medium is T_0 .

Under the steady-state condition, Eq. (2.26) becomes

$$\frac{\partial}{\partial z} \left(k \frac{\partial T}{\partial z} \right) + \sigma \left(\frac{\partial V}{\partial z} \right)^2 = 0 \quad . \quad (2.30)$$

From the equation of current continuity, we have

$$\sigma \frac{\partial V}{\partial z} = -j \quad . \quad (2.31)$$

The Eqs. (2.30) and (2.31) combine to give

$$\frac{\partial}{\partial z} \left(k \frac{\partial T}{\partial z} \right) - j \frac{\partial V}{\partial z} = 0 \quad . \quad (2.32)$$

Integrating from the center to a variable point, we have

$$jV = \int_0^z \frac{\partial}{\partial z} \left(k \frac{\partial T}{\partial z} \right) dz = k \frac{\partial T}{\partial z} \quad , \quad (2.33)$$

since $\frac{\partial T}{\partial z} = 0$ at the central plane. Substitution for j from Eq. (2.31)

ORNL-DWG 82-19653

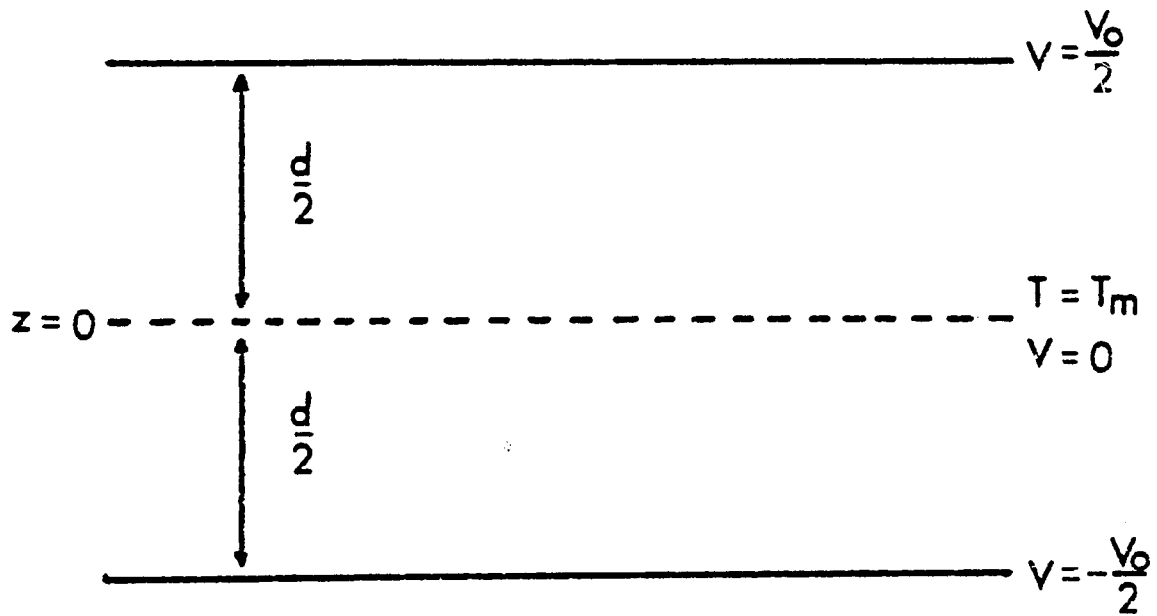


Figure 2.2 Diagram of notation for infinite dielectric slab.

into Eq.(2.33) gives

$$V = - \frac{1}{\sigma} \frac{\partial z}{\partial V} k \frac{\partial T}{\partial z} . \quad (2.34)$$

Using the electrical conductivity

$$\sigma = \sigma_0 \exp(-\phi/k_0T), \quad (2.35)$$

the critical thermal voltage is obtained to be (72)

$$V_{OC} \sim \left(\frac{k k_0 T_0^2}{\sigma_0 \phi} \right)^{1/2} \exp(\phi/2k_0T) , \quad (2.36)$$

assuming that $\phi \gg kT$ for all temperatures considered and $T_{mc} \gg T_0$.

2.2.2 Intrinsic Breakdown

When the applied electric field is sufficiently high such that the electron temperature suddenly reaches a critical value, intrinsic breakdown occurs. Experimentally, intrinsic breakdown occurs at low temperatures and in very short time intervals, approximately less than a microsecond. There is evidence that intrinsic breakdown is electronic in nature.

The name "intrinsic" is used because breakdown by this mechanism is independent of the sample or electrode geometry used (provided no field distortion occurs), or of the wave form applied. Hence, the value of applied field required to cause intrinsic breakdown at a given temperature depends only on the property of the material.

The intrinsic critical field strength is the field strength for which some instability occurs in the electronic conduction current. The first calculation of an intrinsic critical field was given by Zener (98),

who calculated the rate of quantum mechanical tunneling from the valence band to the conduction band in the presence of a strong electric field.

More detailed calculations of the intrinsic critical field strength have considered the conduction-electron energy balance equation. The energy balance equation is

$$A(E,T,\alpha) = B(T,\alpha) \quad , \quad (2.37)$$

where

$A(E,T,\alpha)$ = energy gained by the material from the applied field

$B(T,\alpha)$ = energy dissipated by the material,

T = Lattice temperature (K),

E = Applied field, and

α = Energy distribution parameter, which depends on the model proposed.

Depending on the details of the model, it may then occur that Eq.(2.37) can be satisfied in a physically acceptable manner only for values of E below a certain critical value E_c . This value is regarded as the intrinsic critical field for the particular model being considered (cf. Frolich (21,22), Callen (5) and Frolich and Paranjape (23)). The models proposed by these authors differ from each other in that they consider different mechanisms of energy transfer from the conduction electrons to the lattice, and also by the different assumptions they make concerning the energy distribution of the conduction electrons.

The intrinsic critical field strength for alkali halides have been measured by von Hippel (33), von Hippel and Alger (34), Calderwood and Cooper (4), Cooper et al. (12), Cooper et al. (13,15). The agreement between experimental results and theoretical values is poor.

2.2.3 Avalanche Breakdown

In theories of intrinsic breakdown, the breakdown is due to a sudden increase in the number of conduction electrons as the applied field reaches the critical value. On the other hand, the avalanche breakdown theories consider that the breakdown results from a conduction-electron multiplication process which gradually increases the number of conduction electrons to a limit beyond that the material can tolerate as the field strength rises. Avalanche theories can be classed by their initiation mechanisms which are either field emission or ionization collision (72).

a) Field Emission

The field-emission critical field strength introduced by Zener (98) was based on the probability per unit time that an electron would escape from the valence to the conduction band. He obtained the Fowler-Nordheim type result

$$\begin{aligned} P_{VC} &= (eEa/h)\exp\{-\pi^2maI^2/h^2eE\} \\ &= (0.243 \times 10^7 Ea)\exp\{-3.3 \times 10^6 aI^2/E\} \end{aligned} \quad (2.38)$$

where a is the sample thickness in 10^{-8} cm, h is Planck's constant, m is the electron mass, E is the field strength in V/cm, and I is the energy gap in eV.

When we use the typical magnitudes $a = 3 \times 10^{-8}$ cm, $I = 2$ eV, and let E be the electric field in $V\text{ cm}^{-1}$, Eq.(2.38) becomes

$$P_{VC} = 10^7 E \times 10^{(-2 \times 10^7)/E} \quad (2.39)$$

The dielectric breakdown is thus not to be expected until E reaches the

order of magnitude of 10^6 . In the case of MgO crystals, $a = 2.5 \times 10^{-1}$ cm, $I > 2$ eV, and $E = 10^3$ V/cm, this type of breakdown becomes unrealistic.

b) Forty-Generations

The forty-generations critical field strength is based on a single electron collision-ionization theory developed by Seitz (80) and formulated by Stratton (87).

The simple picture of avalanche formation is described as follows. One electron, initially at the cathode, receives sufficient energy from the applied field to ionize a bound electron. If both of these electrons now receive the same energy from the field, they each cause a further ionization, and eventually 2^i free electrons will be formed if there are i generations between cathode and anode. From the simple argument of Seitz (80), the breakdown will occur when i reaches 40. Assume that the critical field strength is of the order of 10^6 V cm⁻¹ and that the average mobility is of the order of 1 cm²V⁻¹S⁻¹ at this field strength, which means that the electron travels about 1 cm in 1 μ s. During a 1 μ s drift, the electron also wanders in a cylinder of radius 10^{-3} cm. There are about 10^{17} atoms in a tube of a solid 1 cm long and 10^{-3} cm in radius, and energy of the order of 10 eV per atom would disrupt the structure of the material. Assuming that none of the energy supplied by the field is conducted away from the tube thermally, the above data shows that about 10^{18} eV would be required to cause disruption in the tube. With a field of 10^6 V cm⁻¹, this requires an avalanche of 10^{12} electrons, or about forty generations. This is just a very rough analysis. A much more elaborate analysis has been performed

by Stratton (87) who showed that only thirty-eight generations could reach the critical condition.

c) Avalanche-Enhanced Cathode Emission

Critical conditions of another type were considered by Forlani and Minnaja (19). Rather than taking account of the avalanche multiplication resulting from only one electron starting from the cathode, they considered the consequence of avalanche multiplication of the Fowler-Nordheim emission current from the cathode. This model decreases the number of collisions required to reach the breakdown condition.

2.2.4 Space-Charge-Enhanced Breakdown

O'Dwyer has proposed a space charge modified field emission model for avalanche breakdown. His criticism of the single electron or forty-generation model is based on its lack of a continuity of current (71,72). Assuming that the freed electrons and holes occurring after the fortieth collision form a parallel plate capacitor, calculations show that a field of order 10^{11} V cm⁻¹ would be needed to maintain this charge separation. Since such a field strength is far above any reasonable value, he suggests a continuous current model involving cathode field emission with ionization occurring after emission for short breakdown times. The proposed steps in the breakdown process are described as follows (72):

(1) Initially the field strength is uniform across the dielectric and, at a certain critical field, substantial collision ionization begins within the dielectric.

(2) The products of collision ionization are relatively mobile electrons and relatively immobile holes. The holes drift slowly toward

the cathode and their space charge distorts the field, making it stronger near the cathode and weaker near the anode.

(3) The stronger cathode field causes enhanced electron emission, which in turn results in increased collision ionization with consequent further increase in field distortion. This whole sequence of events results in a type of positive feedback situation.

(4) The dielectric is destroyed by massive electron emission from the cathode caused by the greatly enhanced field strength in the vicinity of that electrode.

O'Dwyer has shown that a space charge of low mobility holes is influencing the field distribution, as seen by the drop in field away from the cathode in Fig. 2.3. Comparison of the theoretical results with Al_2O_3 and NaCl thin film breakdown data gives a good agreement. O'Dwyer's model has been supported by the experimental works of Cooper and Elliott (11), and Paracchini (75) on the pre-breakdown light emission of alkali halides.

Cooper and Elliott (11) photographed the pre-breakdown light emission from KBr. They found that no light could be detected earlier than about 20 ns prior to collapse of voltage across the specimen, and thereafter a broad band of light emission composed of several bright cores propagated through the sample from the cathode to the anode. This evidence is considered to be unfavorable to the forty-generation theory and to the avalanche theory of Forlani and Minnaja (19) since these theories both predict the heaviest collision ionization is occurring in front of the anode and the light emission would be expected to begin in that region. On the contrary, Cooper and Elliott (11) believe that conditions first become unstable in the vicinity of the cathode and they

ORNL-DWG 82-19655

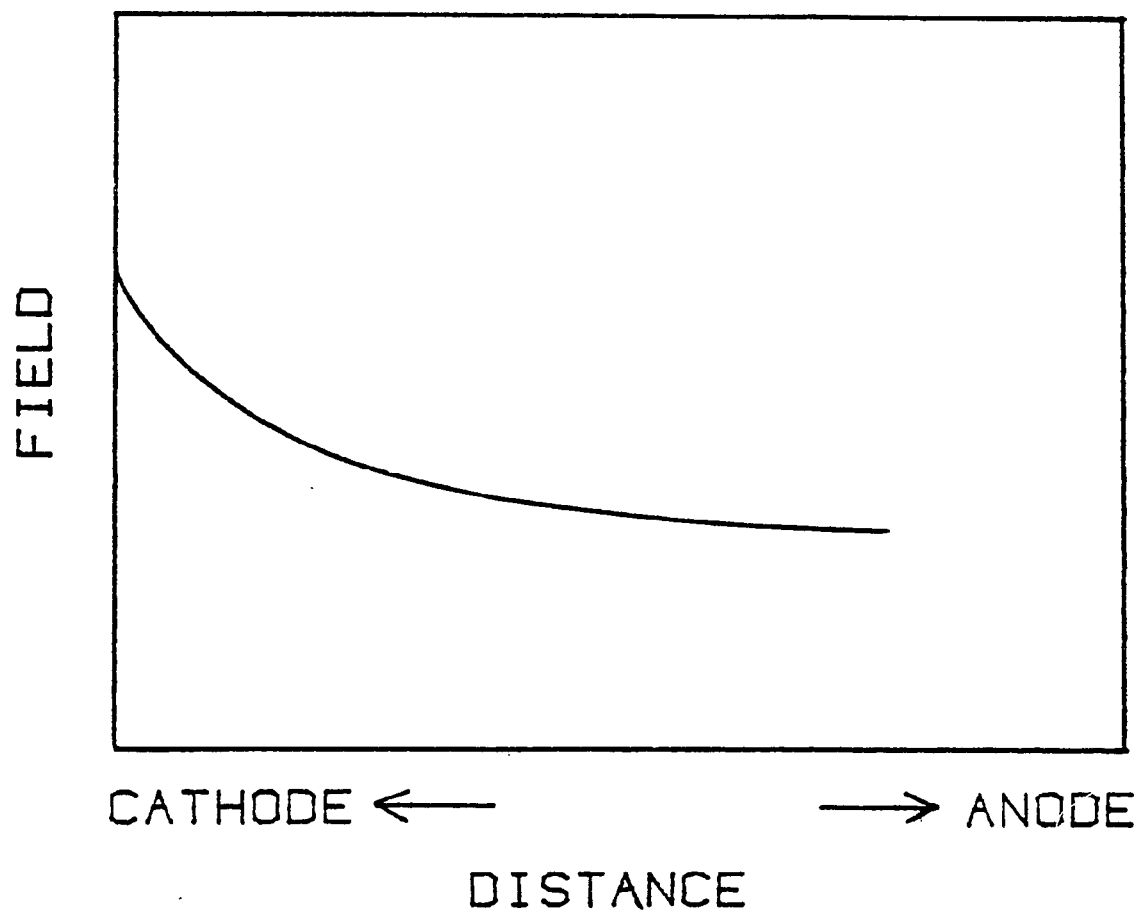


Figure 2.3 Field strength varying across the dielectric. The increase of field strength near cathode is due to the drift of holes (ref.71).

suggested that space-charge enhancement of the cathode field and field emission current leads to breakdown.

However, in the work of impurity and time effects in the electrical breakdown of alkali halides, Hanscomb (29) has found that several experimental facts cannot be explained by O'Dwyer's model, such as the time-dependent breakdown and pre-breakdown current behaviors. The breakdown strength with the long type voltage pulse (8×10^{-3} sec) is greater than that obtained with short type voltage pulse (70×10^{-6} sec). This is contradictory to the ionic space-charge hypothesis which suggests that an increased time of application of voltage will lead to a decreased breakdown strength, since ionic space charge should develop more fully in a longer period of time. Hanscomb has also found that the prebreakdown current is decaying with time, which is not predicted by any of the avalanche theories. Therefore, he suggested that electron or hole transport accompanied by trapping and recombination may be involved in the electrical breakdown of alkali halides (29).

Chapter 3

EXPERIMENTAL PROCEDURES

3.1 Sample Preparation

Crystals used in this work were grown at the Oak Ridge National Laboratory (ORNL) and Tateho Chemical Company. The ORNL crystals, doped and undoped, were grown by the arc-fusion method (1) using high-purity MgO powder from Kanto Chemical Company, Tokyo, Japan. Table 3.1 lists the crystals, the source, and the dopant concentration. They are high quality, transparent, single crystals. The concentration of a dopant has been determined by neutron activation analysis with an accuracy of better than $\pm 5\%$. The total background impurity of undoped MgO crystals is about 100 ppm (1,9). The impurities are primarily Ca at 15 ppm, Al at 10 ppm, and Si at 15 ppm. The MgO:H crystals, grown by presoaking MgO powder with water, were cloudy due to the presence of cavities containing high-pressure H₂ gas (3).

Optical absorption measurements have been made using a Cary 17D spectrophotometer. Typically the absorption coefficient of an impurity band was correlated with the concentration determined by neutron activation analysis for a specific crystal, using the relationship

$$n = c \alpha \quad , \quad (3.1)$$

where n is the dopant concentration, α the peak absorption coefficient of the impurity band(s) and c a constant. The values of c for different impurities and absorption bands are tabulated in Table 3.2. The con-

Table 3.1

Impurity concentrations of MgO crystals obtained by neutron activation analysis.

Sample	Source	Dopant Impurity Concentration (ppm)
MgO	ORNL	undoped
MgO:Co	ORNL	2080
MgO:Cu	ORNL	36
MgO:Ni	ORNL	4280
MgO:Fe	Tateho	1000*
MgO:Cr	Tateho	720
MgO:V	Tateho	350
MgO:H	ORNL	not measured

*This value is given by the manufacturer.

Table 3.2

The relationship between impurity concentration and optical absorption coefficient, $n = c\alpha$, in doped MgO crystals, where n is the concentration of dopant impurity, α the optical absorption coefficient, and c a constant.

Dopant Impurity	n (ppm)	Band Peak (eV)	Optical Absorption Coefficient α (cm^{-1})	Constant C^* ($\text{cm}^{-1}\text{-ppm}$)
Co	2080	2.4 ^a	1.7	6.2×10^{19}
		4.4 ^a	9.4	1.1×10^{19}
Cu	36	4.5	36.0	5.0×10^{16}
		5.5	40.0	4.5×10^{16}
Ni	4280	1.9 ^{a,b}	1.9	1.1×10^{20}
		3.1 ^{a,b}	3.8	5.5×10^{19}
Cr	720	2.8 ^a	1.8	2.0×10^{19}
V	350	2.9 ^c	2.2	8.0×10^{18}
		5.2 ^c	90.0	2.0×10^{17}
Fe	1000	4.3 ^d	---	$1.4 \times 10^{17**}$

*With the exception of Fe-doped MgO crystals, all the C values are based on one sample analyzed by neutron activation energy.

**Calculated from Reference 8.

^areference 54.

^breference 37.

^creference 61

^dreference 86.

centration in all other crystals with the same dopant could then be determined from Eq. (3.1) using this value of c and measured α . This method of determining concentration has been shown to be reliable in the case of Fe-doped MgO crystals (8).

Optical absorption measurements were used to characterize the impurity charge states before and after dielectric breakdown at elevated temperatures. For example, these measurements showed that substitutional Ni^{+2} ions are converted to Ni° metallic precipitates after electrothermal reduction at elevated temperatures (62,90,95).

The results of optical and transmission electron microscopy studies (68) indicate that even in the highly doped MgO:Ni (4280 ppm) crystals, only a very small percentage of the impurity is in precipitate form, and these precipitates are found to be associated with sub-boundaries. Voids and cracks were not observed. The nickel dopant is mostly dissolved as Ni^{2+} ions in the matrix.

The dimensions of sample were chosen such that the surface distance between electrodes was much greater than the thickness and therefore the effect of surface conduction was eliminated. Two types of measurements were carried out - current and potential profile. For current measurements, samples of dimensions $15 \times 15 \times 2.5 \text{ mm}^3$ were usually used except where thickness dependence was investigated. For the measurement of potential profile inside the sample, a thick sample was used in order to have enough measuring points between the electrodes. Therefore, the sample had to be specially prepared such that the problem of surface conduction could be minimized and the value of potential at a given point could be correctly measured without disturbing the electric field.

3.1.1 Sample for Current Measurement

Samples of desired dimensions were prepared by cleaving along {100} planes from single-crystal ingots and abrading on SiC papers. The samples were then etched in hot phosphoric acid maintained at 385 K. This procedure was used to remove the damaged surface layers from which dislocations were known to propagate into the crystal at elevated temperatures (7). Furthermore, an etched surface would provide a good electrical contact.

3.1.2 Sample for Potential Profile Measurement

A rectangular block of MgO:Ni single crystal with dimensions $10 \times 10 \times 5.6 \text{ mm}^3$ was cut by a diamond wafering blade of thickness 0.3 mm at five positions between the two big square faces on which the electrodes were attached. During the cutting, both the crystal and the diamond blade were rotating at the same time so that the crystal was cut in a special shape, as shown in Fig. 3.1. After the cut, the sample with a central cylindrical solid 6.2 mm in diameter and six extended blade-like projections was then etched in phosphoric acid at 330 K for two hours to remove the damaged surface layers. Five individual platinum wires serving as measuring probes were wrapped around the central cylindrical solid, as shown in Fig. 3.2.

3.2 Measurement System

The experimental setup is shown in Fig. 3.3. The sample was sandwiched between two flat circular platinum electrodes with a diameter of 6.3 mm and suspended, with the aid of a set of alumina tubes, in the hot zone of a vertical alumina furnace tube which had one hole on each end to allow circulation of a desired atmosphere.

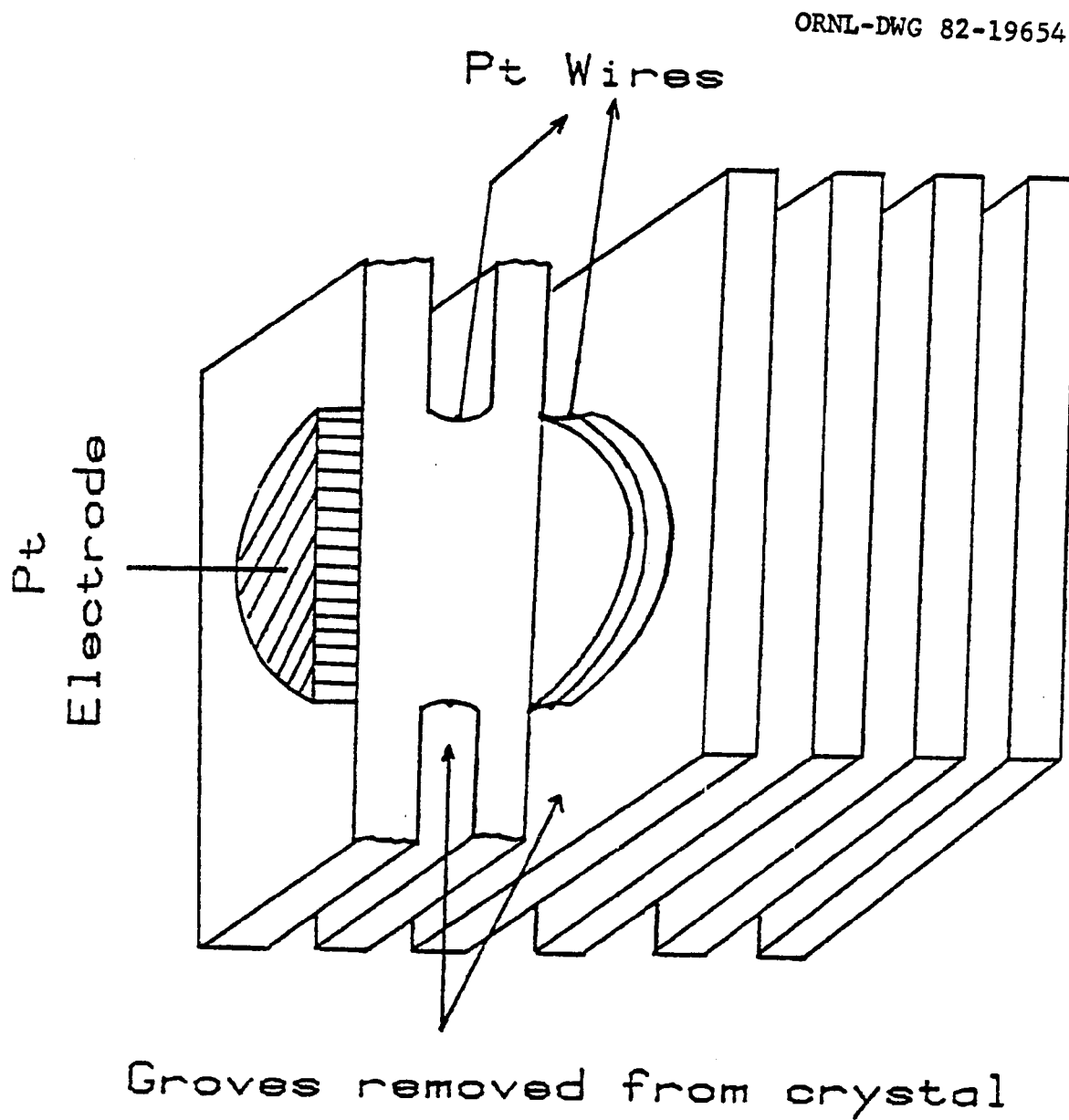


Figure 3.1 Diagram of sample configuration for the measurement of potential profile.

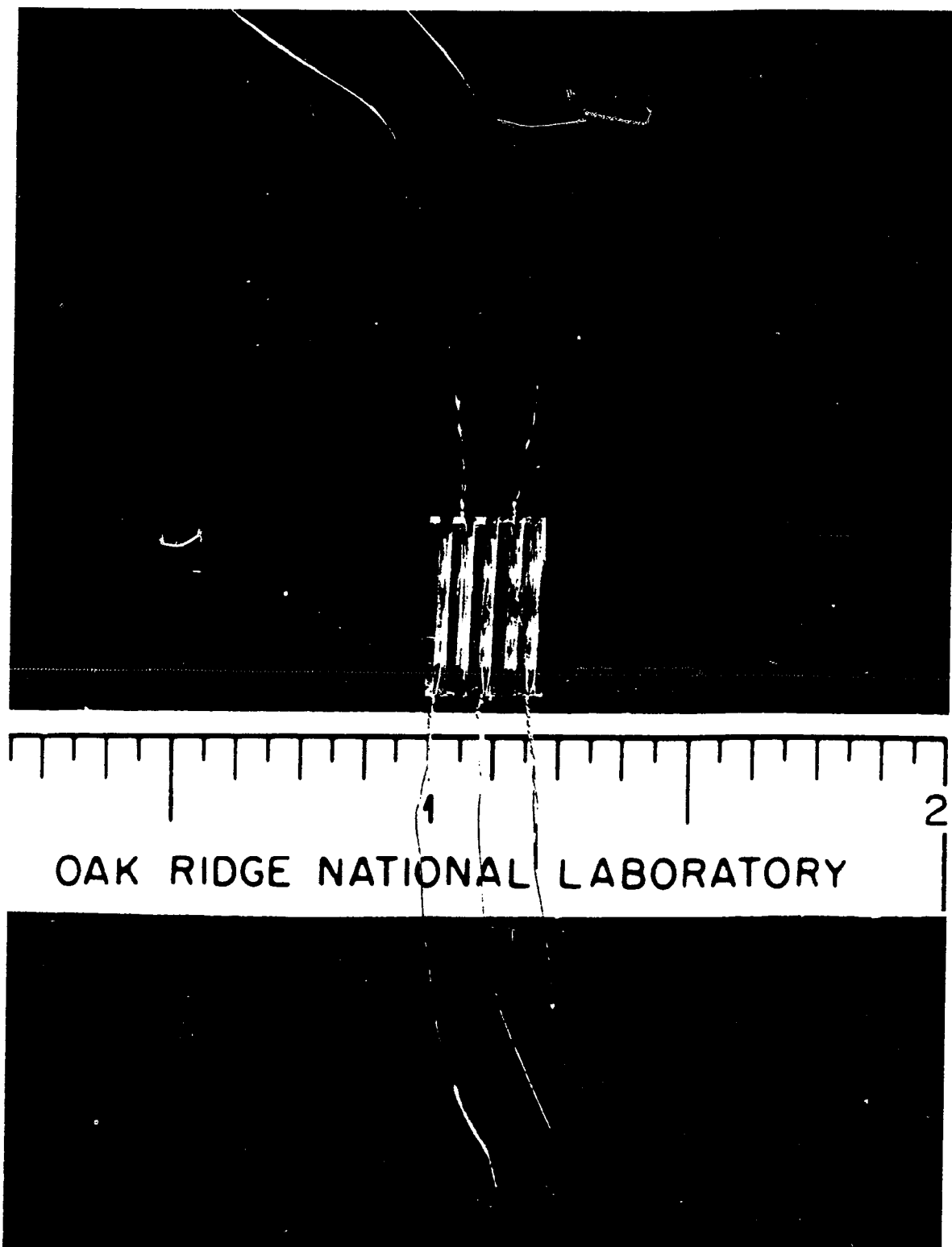


FIGURE 3.2. PHOTOGRAPH OF MgO:Ni SAMPLE PREPARED FOR THE MEASUREMENT OF POTENTIAL PROFILE. FIVE INDIVIDUAL Pt WIRES WERE WRAPPED AROUND THE CENTRAL PART OF THE SAMPLE.

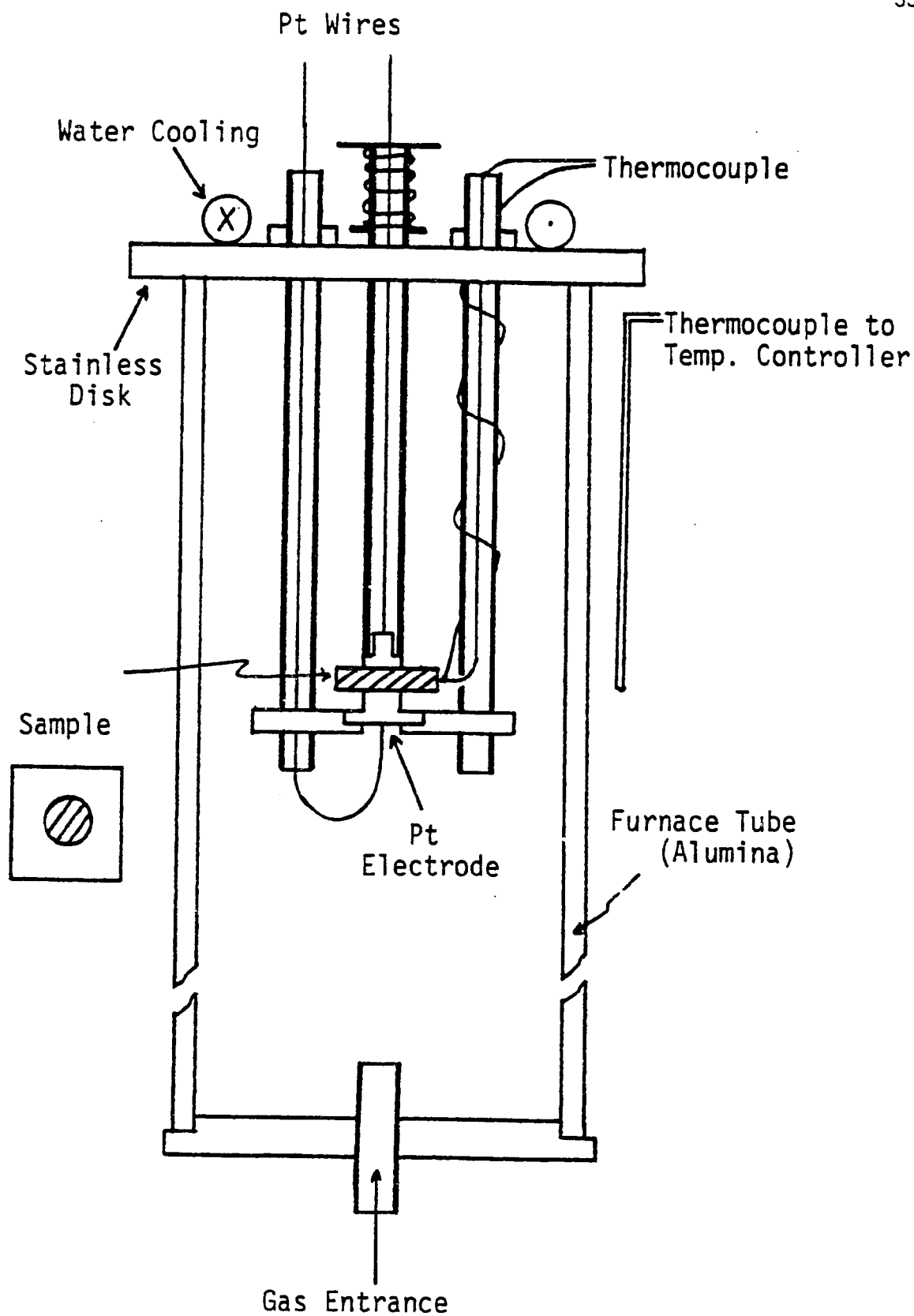


Figure 3.3 Sample holder and electrode configuration.

A Sentry AV electric furnace was used. The furnace temperature was regulated by a Wheelco temperature controller. The temperature was monitored by Pt and Pt (10% Rh) thermocouples and did not fluctuate more than ± 2 K.

The circuit used for this experiment is shown in Fig. 3.4 Both constant and alternating electric fields were used. Constant electric field was provided from a dc power supply (PRL CP-1413-V) and alternating electric field was generated by a line-to-line transformer (STANCOR P-4076) in conjunction with an autotransformer (VARIAC, W5MT3). AC currents were measured with a Valballa 4440 digital multimeter. DC currents were monitored with a Keithley 160B digital multimeter and also recorded by a Varian G-14 strip-chart recorder. A variable resistor R_T was used in conjunction with the recorder to permit proper scaling. A fuse was used to protect the power supply. For the potential profile measurement, a potential divider with a total resistance of $10^9 \Omega$ and a ratio of 1000:1 was connected in parallel with the electrodes to directly measure the value of potential at various points inside the sample.

Pressure contacts using cylindrical platinum rods were used throughout, except that evaporated platinum contacts were used on one occasion and yielded the same results. All measurements were made by the two-probe method. In order to check the effect of surface conduction, a guarded electrode was used and no difference in current behavior was observed.

ORNL-DWG 81-9495

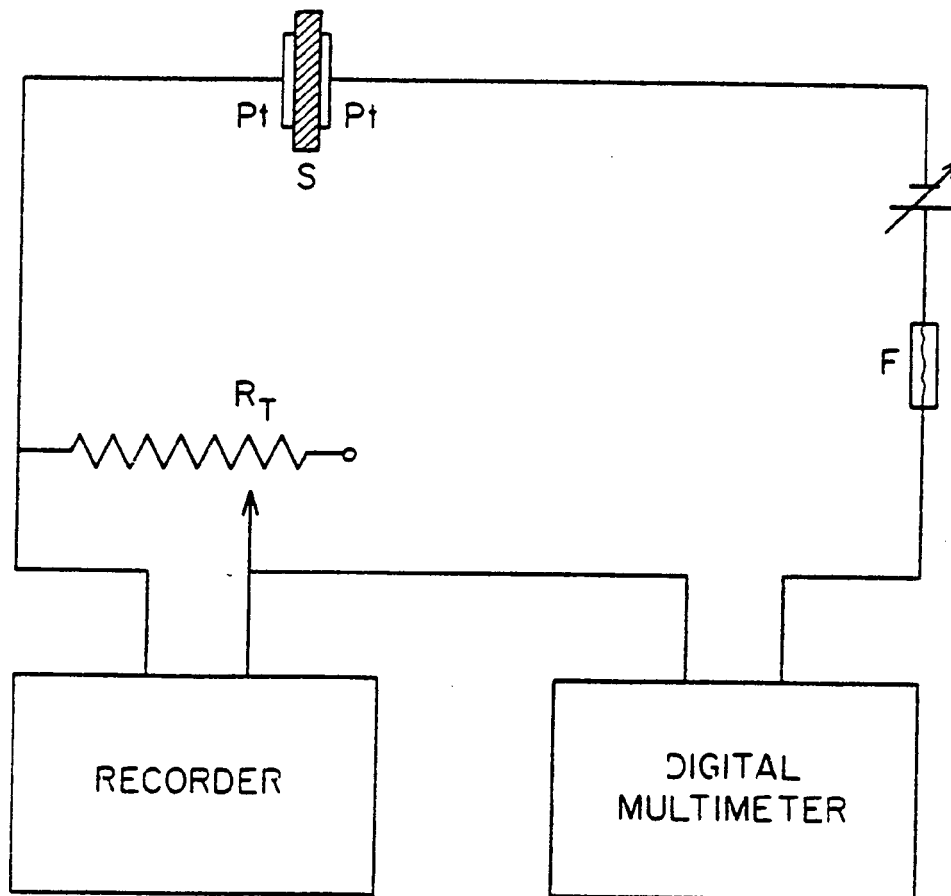


Figure 3.4 Circuit diagram for the experiment of the dielectric breakdown.

Chapter 4

EXPERIMENTAL RESULTS

There are many parameters associated with the breakdown phenomena of dielectrics. Some of the important parameters are temperature, electric field, sample thickness, impurity concentration, atmospheric condition, and electrode material. The experimental procedure was designed to study one parameter at a time and to keep the others constant. Measurements were focused on the prebreakdown phenomena which provide direct information of the breakdown process. The initial study was concentrated on MgO:Ni and undoped MgO crystals; subsequently the work was extended to other doped MgO crystals. The experimental results are described as follows.

4.1 Nickel Doped and Undoped MgO Crystals

4.1.1 Current Behavior

When a moderate dc electric field was applied to a MgO crystal at 1473 K, a slight decrease in current was initially observed. Subsequently, the current increased exponentially until the sample experienced dielectric breakdown and could no longer be used as an electrical insulator. Mostly, the sample was not allowed to proceed to breakdown since this would have destroyed it. When the current reached 18 mA the applied field was removed or reversed, because at this current the breakdown was imminent and the sample temperature would begin to be significantly changed (see APPENDIX A). Therefore, the time required

for the current to reach 18 mA was considered to be the characteristic time for breakdown, t_c . The current behaviors induced by constant and alternating fields as well as by field reversals, and open- and short-circuit conditions are described below.

a) Field Reversal

When an electric field of 1500 V/cm was applied to a sample at 1473K, a current increase over many hours was observed. Typically, when the current reached 18 mA, the field was reversed quickly and the current in the opposite direction was also measured as a function of time. Usually, several field reversals were made and the current behavior of a typical MgO:Ni sample was shown in some detail in Fig. 4.1.

The field was applied at $t = 0$, after the sample had been heated at 1473 K for about 10 minutes (hereafter referred to as min) in order to ascertain that the sample temperature had reached equilibrium. The current initially decreased from 0.20 to 0.10 mA in 40 min (in the top inset of Fig. 4.1), and then increased exponentially until 18 mA was reached and the field was reversed at $t = 18$ hours (hereafter referred to as h). This value, 18 mA, represents a 180-fold increase from the minimum current value. Upon the field reversal, the current flowing in the opposite direction decreased from an initial value, which was slightly less than 18 mA, to a minimum value of 0.7 mA in 25 min (in the lower inset of Fig. 4.1), and then followed by an exponential increase which was faster than that in the first cycle. The characteristic time for this cycle was only 9 h. Several more field reversals were performed subsequently. The current behavior was similar to that of the first reversal, but the characteristic time diminished with each reversal, until ultimately only 2 h were required. It is noteworthy

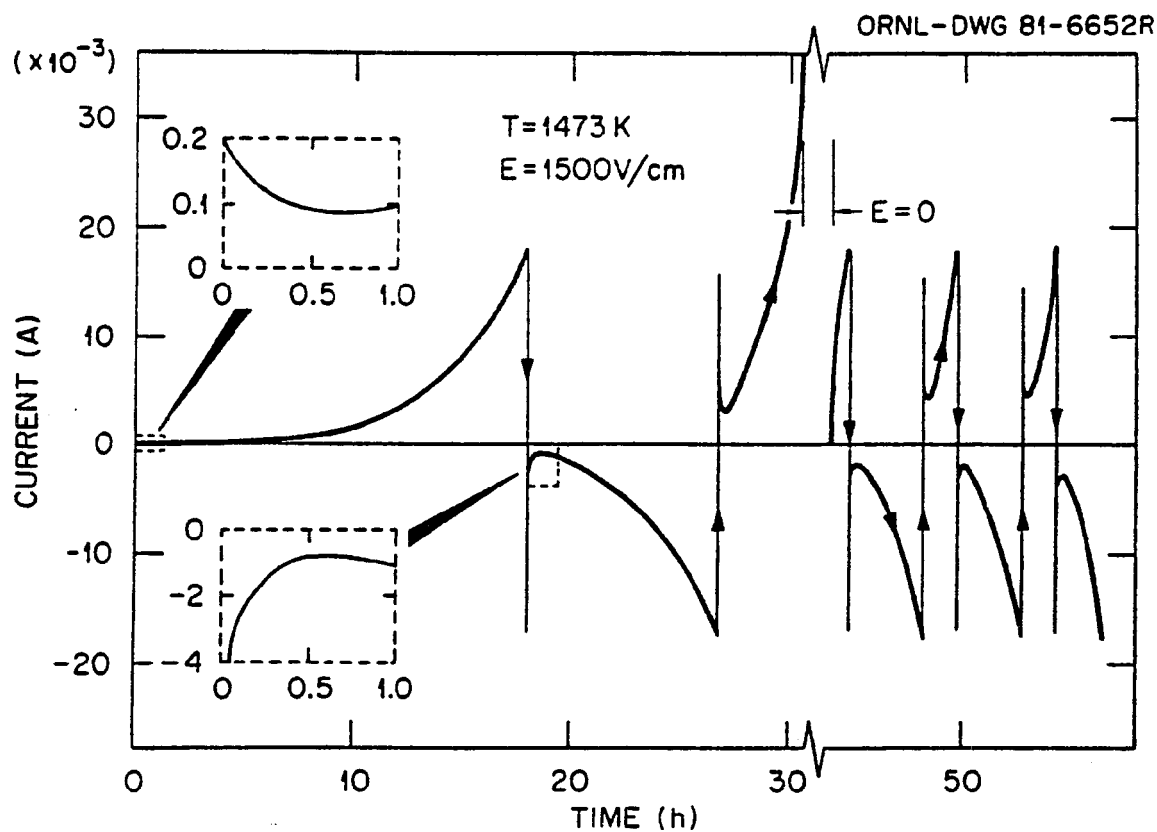


Figure 4.1 Current vs time at 1473K with $E = 1500\text{ V/cm}$ applied to a MgO:Ni crystal for several polarity reversals. At $t = 31\text{ h}$, fuse was burned out at $I \sim 35\text{ mA}$; field was reapplied after 13 h. Upon reapplication of the same field, less time is required to reach a certain current level if the time interval without the field is short.

that current fluctuations were larger in the first cycle than in subsequent reversals, within 5% and 2%, respectively. Figure 4.2 plots the characteristic time as a function of chronological reversals. The characteristic time for one polarity exceeds the other before the tenth reversal, but the decreasing trend is evident. Five other MgO:Ni crystals were studied in a similar fashion. The results were similar to those shown in Figs. 4.1 and 4.2, although the values differed slightly.

The time-dependent currents for each of the reversals can be described accurately as the sum of two exponential terms

$$I(t) = I_{01}e^{-t/\tau_1} + I_{02}e^{t/\tau_2} \quad \text{for } t > 0 \quad (4.1)$$

where I_{01} , I_{02} , τ_1 , and τ_2 are positive constants, and $I_{01} > I_{02}$, $\tau_1 < \tau_2$. These constant values are obtained from the values of $I(t)$ plotted on semilog paper, as shown in Fig. 4.3. Equation (4.1) shows a minimum in $I(t)$ at a time denoted by t_m . At $t < t_m$, the first term, $I_{01}e^{-t/\tau_1}$, is predominant and therefore the current is decreasing. At $t > t_m$, the second term, $I_{02}e^{t/\tau_2}$, dominates.

Reversal experiments under identical experimental conditions were performed also on nominally pure MgO crystals. The current behavior was essentially the same as for MgO:Ni crystals, but the magnitude of the characteristic times was about 30% to 50% larger. The instantaneous current, $-I_{i0}$, after field reversal was smaller. The reversed current reached its minimum value in a much shorter time.

It was noted that when dc was applied to MgO:Ni, black streaks (2) propagating from the negative electrode were observed. Streaks were observed when the contacts were non-uniform. Good contacts were produced using chemically polished crystal, as evidenced by the uniform

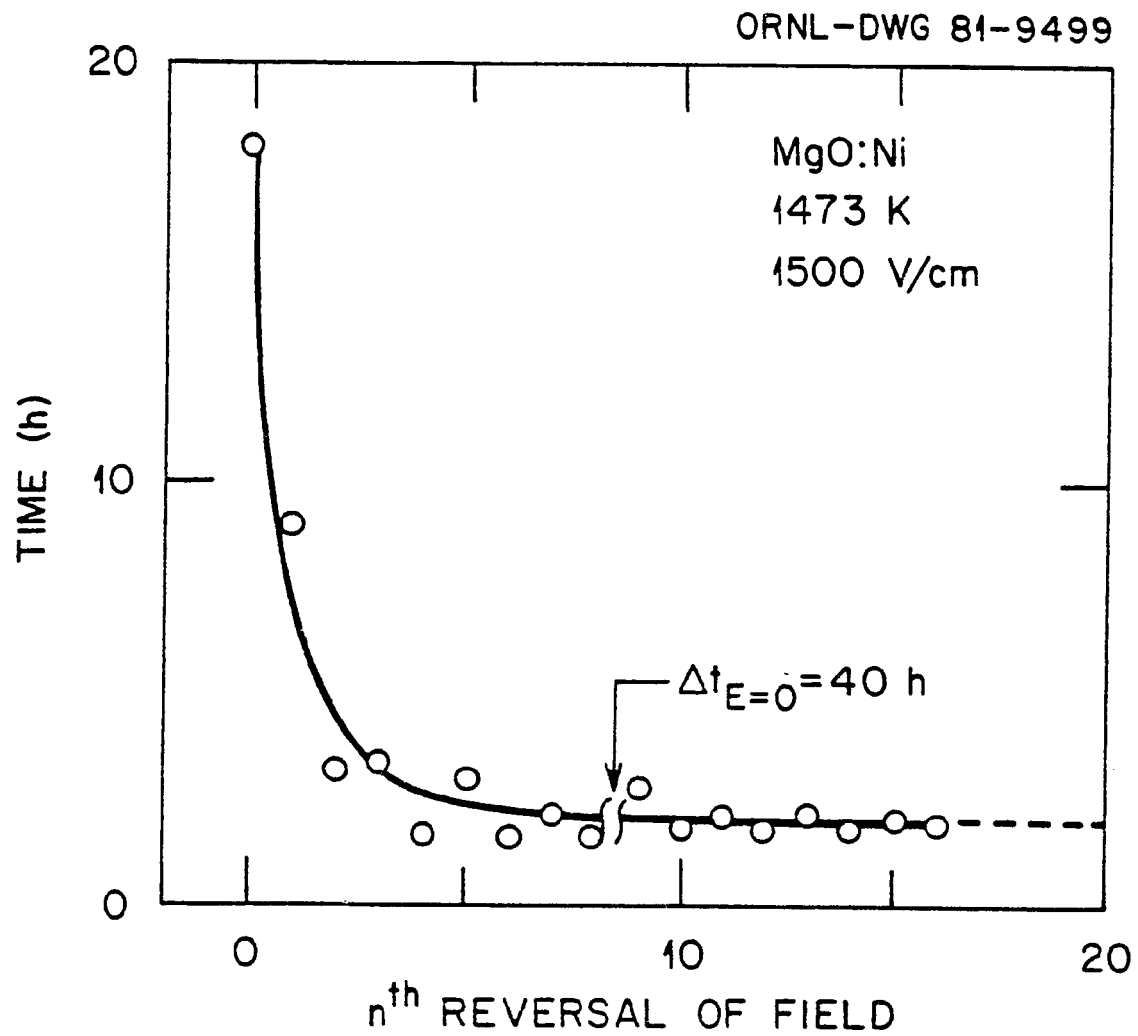


Figure 4.2 Characteristic time for breakdown vs the n^{th} field reversal.

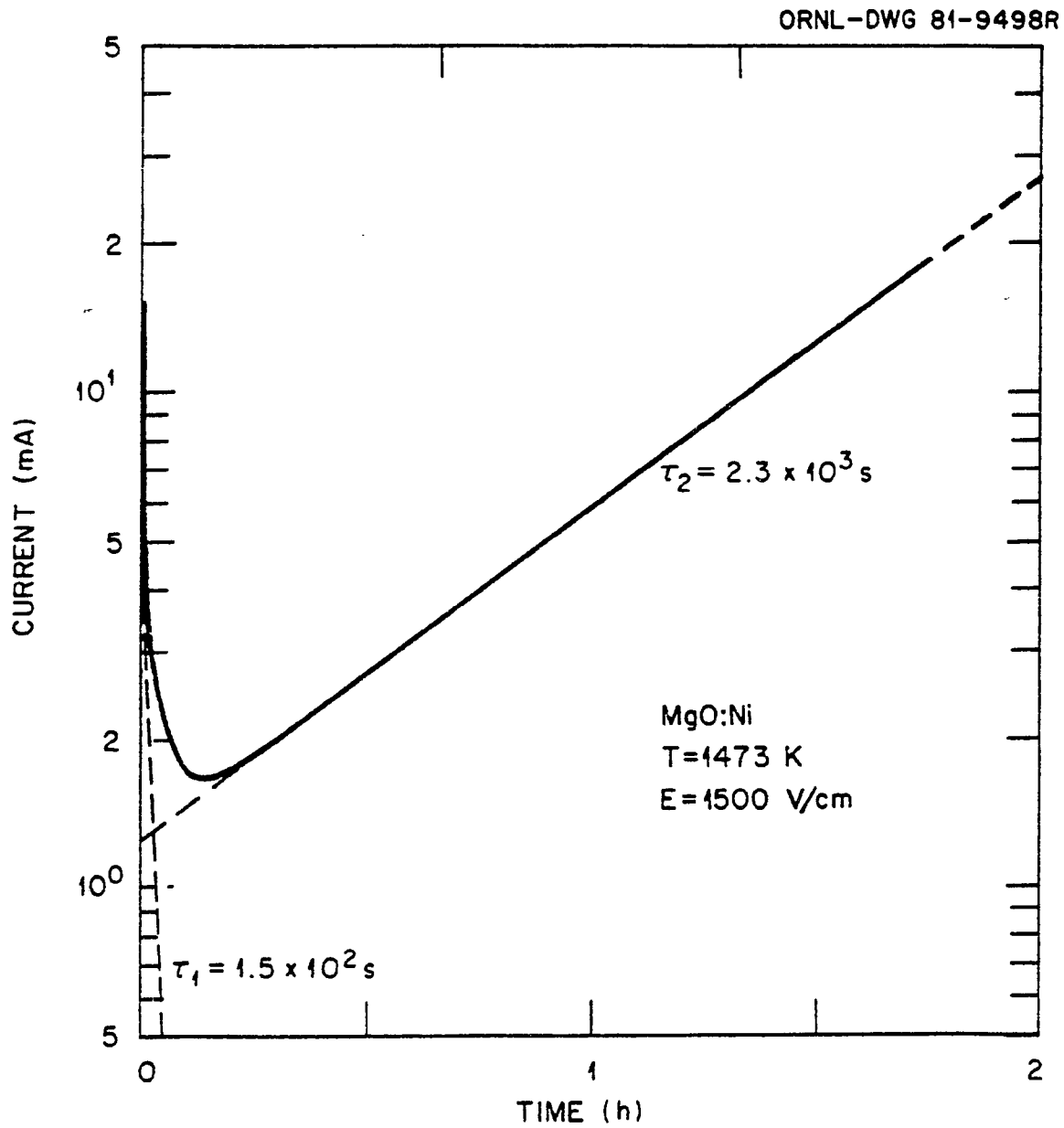


Figure 4.3 Log of current vs time. The current was obtained after 10th field reversal. The line associated with τ_1 was obtained by subtracting the line associated with τ_2 from the original curve.

distribution of dark coloration. If the field was sustained for a sufficiently long time, most of the the crystal between the electrodes became darkened. The coloration is in part due to colloidal Ni. A broad optical absorption band at 2.2 eV is similar to that observed in thermochemically reduced MgO:Ni crystals (69). For undoped MgO crystals, no such coloration was observed.

Figure 4.4 illustrates the general current behavior in MgO:Ni crystals when the polarity of the power supply is reversed at different stages of a given cycle, where a cycle refers to the time interval between two field reversals performed at 18 mA. The solid curve at the bottom represents a given cycle when the field was initially reversed at t_1 . The behavior of the current, when the polarity was reversed again at three different stages, such as t_2 , t_3 , and t_4 , is illustrated in the figure and described as follows:

i) Polarity switch at t_2 , when the current was decreasing: Flowing in the opposite direction, the current reaches an instantaneous value I_i , which has the same magnitude as the current prior to the polarity change. It then continues to rise and saturate at I_{i0} before embarking on an exponential increase.

ii) Polarity switch at t_3 , when the current was at a minimum: The current reverses and also rises immediately to an instantaneous value I_i with the same magnitude as the current prior to the polarity switch. The current remains at I_i for a short period before increasing. Subsequently the current levels off before embarking on the exponential course.

iii) Polarity switch at t_4 , when the current was increasing exponentially: An instantaneous current in the opposite direction is

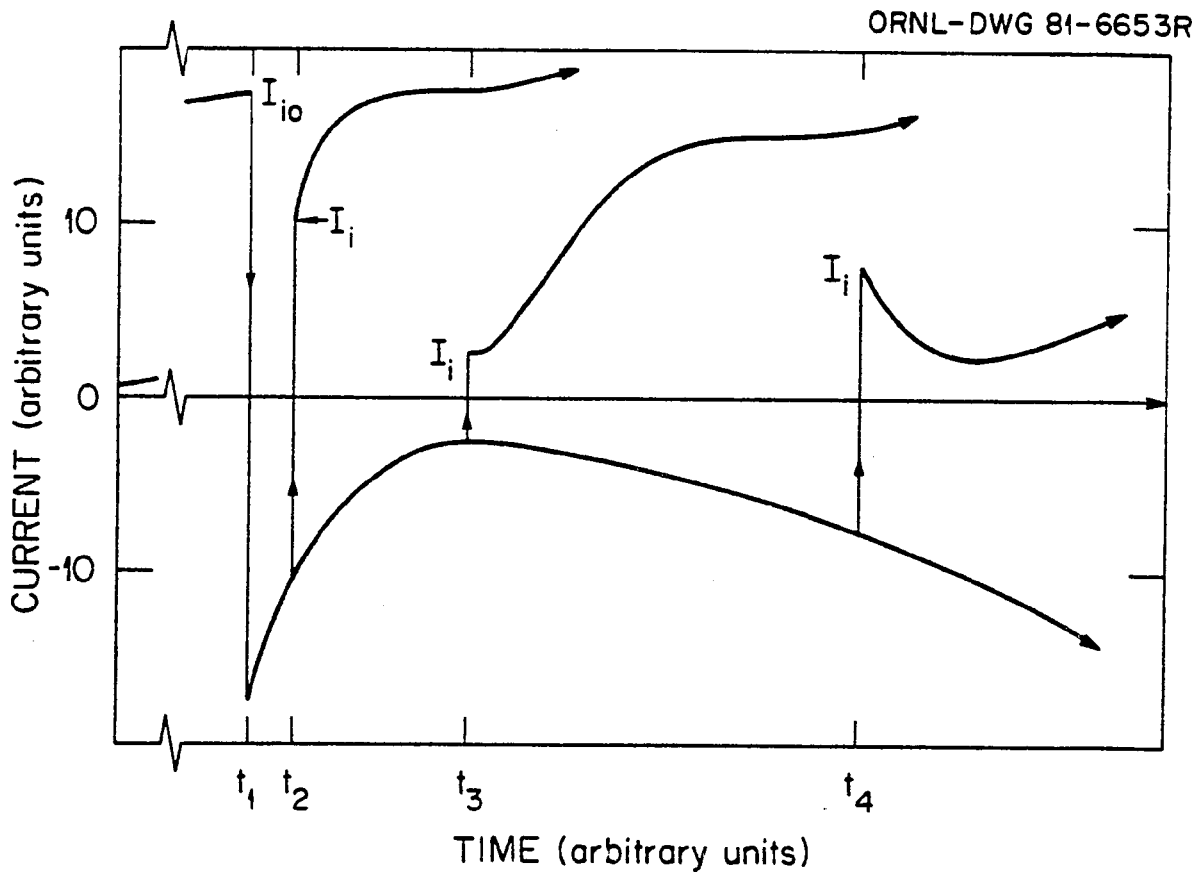


Figure 4.4 Current behavior when the field is reversed at different stages of a given cycle.

again observed. The subsequent current behavior is the same as that shown in Fig. 4.1.

Some generalizations on the current behavior in MgO:Ni crystals can be made from Fig. 4.4. Firstly, whether the current in a given cycle is decreasing, constant, or increasing, polarity change will induce an instantaneous current, which has roughly the same magnitude as the current prior to the polarity switch but flows in the opposite direction. Secondly, the current behavior immediately following the instantaneous current will depend on the current prior to the polarity switch. A diminishing current will result in an increasing current, and vice versa. A constant current will be followed by a constant current. Thirdly, an exponential increase in current will ultimately occur.

b) Instantaneous Current after Time Interval with $E = 0$

An instantaneous current can be obtained in either direction upon restoration of the field following a time interval without applied field, to be denoted as $\Delta t(E=0)$. An illustration is shown in Fig. 4.5. An electric field was applied initially at $t=0$ and removed at $t=10$, when the current reached I_{i0} . When the same field was restored at $t=11$, an instantaneous current I_i was obtained. The subsequent current enhancement then slowed down at a level approximating I_{i0} before increasing exponentially. Later, if the field was removed at $t=12$ and a reversed field was applied at $t=13$, an instantaneous current in the opposite direction, $-I_i$, was obtained followed by a current behavior similar to that shown in Fig. 4.1.

The magnitude of the instantaneous current in either direction is a function of $\Delta t(E=0)$, as shown in Fig. 4.6. Three initial currents, $I_{i0} = 4.0, 8.4, \text{ and } 16 \text{ mA}$, in both directions are shown. The value of

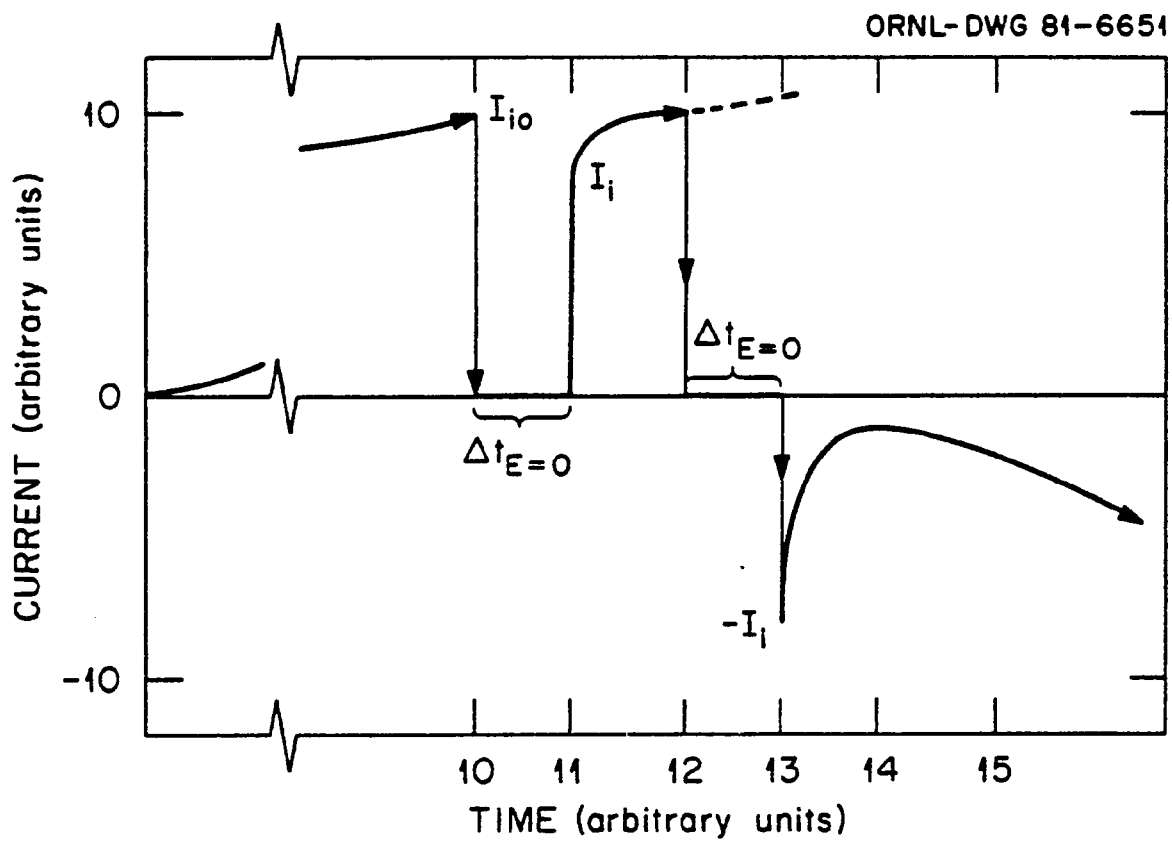


Figure 4.5 Current behavior after a time increment without field ($\Delta t_{E=0}$). The instantaneous current I_i is the current obtained immediately (< 1 sec) after reapplication of the field, either in the same or reversed direction.

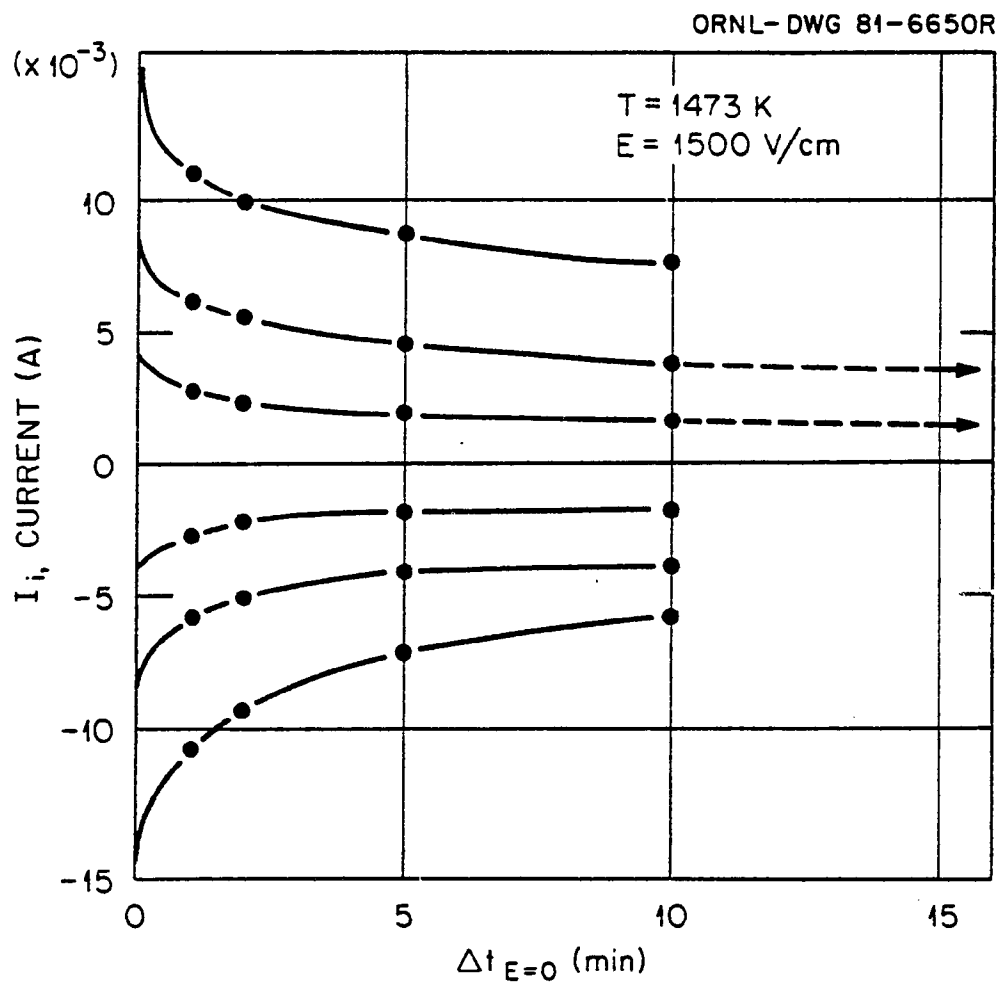


Figure 4.6 Instantaneous current, I_i , as a function of time interval without field, $\Delta t_{E=0}$, for three different initial currents.

I_i decreased rapidly in the first minute and eventually reached a value which was nearly constant. It became nearly constant after 5 mins for $I_{i0} < 5$ mA, and 15 mins for $I_{i0} > 5$ mA. After 40 h (not shown), an instantaneous current 0.5 mA was detected for $I_{i0} = 8.4$ mA. There appears to be symmetry between the positive and negative currents.

c) Short-Circuit Current

A method of obtaining information on the distribution of stored charges inside the sample and therefore the mechanism for the breakdown is to measure the short-circuit current I_{SC} , which flows from one sample surface to the other via an external conductor when the electric field is removed. The I_{SC} as a function of time after field removal at $I_{i0} = +18$ mA is shown in the bottom of Fig. 4.7. It was found to flow in the opposite direction. It decreased rapidly in the first minute and remained nearly constant at $t > 15$ min. For comparison, a curve for instantaneous current as a function of $\Delta t(E=0)$ is plotted in the top figure. While the shape of the I_{SC} and I_i curves appear to be symmetric, the former is about three orders of magnitude smaller.

When the same electric field was restored at $t=10$ mins, an instantaneous current I_i of the same magnitude as that shown in the top curve was obtained. In fact, it would coincide with the top curve regardless of when the same field was applied again. The coincidence of the I_i with the top curve and the small I_{SC} values indicates that annihilation of stored charges occurs almost entirely within the crystal.

It is noted that immediately after field removal at $I_{i0} = 18$ mA, a high-impedance voltmeter measured about 0.5 volts across the sample with the polarity being the same as the applied field. The decay pattern of the voltage was similar to that of I_{SC} .

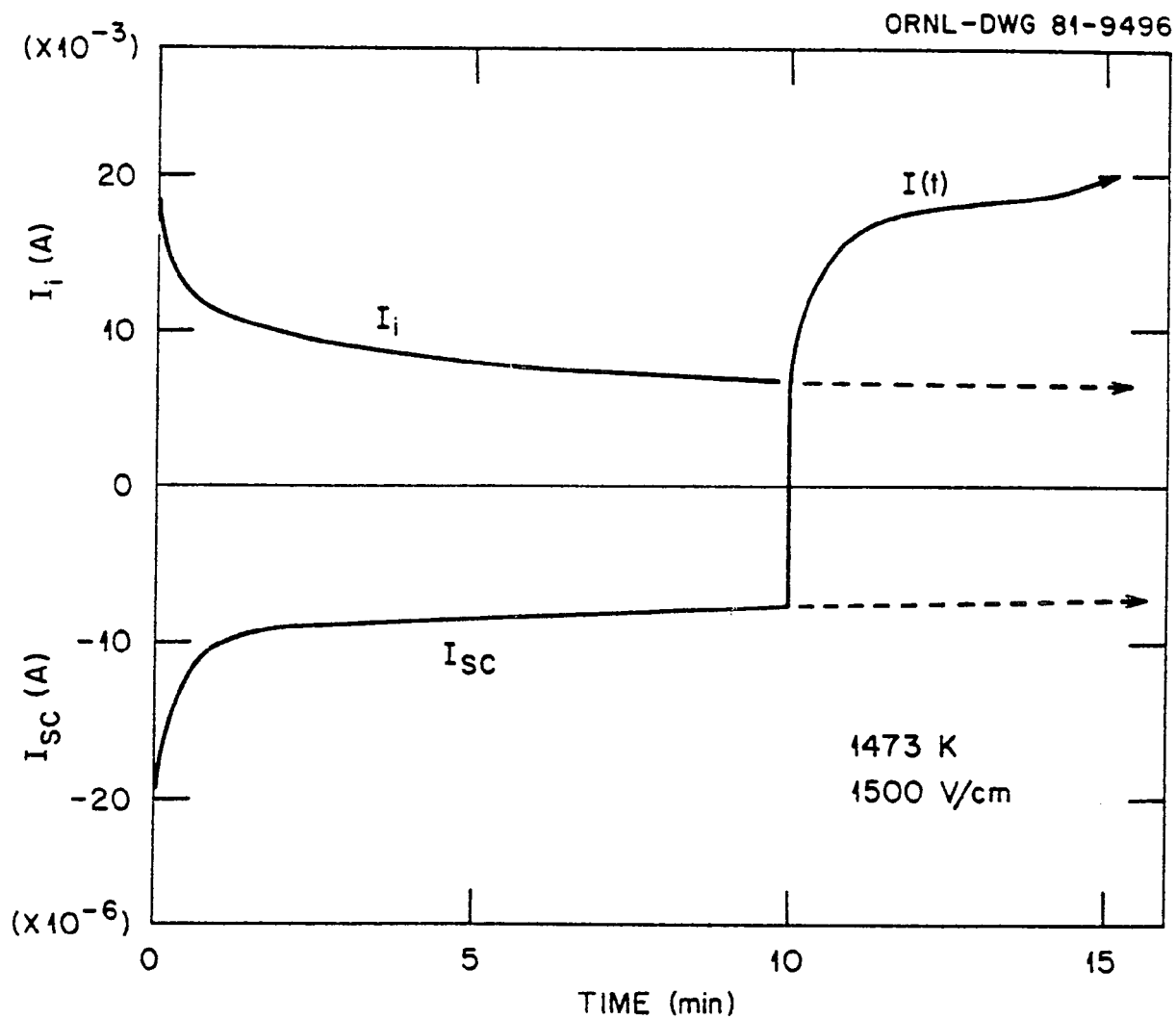


Figure 4.7 Top curve: Instantaneous current vs $\Delta t_{E=0}$. Bottom curve: Short-circuit as a function of time.

The short-circuit current was also been measured after the applied field had been reversed for different time periods. Figure 4.8a shows five different points along a typical current curve before and after the field reversal. The short-circuit currents measured at these points are shown in the corresponding numbered curves of Fig. 4.8b. The positive current direction is defined as the direction of initial current before the first field reversal. Curve 1 was obtained just before the field reversal, that is at $I = +18 \text{ mA}$, which was the same as the bottom curve of Fig. 4.7. Curve 2 was obtained immediately ($< 1 \text{ sec}$) after the field was reversed. The short-circuit current, initially flowing in the positive direction, decreased rapidly from about $+ 2 \text{ } \mu\text{A}$ to zero in a few seconds and then flowed in the negative direction. Then the current increased to a maximum (about $8 \text{ } \mu\text{A}$) before it decreased in a behavior similar to curve 1. Curve 3 was obtained at 10 sec after the field was reversed. The current behaved similarly to that described in curve 2. The current showed a higher initial positive value and a lower final negative value than that in curve 2. Curve 4 was measured 15 min after the reversal, just before the reversed current reached its minimum, the short-circuit current flowed in the positive direction and decayed to zero in about 1 min. Curve 5 was obtained 30 min after the reversal, when the reversed current just began to increase. The current behavior was similar to that in curve 4 but its magnitude was larger.

d) Alternating Electric Field

As noted in Fig. 4.1, it requires about an hour to observe a definite increase in current, and it requires 18 hours for the current to reach 18 mA . Also investigated was the question of whether a similar current increase would occur if the same field was applied, but reversed

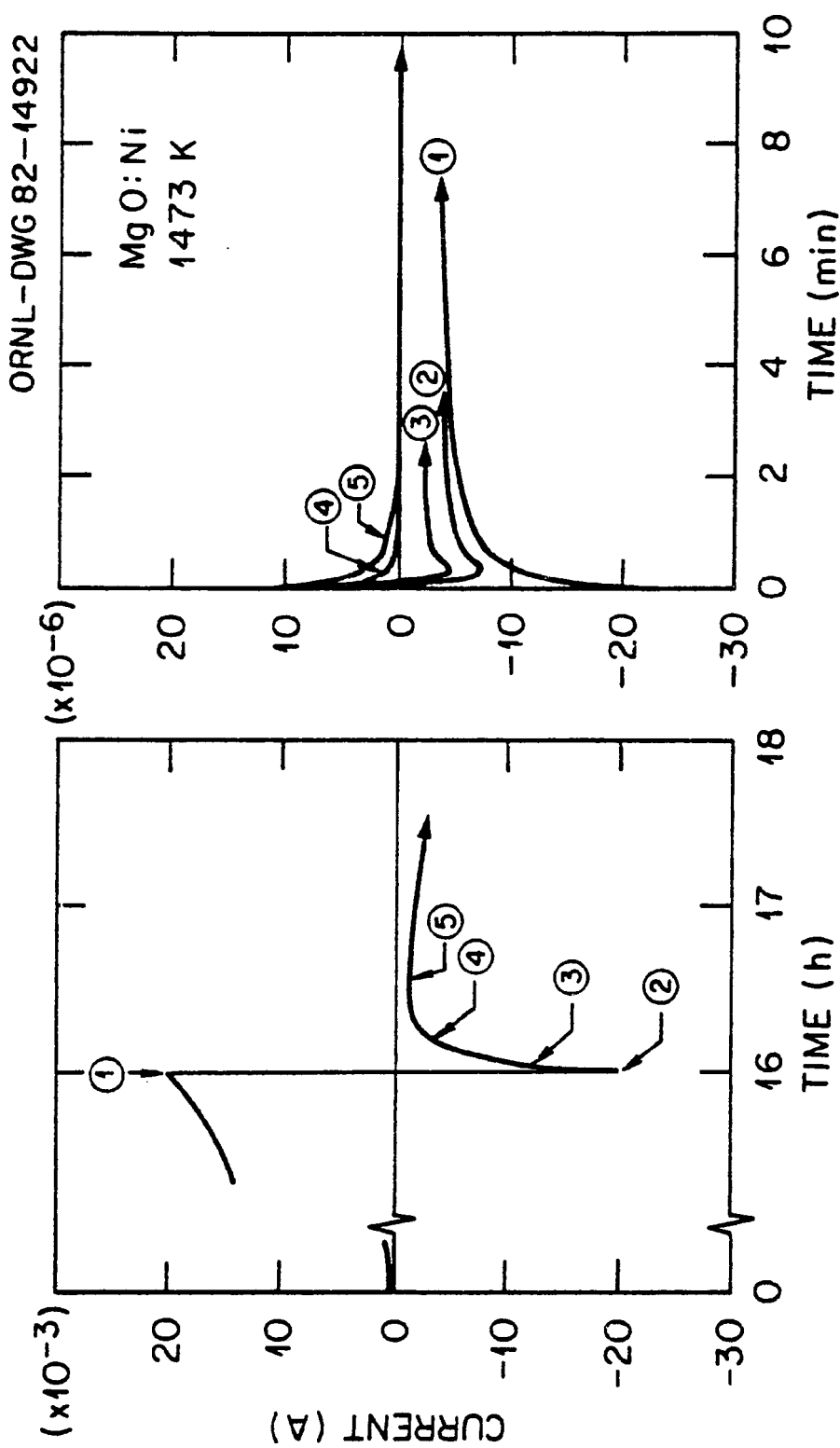


Figure 4.8 (a) Five points along a typical current curve before and after the field reversal. (b) Short-circuit current vs time. Those currents were measured at points shown in (a).

frequently such as in an alternating electric field. Results were shown in Fig. 4.9.

An alternating field of $1500 \text{ V-cm}^{-1}(\text{rms})$, 60 Hz, was applied to two samples: (a) an as-grown MgO:Ni crystal, and (b) a MgO:Ni crystal which had undergone a current increase due to direct bias. In the first sample there was no significant change in the current even after 24 h, even though there were fluctuations during the first 3 h (see the lower curve in Fig. 4.9). No dark coloration across the sample was observable. In the second sample, the direct current through the sample reached 18 mA before the alternating field was applied. A high alternating current was observed initially (the top curve in Fig. 4.9) but it eventually decayed to a level somewhat higher than in the first case. The application of an alternating field did not remove the dark coloration caused by the direct bias.

4.1.2 Activation Energy

The activation energy associated with the Dielectric breakdown of MgO crystals was obtained by three different methods described as follows:

a) Time Constants of $I(t)$

As noted in Eq. (4.1), the time dependent current $I(t)$ can be expressed as the sum of two exponential terms with different time constants. The characteristic time effectively diminished with each reversal until a constant value is reached, as shown in Figs. 4.1 and 4.2. Correspondingly, the constants I_{01} , I_{02} , τ_1 and τ_2 were changing with each reversal. After the tenth reversal they remained unchanged. Activation energies associated with τ_1 and τ_2 after the tenth reversal

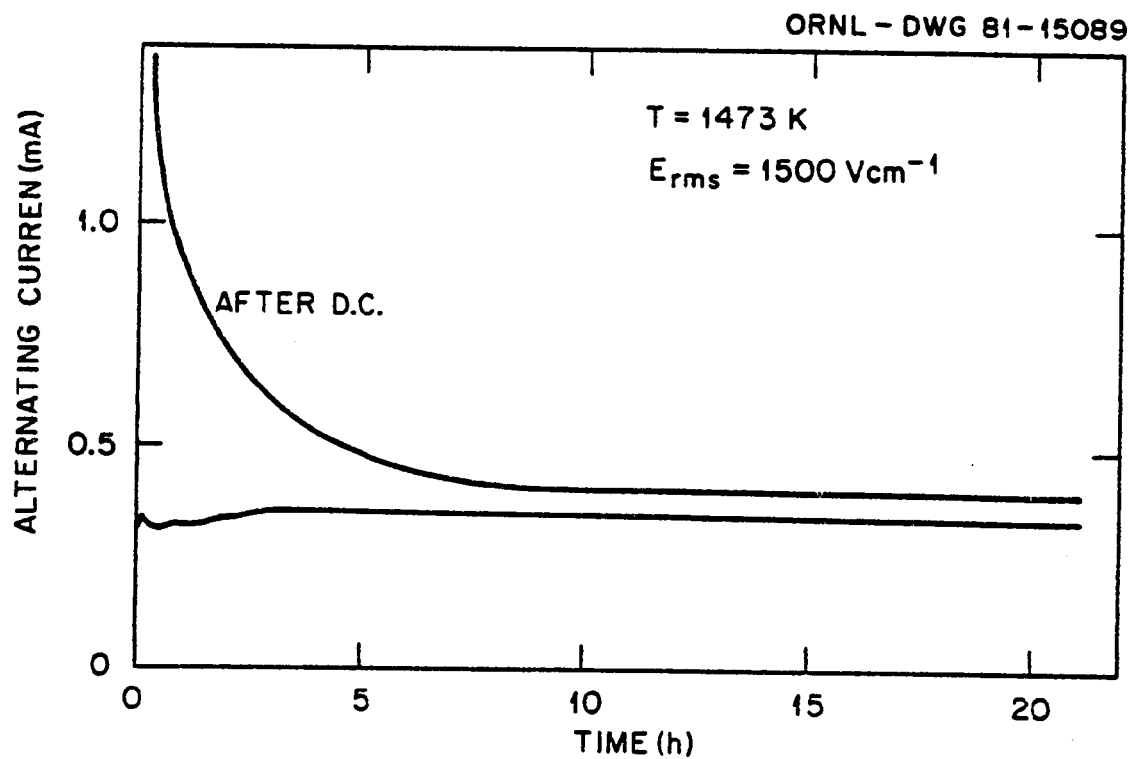


Figure 4.9 Current vs time with application of alternating field for (a) an as-grown MgO:Ni crystal, and (b) a similar crystal having experienced a current increase due to a dc field.

were obtained: Measurements were made at $T = 1200, 1248, 1302$ and 1352°C , as shown in Fig. 4.10. For a given field, the time constants τ_1 and τ_2 were found to obey the relationship:

$$\tau_1 = \tau_{01} e^{Q_1/kT}, \quad (4.2)$$

$$\tau_2 = \tau_{02} e^{Q_2/kT}, \quad (4.3)$$

where Q_1 and Q_2 are activation energies for τ_1 and τ_2 , respectively. The activation energies were found to be: $Q_1 = 3.7 \pm 0.3$ eV and $Q_2 = 2.3 \pm 0.2$ eV.

b) Short-Circuit Current

Short-circuit current $I_{SC}(t)$ decreased rapidly in the first minute, but became nearly constant after 15 minutes (see Fig. 4.7). Therefore, the current could be measured at different temperatures (all within five min) when the temperature is decreasing. The results are shown in Fig. 4.11. Both the nickel-doped and the nominally pure MgO crystals yield an activation energy of 2.4 ± 0.1 eV.

c) Alternating Current

As shown in Fig. 4.9, the alternating current became constant after 3 h of applied field. Therefore the temperature dependence of the steady-state current could be measured easily. The log of the alternating current plotted against $1000/T$ was shown in Fig. 4.12. An activation energy of 2.4 ± 0.1 eV was obtained.

4.1.3 The Effect of Sample Thickness

The breakdown characteristics of MgO crystal is nearly independent of the sample thickness. Thickness-dependence measurements have been

ORNL-DWG 82-9083R

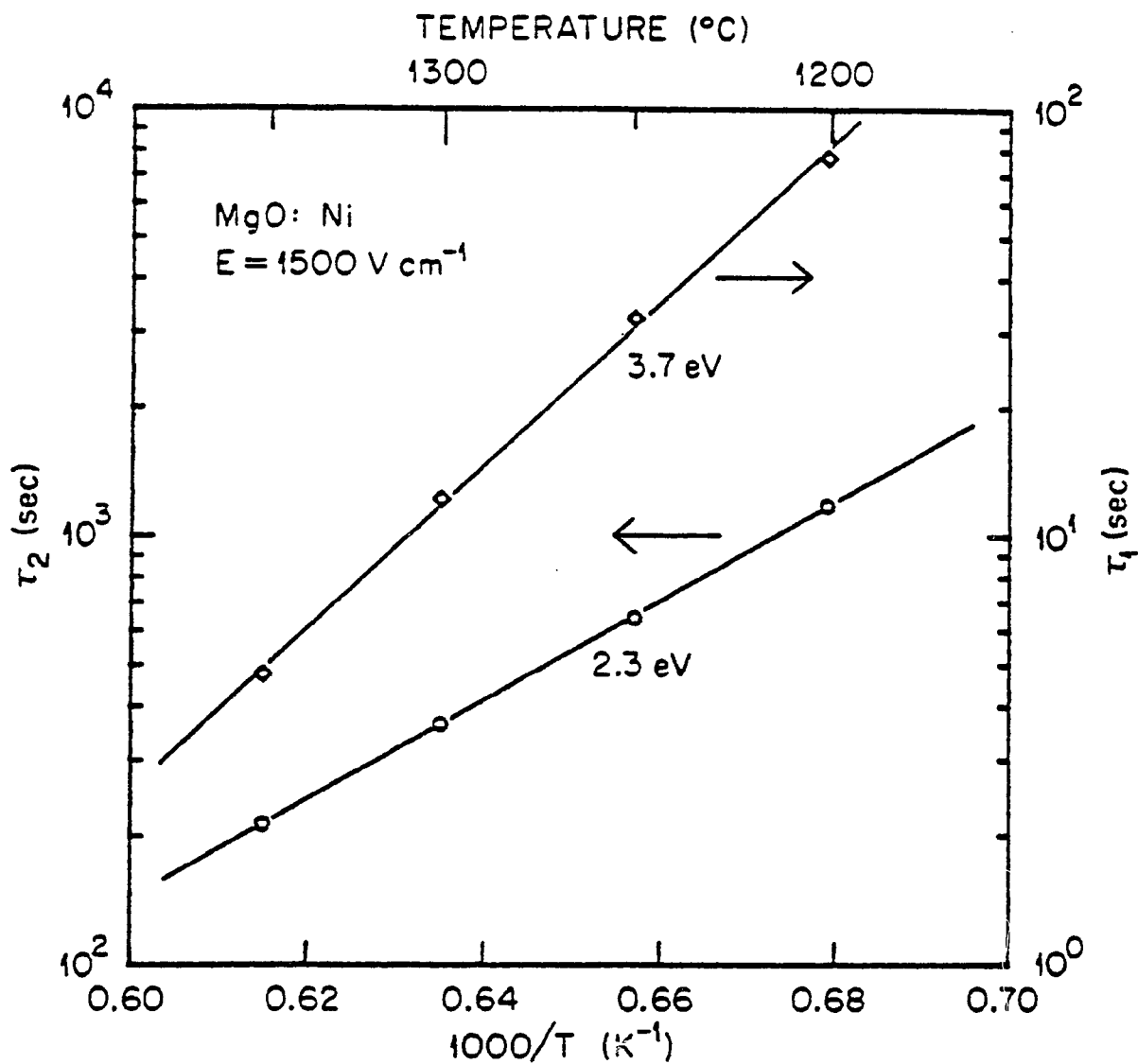


Figure 4.10 Log of the time constants τ_1 and τ_2 were plotted against $1000/T$. The activation energies determined from the slopes for τ_1 and τ_2 were $3.7 \pm 0.3 \text{ eV}$ and $2.3 \pm 0.2 \text{ eV}$, respectively.

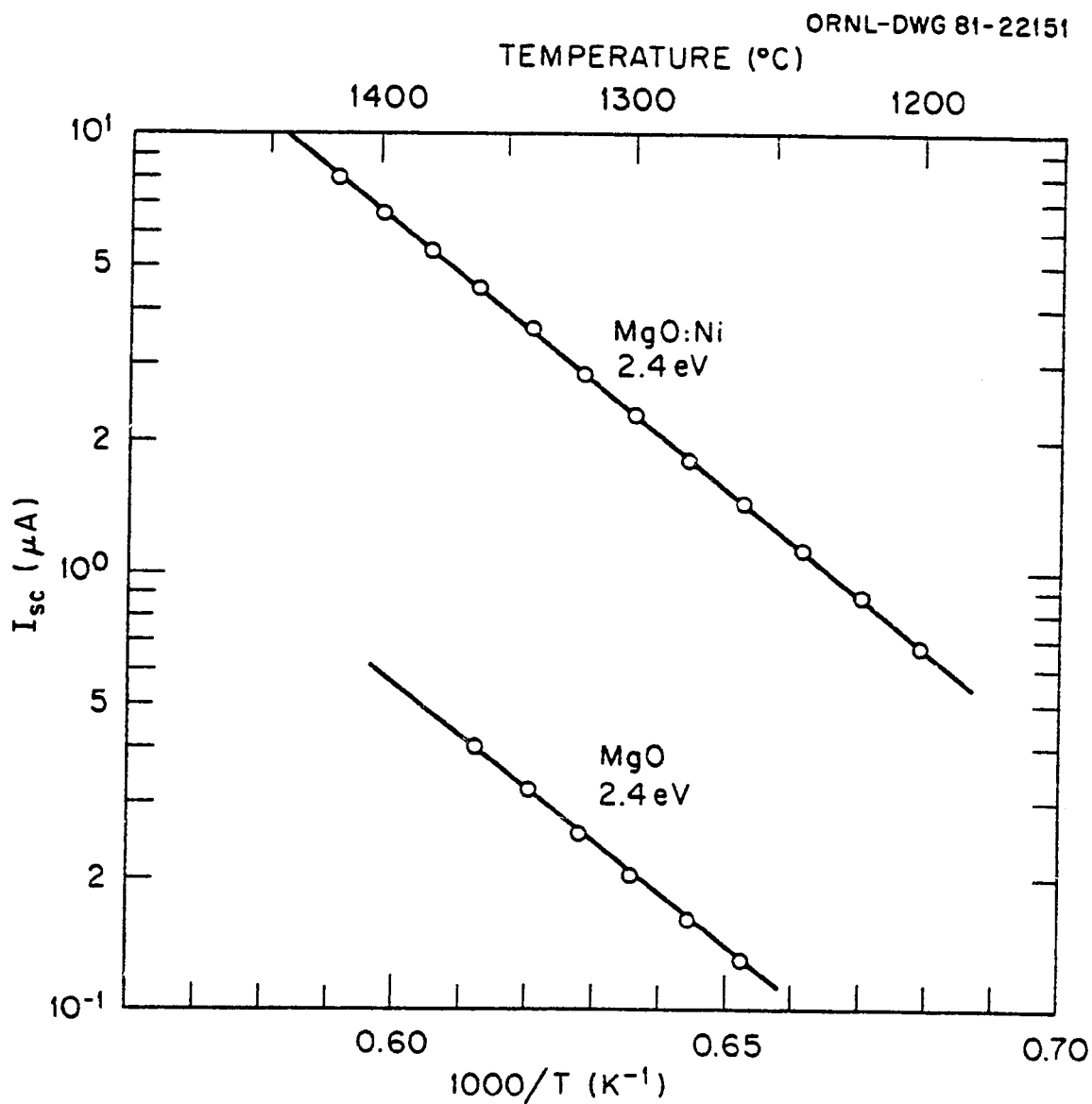


Figure 4.11 Log of the short-circuit current vs $1000/T$ for both MgO:Ni and nominally pure MgO crystals. Activation energy 2.4 ± 0.1 eV was obtained.

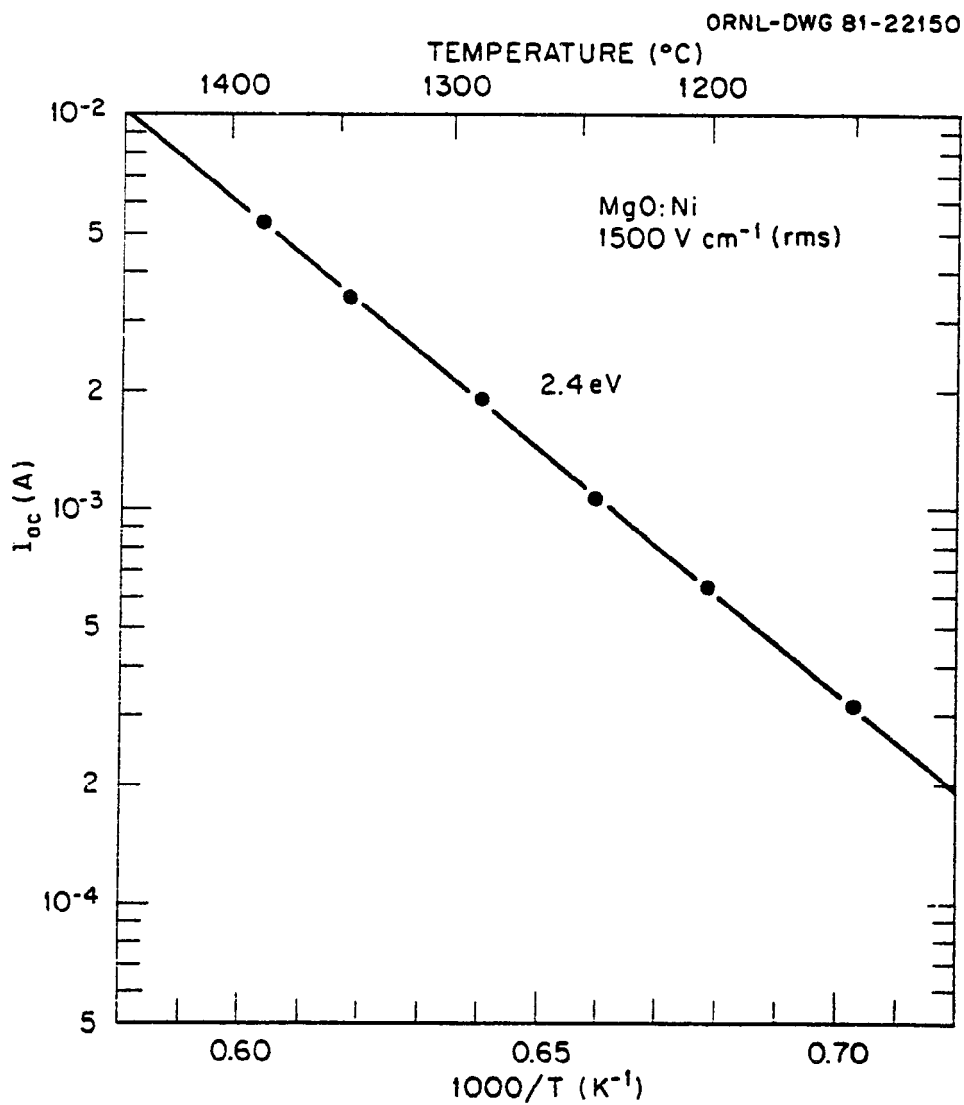


Figure 4.12 Log of the alternating current vs $1000/T$ for MgO:Ni crystal. Constant field 1500 V/cm (rms) was used. Activation energy 2.4 ± 0.1 eV was calculated from the slope.

performed on MgO:Ni crystals at 1473 K with the use of an electric field of 1500 V/cm for thickness ranging from 0.2 mm to 9.1 mm. The characteristic time for breakdown and the time constant τ_2 of current equation (Eq. 4.1) are plotted as a function of sample thickness in Figs. 4.13 and 4.14, respectively. It is noted that the time constant τ_2 is almost thickness independent for thickness up to 5 mm, but the breakdown time decreases somewhat for samples thicker than 3.5 mm.

4.1.4 Field Strength Effect

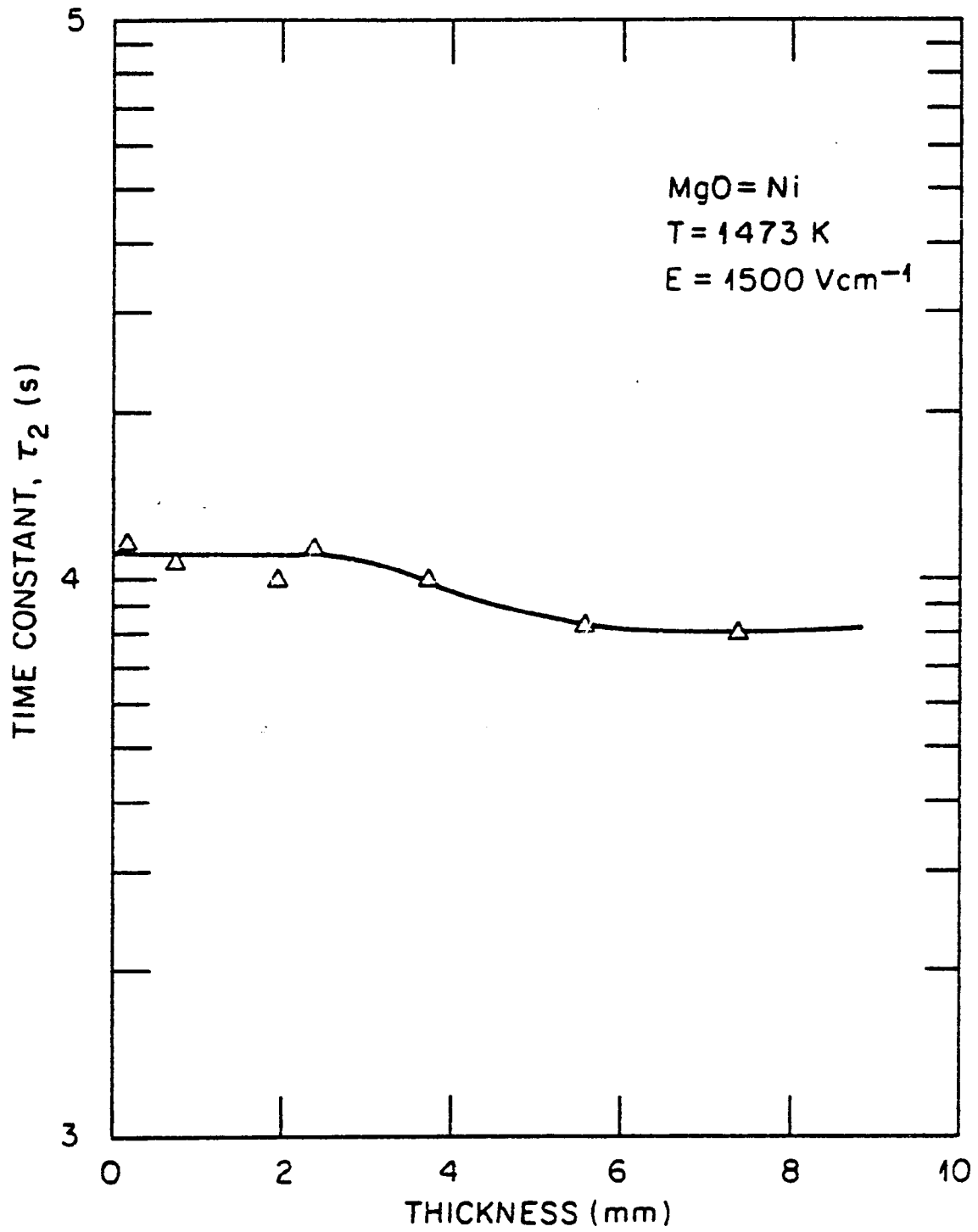
The investigation of the field strength effect on the breakdown was performed at 1473 K on (i) several as-grown MgO:Ni crystals, and (ii) MgO:Ni crystals which had a past history of having been treated at 1473 K using an electric field of 1500 V/cm for more than 10 field reversals. The results are described in terms of the time constant τ_2 rather than the characteristic time for breakdown t_c , because the time constant τ_2 is not only directly related to the breakdown time, but also has a simple relationship with the applied field. The values of τ_2 have been found empirically to decrease exponentially with the applied field strength, as described by

$$\tau_2(E) \propto e^{-\beta E} \quad (4.4)$$

where β is a positive constant. The value of β depends on the past history of the sample as well as the given field strength.

In the case of as-grown samples, as shown in Fig. 4.15, the value of β has been found to be (i) 2.3×10^{-3} cm/V for field strengths less than 1 K V/cm, (ii) 4.5×10^{-4} cm/V for field strengths from 1 to 10 K V/cm, and (iii) decreasing with an increase of the field. It has been

ORNL-DWG 82-17193

Figure 4.13 Time constant τ_2 vs sample thickness.

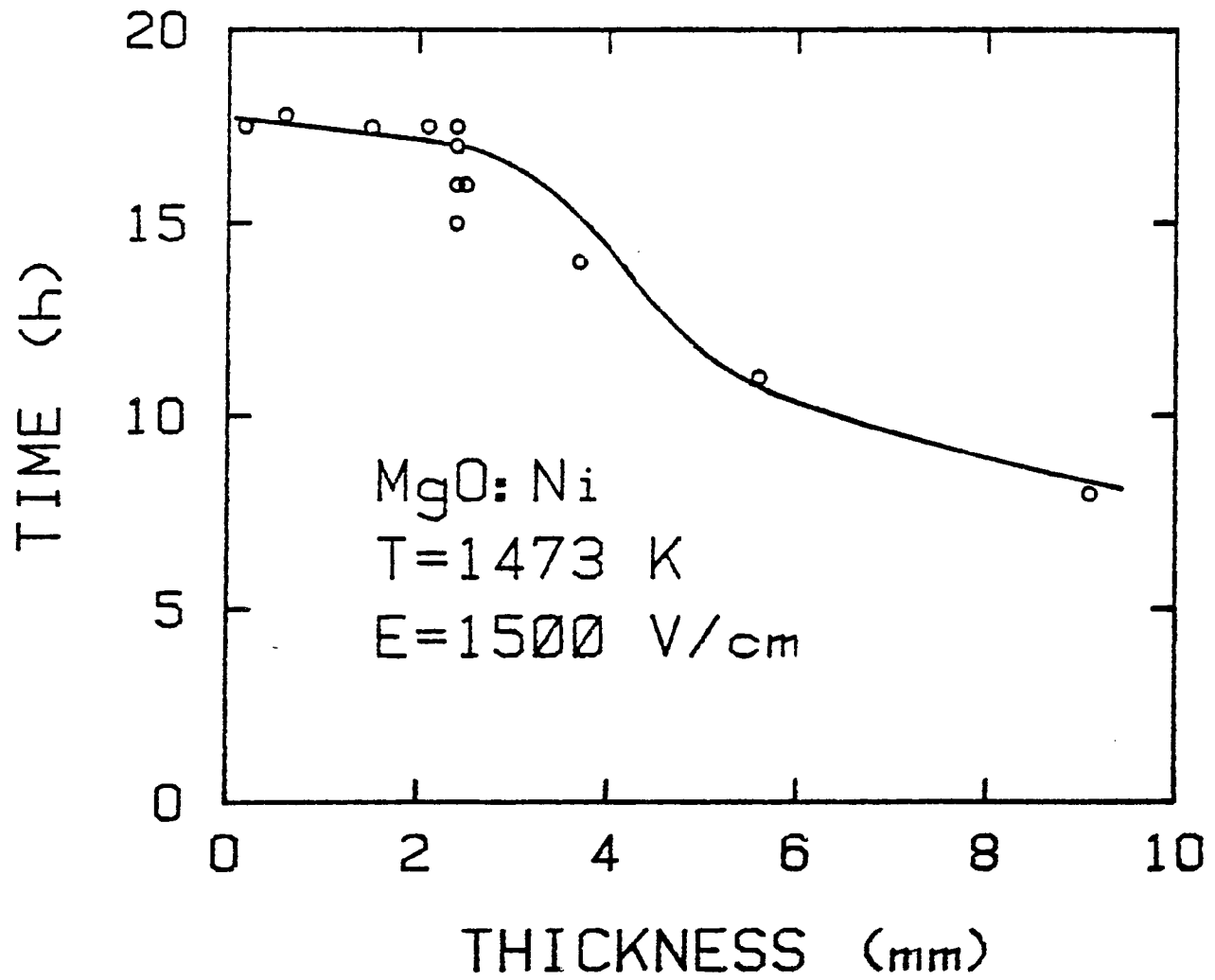


Figure 4.14 Time required for current to reach 18 mA vs sample thickness.

ORNL-DWG 82-14923

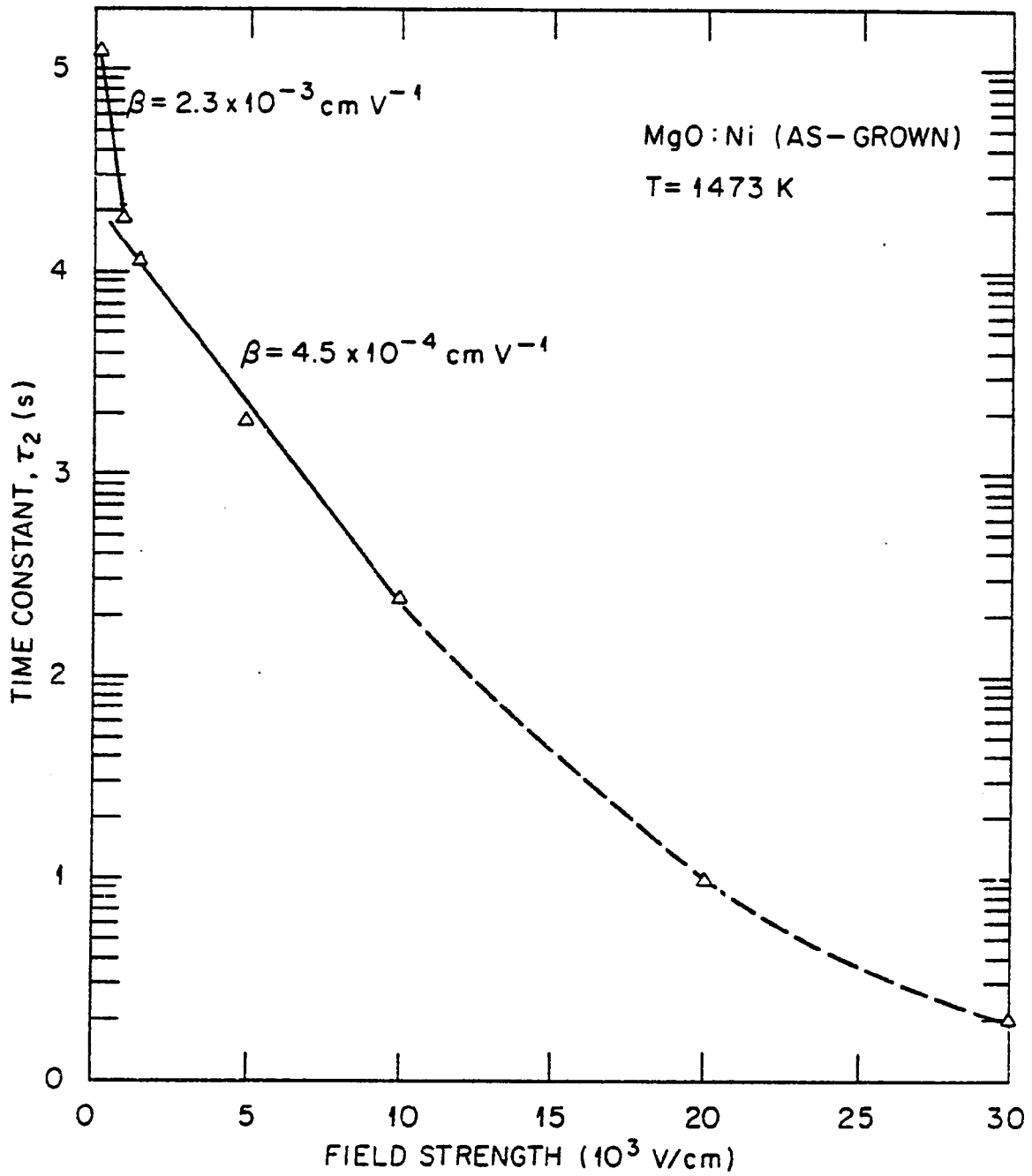


Figure 4.15 Time constant τ_2 vs electric field strength. The measurements were made on as-grown MgO:Ni crystals.

also estimated that the value of β is less than 5×10^{-5} cm/V when the field strength reaches a magnitude of 10^6 V/cm.

In the case of the samples with a past history of having undergone 10 cycles of electrothermal treatments, as shown in Fig. 4.16, $\beta = 2.7 \times 10^{-3}$ cm/V has been measured at temperatures 1473 and 1673 K for field strengths from 1 to 2 K V/cm. This value is greater than that obtained from the as-grown samples with the same electric field.

Taking into account the temperature effect, Eq. (4.3), the time constant τ_2 can be expressed as

$$\tau_2 = \tau_{02} \exp\{(Q_2/kT) - \beta E\}, \quad (4.5)$$

where Q_2 is activation energy, and β is a constant at a given range of field strength.

4.1.5 Current-Voltage Characteristics

The current-voltage characteristics of MgO crystals at high temperatures was measured and a nonlinear I-V relationship has been obtained. The I-V relationship is described as

$$I \propto V^n, \quad (4.6)$$

where n is a constant. The value of n depends on the past treatment history of the crystal and the electric field strength, as shown in Fig. 4.17.

A MgO:Ni crystal with thickness 0.62 mm was treated at 1473 K with an electric field of 200 V/cm. The I-V measurements were performed at various stages during the treatment, and then the same field was again applied to the sample until the next I-V measurements. Several I-V curves were obtained subsequently, and the results were shown in the

ORNL-DWG 82-14925R

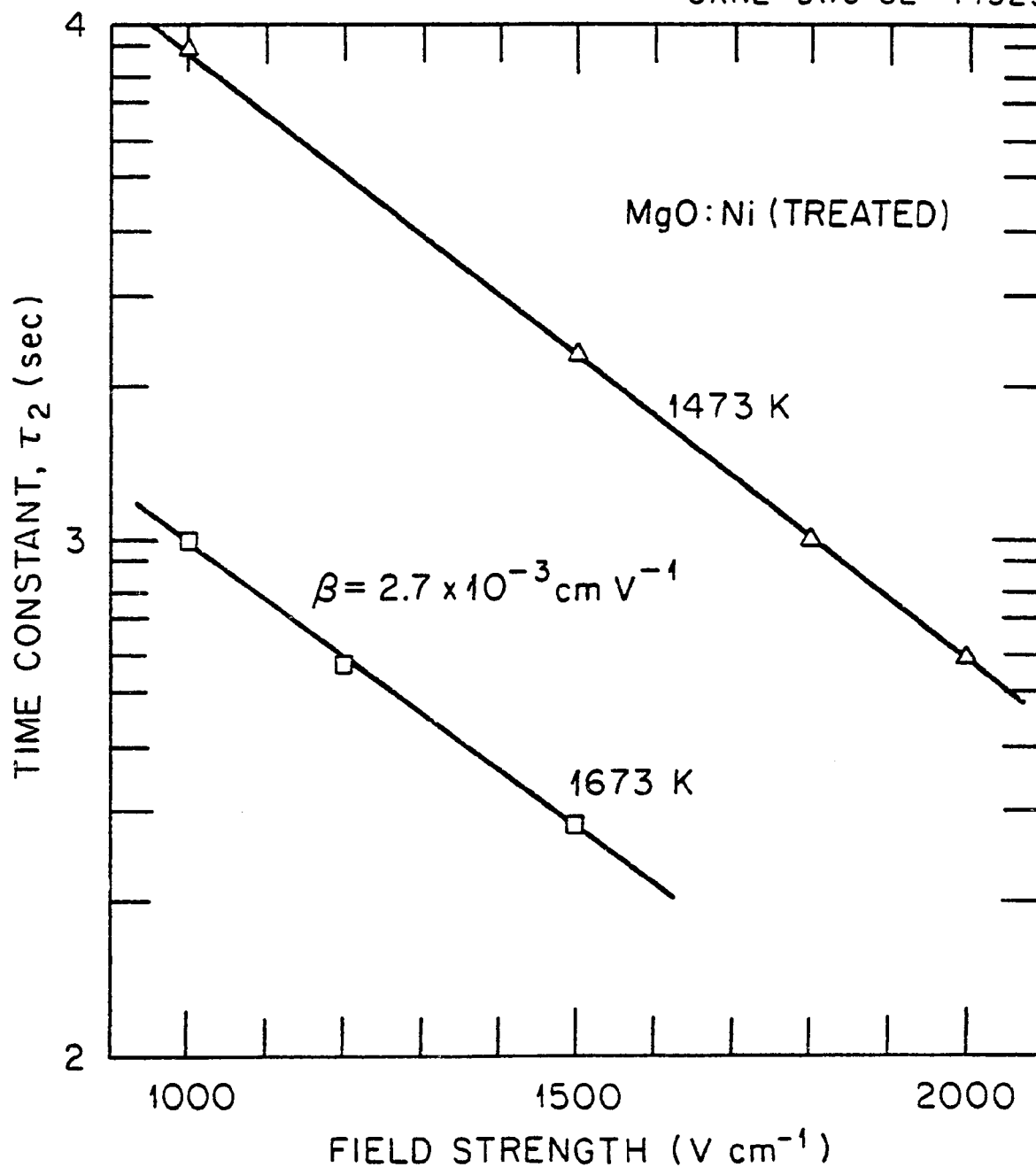


Figure 4.16 Time constant τ_2 vs electric field strength. The measurements were performed after 10th field reversal. Two temperatures 1473 and 1673 K were used.

ORNL-DWG 82-19656

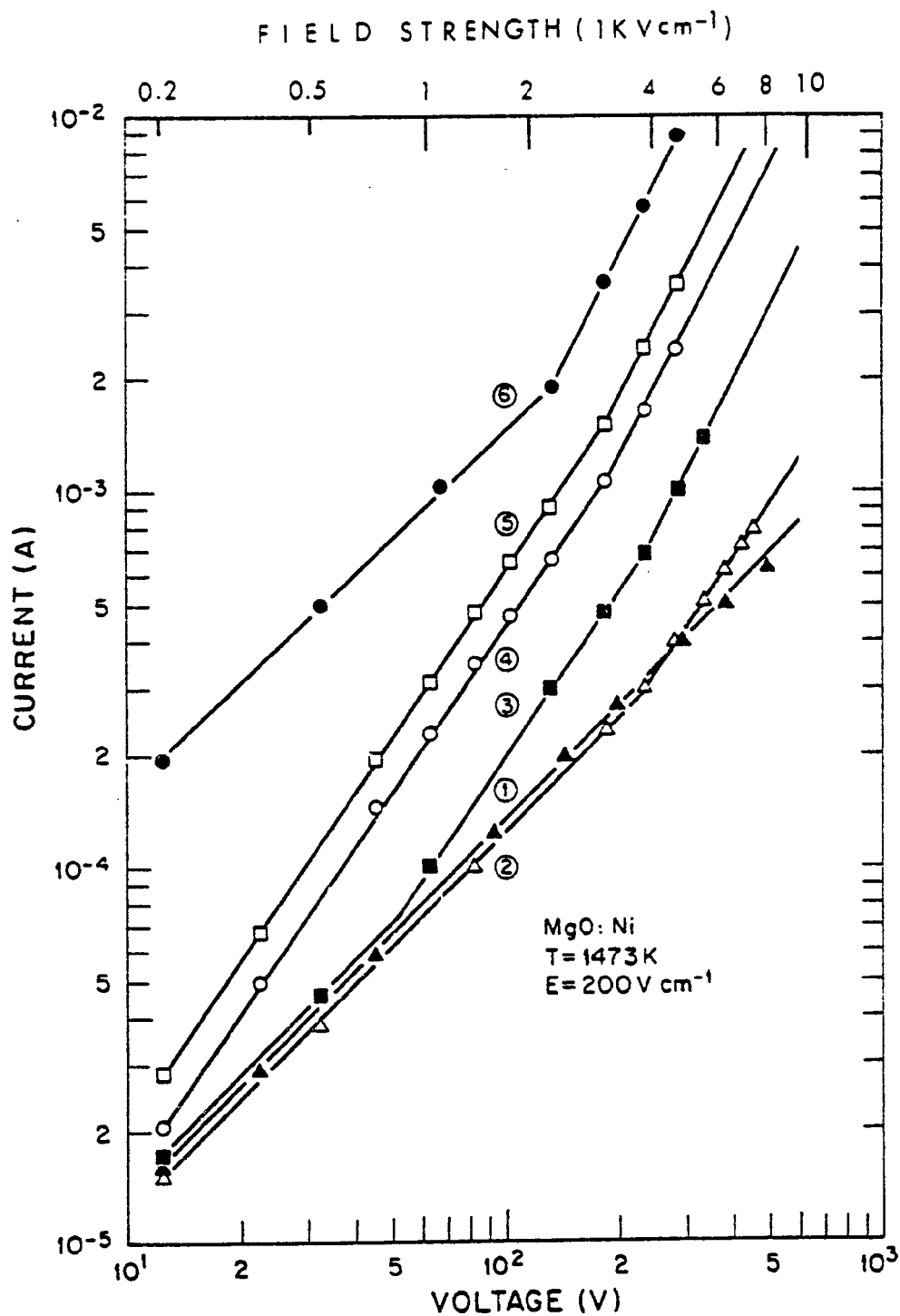


Figure 4.17 I-V characteristics of a MgO:Ni crystal. The sample was treated at 1473 K using an electric field of 200 V/cm. The I-V measurements were performed at various stages during treatment.

numbered curves in Fig. 4.17. At $t=0$, a $n=1$ was obtained for field strengths up to 8×10^3 V/cm, as shown in curve 1. At $t = 1.5$ h, when the current was at the minimum value, curve 2 was obtained. The value of $n=1.0$ was again observed for field strengths lower than 4×10^3 V/cm. Above this field strength, a new value of $n=1.5$ was measured. At $t=3.5$ h, three values of $n=1.0$, 1.5, and 2.0 were obtained, as shown in curve 3, corresponding to $E < 800$ V/cm, $800 < E < 4 \times 10^3$ V/cm, and $E > 4 \times 10^3$ V/cm, respectively. There were only two values of n , 1.5 and 2.0, observed at $t=11$ and 21 h, as shown in curves 4 and 5, respectively. The value of $n=2.0$ was obtained at field strengths higher than 3×10^3 V/cm in both cases. At $t=45$ h, $n = 2.0$ was obtained at a field strength as low as 2×10^3 V/cm when current increased one order of magnitude, as shown in curve 6. The quadratic behavior of the I-V curve became observable at lower fields at higher current levels.

After a long period of current treatment, the I-V characteristics of the treated sample always show two different ranges with $n=1.0$ and 2.0, as shown in Fig. 4.18. A MgO:Ni crystal with thickness of 0.76 mm was treated at 1473 K using a constant current, 1 mA for the first 5 h and then 10 mA for another 15 h. The voltage across the sample was decreasing with time. After 20 h, the voltage was nearly constant across the sample, and the I-V curve was measured. The linear I-V relation (Ohm's relation) was only observed for fields lower than 500 V/cm. The quadratic I-V curve was measured for field strengths from 1000 V/cm to 2000 V/cm. For even higher fields, it was found that the value of n was greater than 2.0, but the result was not reproducible.

ORNL-DWG 82-19652R

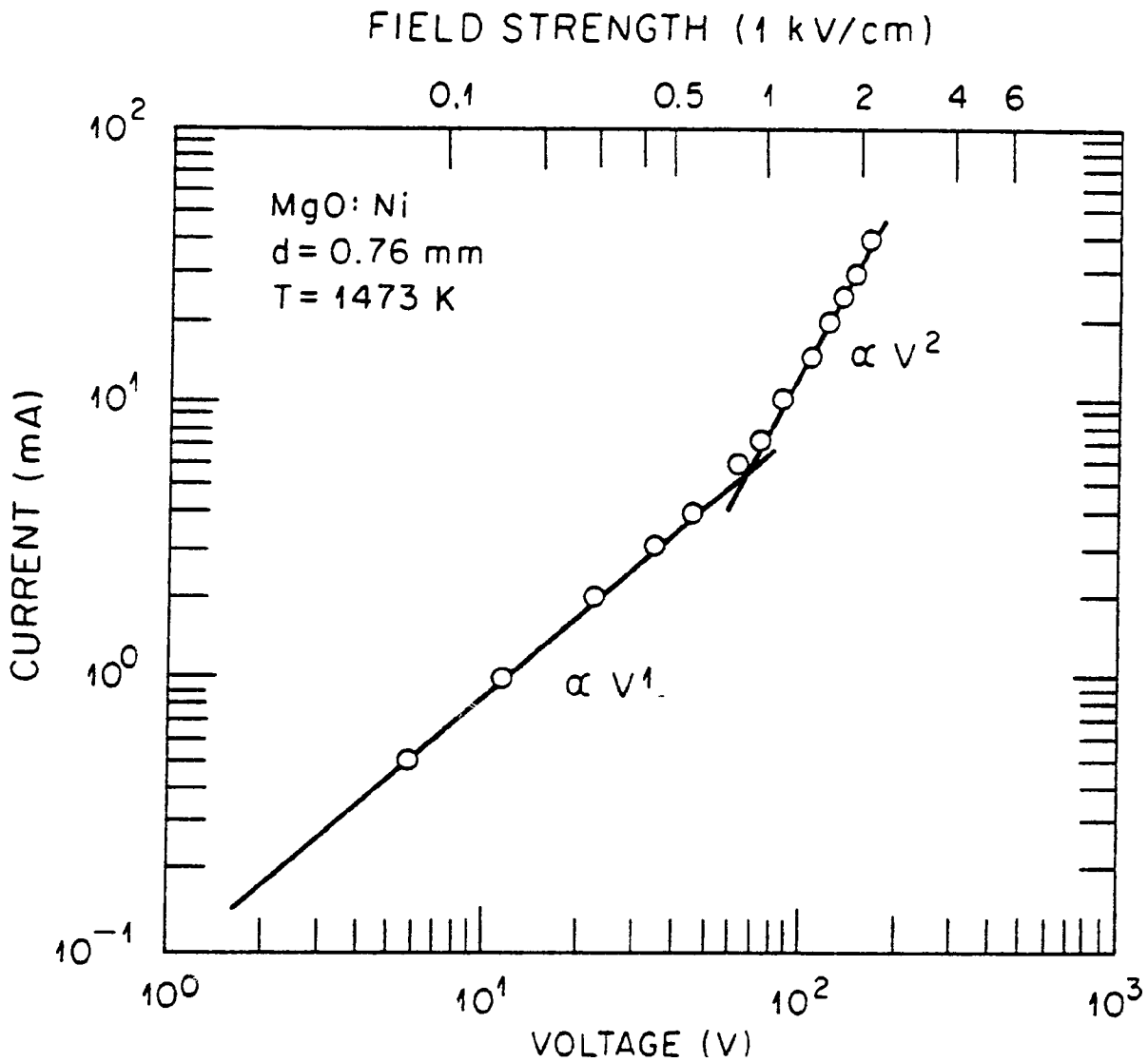


Figure 4.18 I-V characteristics of a MgO: Ni crystal after a constant current of 1 mA for the first 5 h and then 10 mA for another 15 h had been applied to the crystal.

4.1.6 Potential Profile

The potential profiles of MgO:Ni crystals treated at 1473 K using an electric field of 1000 V/cm were measured at different current levels during the treatment as well as after the removal of the applied voltage. The sample thickness was 5.6 mm. The measurements were performed in both the first cycle (as-grown sample) and after the voltage was reversed. There were five platinum probes used between cathode and anode (see Fig. 3.2).

a) An As-Grown MgO:Ni Sample

Several sets of potential measurements were performed at various stages before the current reached 18 mA. The current levels at which the measurements were made are shown in Table 4.1. Each set of measurements were plotted as a corresponding numbered curve in Fig. 4.19. Curve 1 was obtained at $t=0$, immediately after the voltage was applied to the sample. The potential was nonlinear with depth and the curve was not symmetric about the center of the crystal. The potential gradient was greatest near the electrodes. Curve 2 was obtained at $t=10$ seconds (hereafter referred to as sec) after the application of the voltage when the current was decreasing. The curve was similar to curve 1 except the central flat region voltage was lower. The voltage drop in the region near the anode was more pronounced. Curve 3 was obtained at $t=19$ min when the current was 0.18 mA and at its minimum point. The potential in the central region increased and the curve became more linear. Curve 4 was obtained at $t=2$ h when the current was 0.3 mA and increasing. This curve was similar to curve 3 and the curve became even more linear. Subsequently, curves 5, 6, and 7 were measured at higher

Table 4.1

The current levels at which the potential profiles were obtained for an as-grown MgO:Ni crystal. The curve number corresponds to that shown in Fig. 4.19.

Curve number	t	I(t) (mA)
1	0	0.8
2	10 sec	0.4
3	19 min	0.18 (min.)
4	2 h	0.30
5	5 h	0.70
6	20 h	9.65
7	22 h	17.8

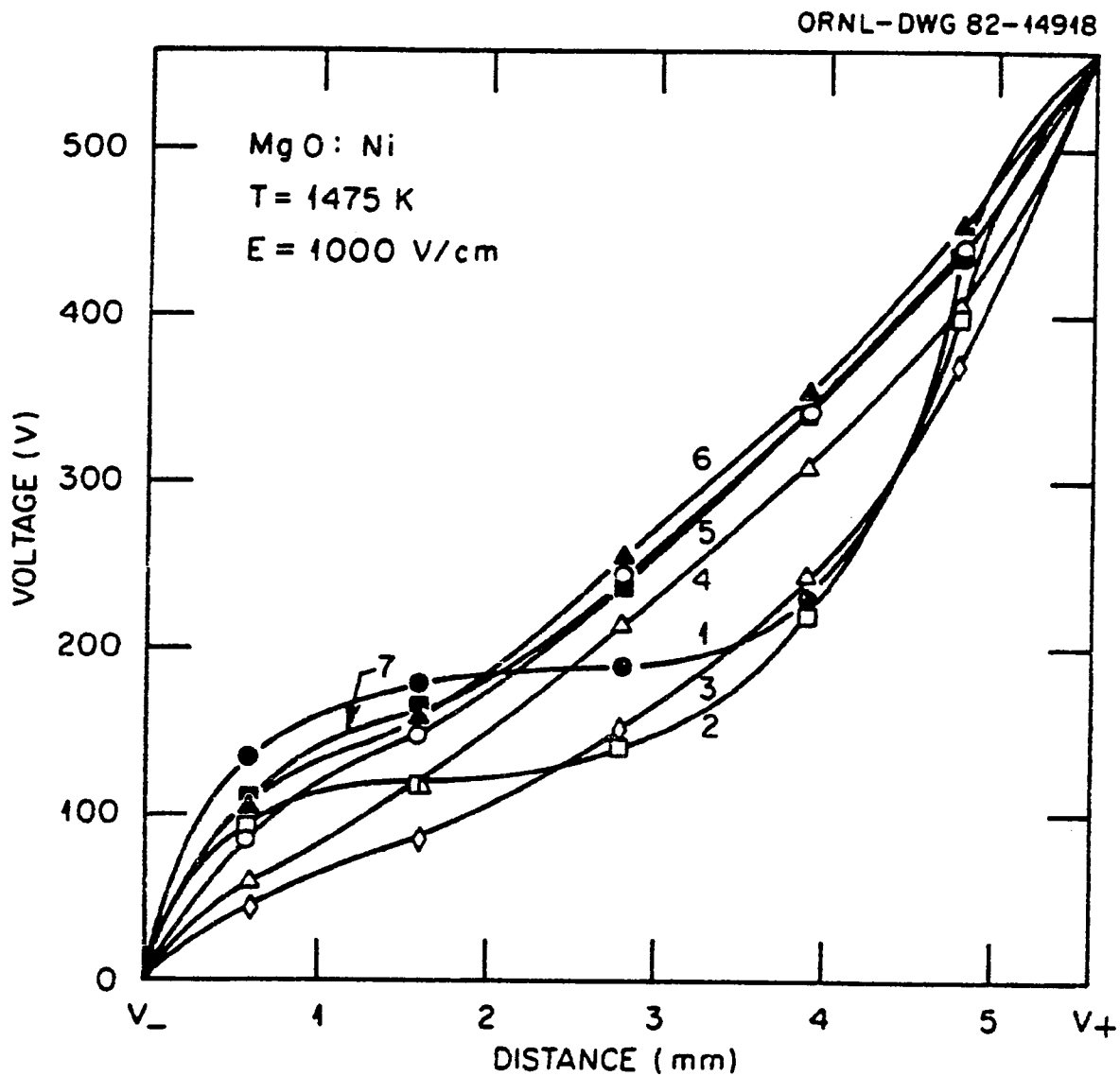


Figure 4.19 Potential profiles of MgO:Ni crystal at 1475 K using an electric field of 1000 V/cm. The profiles were measured at various stages during the current growth. The current levels at which the measurements were made were shown in Table 4.1.

current levels. These three curves were similar and, with increasing time, they approached linearity.

The residual potential profiles were measured at two different current levels at which the applied voltage was removed, as shown in Fig. 4.20. The top curve was obtained when current was 1.15 mA and increasing. The curve was negative quadratic near the cathode and positive quadratic near the anode. It can be shown, using the Poisson equation, that there are positive space charges near cathode and negative space charges near anode. This is evidence of residual heterocharges, space charges of opposite sign to that of the electrode, in the regions near the electrodes. The lower three curves were measured at 0, 40 sec, and 30 min after the removal of the applied voltage when the current reached 18 mA. These curves suggest that the heterocharges near the anode disappeared during the current increase. The voltage in the center region of the crystal became essentially constant shortly after the removal of the applied voltage.

Several interesting points are obtained from Figs. 4.19 and 4.20.

1) The potential profile varies with time and changes from nonlinear (curve 1 of Fig. 4.19) to nearly linear (curves 5,6, and 7) at higher current levels.

2) The distribution of the electric field obtained from the potential profile also varies with time.

3) Initially, the electric field strength is much higher in the regions near electrodes than in the central part of the crystal.

4) The distribution of the electric field becomes more uniform as the current rises. This indicates that the local electrical neutrality is more approached as the current increases.

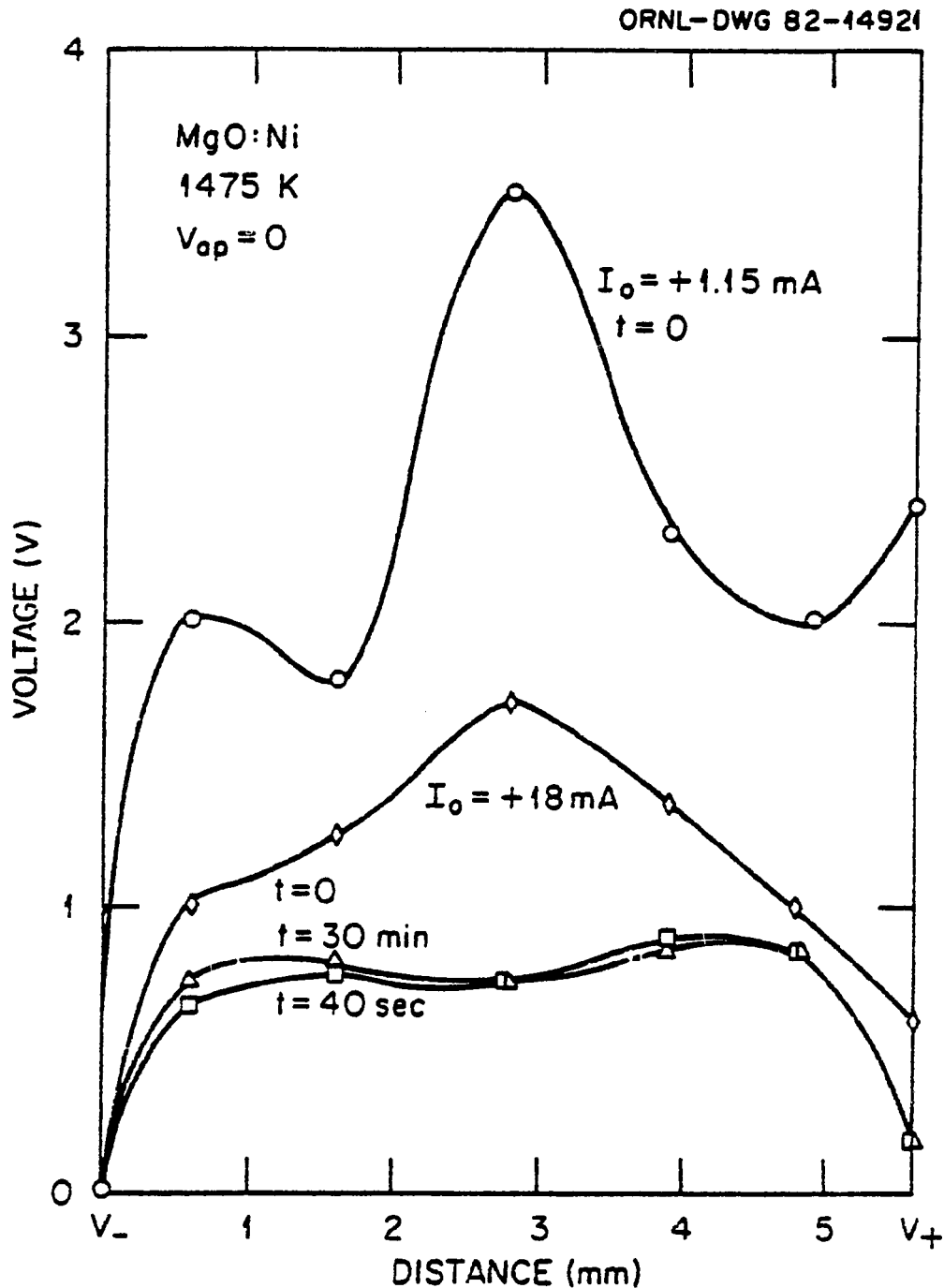


Figure 4.20 Residual potential profiles after the removal of the applied field. The top curve was measured when the field was removed at $I = +1.15 \text{ mA}$. The lower three curves were measured at 0, 40 sec, and 30 min after the removal of the field when current reached $+18 \text{ mA}$.

5) From the potential profiles, there is no evidence to show that heterocharge has been accumulated with time in the regions near the electrodes. Otherwise, the potential drop in the regions near the electrodes should increase with time and also the potential profile should become more nonlinear instead of linear.

6) The evidence of heterocharges near electrodes is clear at lower current levels but not clear at high current levels (Fig. 4.20).

7) The initial residual potential difference between the electrodes decreases as the current increases (Fig. 4.20).

b) Field Reversal

The potential profiles were also measured after the applied field was reversed at 18 mA. The current levels at which the measurements were made are shown in Table 4.2. Several sets of measurements were made in subsequence and were plotted in the corresponding curves of Fig. 4.21. Curve 1 was obtained at $t=0$, immediately after the applied voltage was reversed. The curve showed a nonlinear potential distribution. The potential drop was higher in the region near the new cathode than near the anode. Curve 2, obtained at $t=1$ min when current was -1.8 mA and decreasing, was similar to curve 1 except that the potential drop near the cathode had increased and that near the anode decreased. Curve 3, obtained at $t=11$ min when the current was -0.9 mA and was also decreasing, was similar to curve 2 but the potential value inside the sample was lowered and hence the potential drop was increased in the region near the anode but decreased in the region close to the cathode. Curve 4 was obtained at $t=43$ min when the current was at its minimum. The curve was similar to curve 3 but had a higher potential drop near the anode. Subsequently, curves 5, 6, 7, and 8 were measured

Table 4.2

The current levels at which the potential profiles were obtained after the reversal of the applied voltage. The sample is the same one as mentioned in Table 4.1. The curve number corresponds to that shown in Fig. 4.21.

Curve number	t	I(t) (mA)
1	0	-16.5
2	1 min	- 1.8
3	22 min	- 0.9
4	43 min	- 0.8 (min.)
5	1 h	- 0.83
6	4.5 h	- 2.3
7	7.7 h	- 6.8
8	12.5 h	-17.2

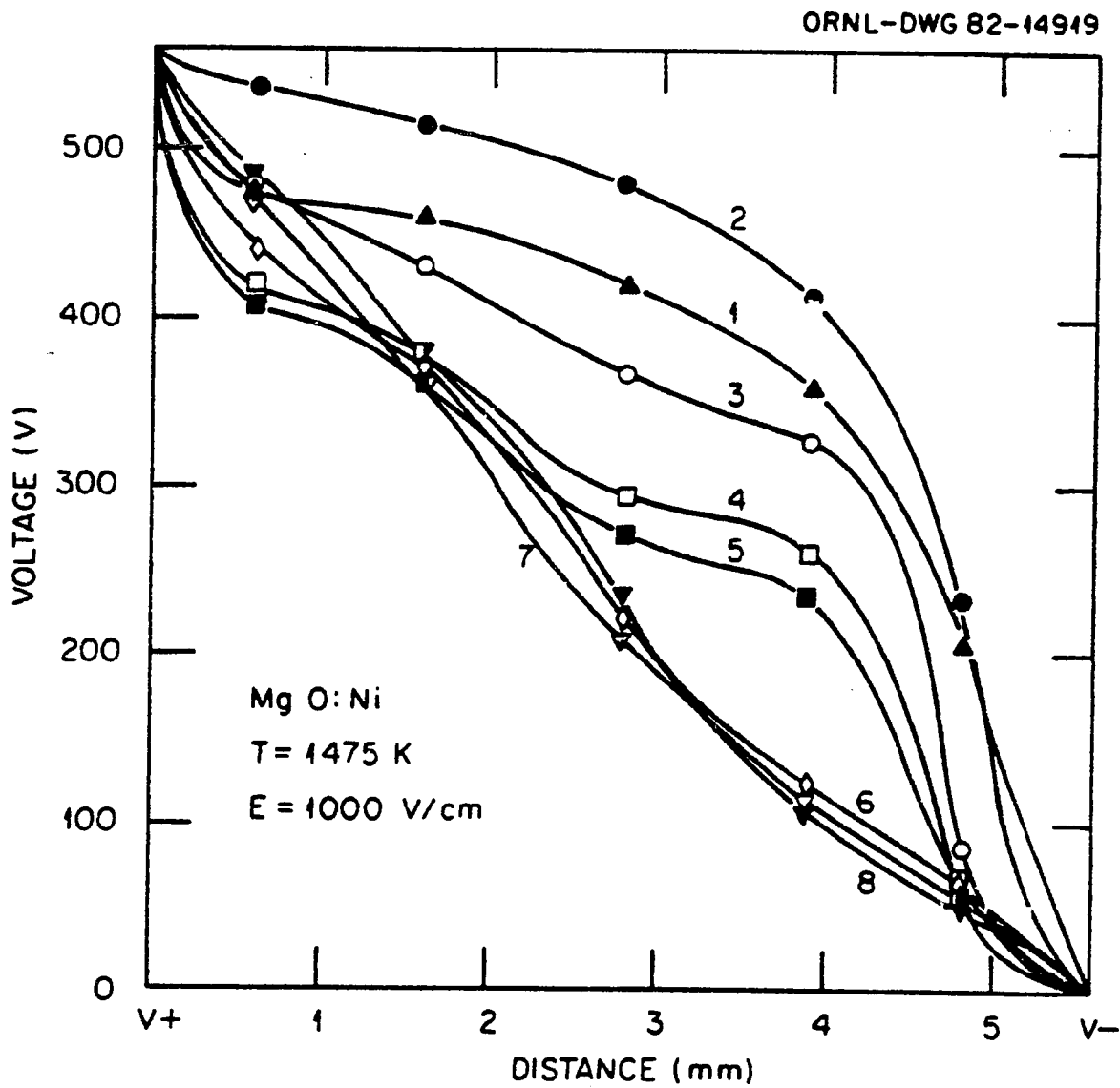


Figure 4.21 Potential profiles after the field reversal. The profiles were measured after the field was reversed at $I = 18 \text{ mA}$. The current levels at which measurements were made were shown in Table 4.2.

while the current was increasing. The potential curves became more linear at higher current levels.

The residual potential profiles after the reversal were measured when the currents reached -3.7 mA and -17.5 mA. Several sets of measurements were made in sequence after the removal of the applied voltage, as shown in Fig. 4.22 and 4.23. The shape of the profiles were similar in both figures. The potential value obtained from -3.7 mA was twice as high as that obtained from -17.5 mA. Both figures showed that the central point of the residual potential curve became essentially constant at about 1 min after removal of the applied voltage. The heterocharges seemed to be accumulated with time in the region near the cathode.

4.17 Atmospheric Effect

The dielectric breakdown of MgO crystals at high temperatures was also investigated in oxygen and nitrogen atmospheres. The characteristic times for breakdown were lower in both cases than in air. The breakdown of MgO:Ni crystals at 1473 K was also performed, using an electric field 1500 of V/cm, in pure oxygen ($P(O_2) = 1$ atm) and pure nitrogen ($P(N_2) = 1$ atm, $P(O_2) < 10^{-5}$ atm) atmospheres. The results are shown in Fig. 4.24 and the characteristic times for breakdown are tabulated in Table 4.3. In both oxygen and nitrogen atmospheres, the current behavior was similar. In the first hour, the current increased more rapidly in oxygen or nitrogen atmosphere than in air. At $t = 1$ h, the current in oxygen or nitrogen atmosphere was about one order of magnitude higher than that in air. Subsequently, the currents increased exponentially with nearly the same time constant. The increase of current was more stable in air than in either oxygen or nitrogen

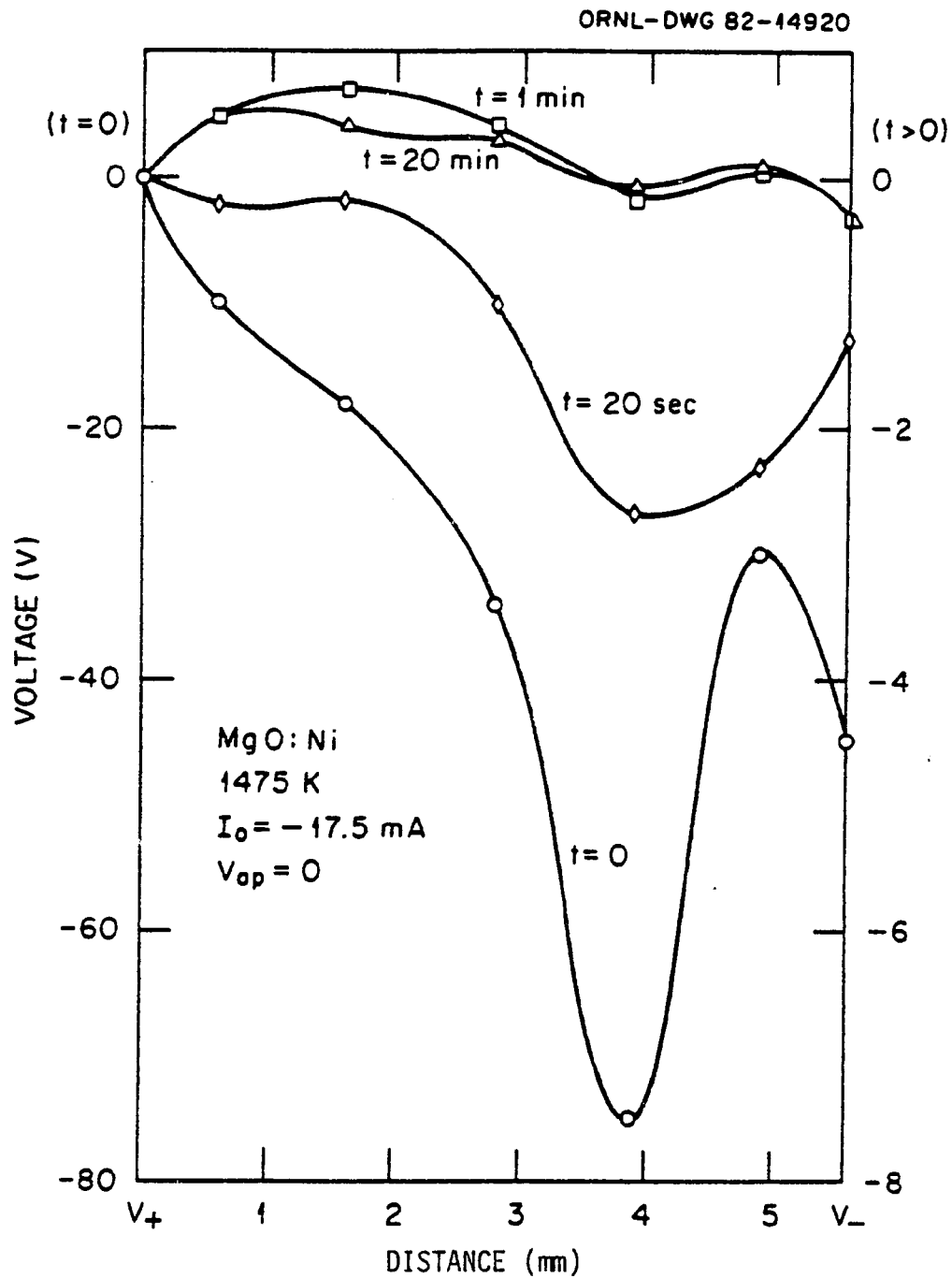


Figure 4.23 Residual potential profiles measured at $I = -17.5 \text{ mA}$. The profiles were measured at 0, 40 sec, 1 min, and 20 min after the field removal.

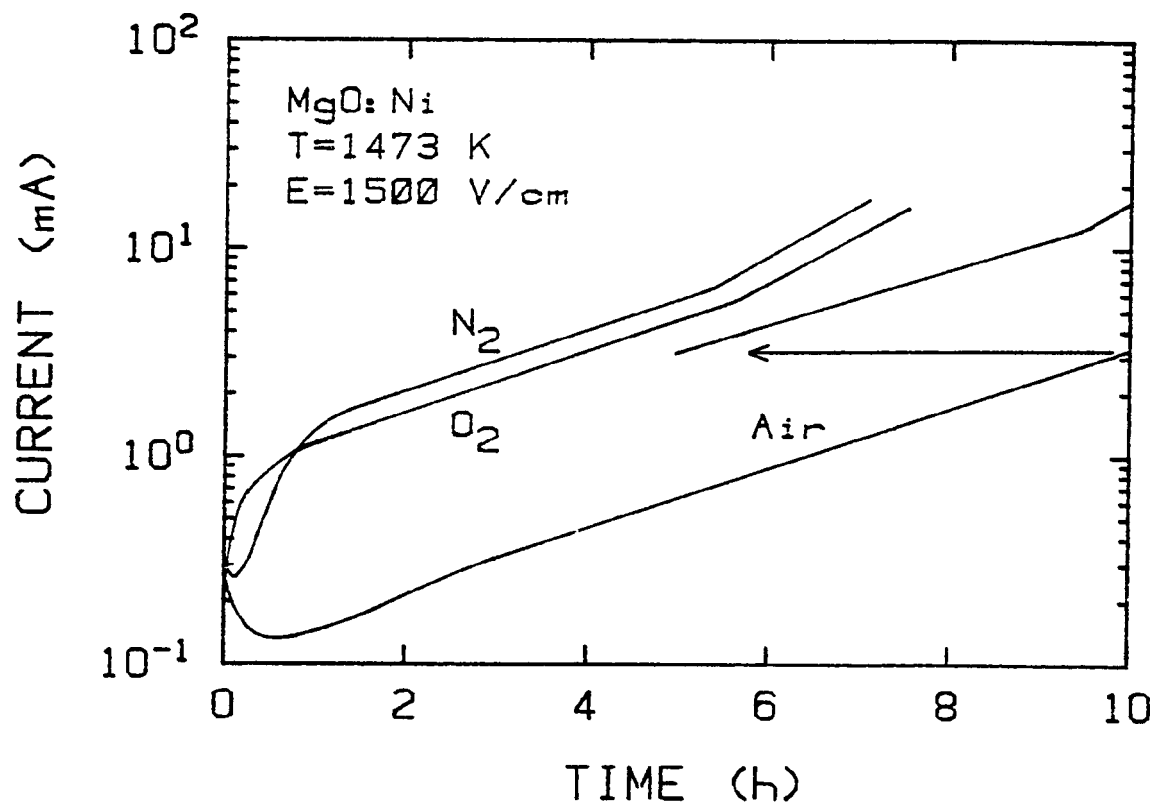


Figure 4.24 The effect of atmospheric conditions on the current behavior of MgO:Ni crystals. The log of current is plotted vs time. Three different atmospheres were used: pure oxygen, pure nitrogen, and air.

Table 4.3

The characteristic time for breakdown, t_c , of MgO:Ni crystals in different atmospheres. The measurements were performed at 1473 K using an electric field of 1500 V/cm.

Atmosphere	t_c (h)
Air	16
N ₂	7.0
O ₂	7.5

atmosphere at high current levels. It is also noted that the crystal lasts twice as long in air than in either oxygen or nitrogen atmosphere.

4.1.8 Electrode Effect

The breakdown characteristic depends strongly on the electrode material. Four kinds of electrode materials were used: platinum, rhodium, iridium, and graphite. Because most of those materials, especially Ir and graphite, are easily oxidized in air at high temperatures (36,53), all the measurements have been performed in dry flowing nitrogen atmosphere. Both cathode and anode were of the same material.

Electrode material has a direct influence on the current behavior and hence the characteristic time for breakdown, as shown in Fig. 4.25 and Table 4.4. In the first 30 minutes after the application of the voltage, the current behaved differently for different electrode materials. Graphite and iridium electrodes provided a similar initial current behavior. Both currents increased rapidly to a maximum, and then decreased to a minimum before their exponential increases. Platinum and rhodium electrodes exhibited a similar current behavior as described previously (see Fig. 4.24). After 30 minutes all four materials displayed an exponential current increase. Pt, Rh, and graphite increased with almost the same time constant. In the case of Ir, the time constant was about four times smaller and therefore resulted in a shorter breakdown time. The characteristic times for breakdown of MgO:Ni crystals at 1473 K using an electric field of 1500 V/cm in dry nitrogen atmosphere for Ir, graphite, Rh, and Pt electrodes were 2, 4, 5, and 7 h, respectively. Different electrodes were also used simultaneously as cathode and anode, the current behavior described above was found to be determined primarily by the cathode electrode.

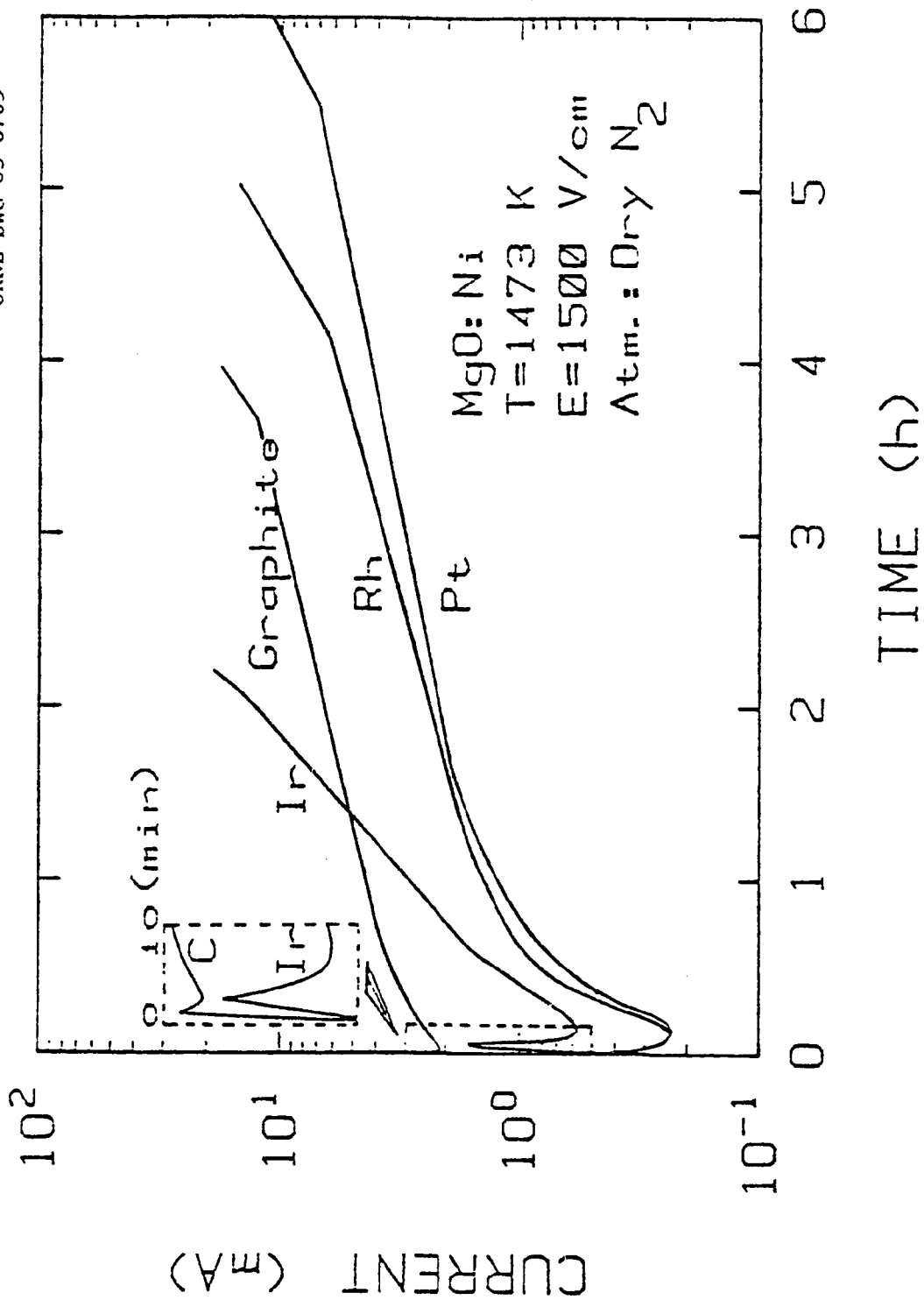


Figure 4.25 The effect of electrode material on the current behavior of MgO:Ni crystals. Samples were treated at 1473 K with the use of an electric field of 1500 V/cm in flowing dry N₂. Four different electrodes were investigated: Ir, Graphite, Rh, and Pt.

Table 4.4

The characteristic times for breakdown, t_c , and the activation energies, Q , of MgO:Ni crystals using different electrode material. The measurements were performed at 1473 K using an electric field of 1500 V/cm in flowing dry nitrogen atmosphere.

Electrode Material	t_c (h)	Q (eV) (± 0.1)
Ir	2	2.9
Graphite	4	*
Rh	5	2.7
Pt	7	2.6

*Not measured (see text).

The activation energies obtained from the temperature-dependence of short-circuit current using different electrode materials in dry nitrogen atmosphere are shown in Table 4.4. They are ranging from 2.6 to 2.9 ± 0.1 eV. Usually, the short-circuit current flowed in the direction opposite to the original current and lasted for a long time. In the case of graphite electrodes, the short-circuit current (measured from $I_0 = +18$ mA), flowing in the same direction as the original current, decreased from about 3 mA to nearly zero in only 30 sec. Therefore, no activation energy could be obtained for the case using graphite electrodes.

4.2 Other Doped MgO Crystals

4.2.1 Effect of Impurities on Breakdown

An undoped MgO crystal typically required 22 hours for the current to reach 18 mA. Crystals doped with V, Cr, Fe, or Ni had lower characteristic times for breakdown and, therefore, were more susceptible to breakdown. However, it has been found that doping with H, Co, or Cu actually suppresses the dielectric breakdown. The results are illustrated in Fig. 4.26. The values of the characteristic times for breakdown of different samples are also tabulated in Table 4.5. It is noted that in the case of the MgO:Cu crystals (30 ppm), it requires more than 400 hours to reach 18 mA.

4.2.2 Effect of Impurity Concentrations

The concentration of the dopant affected the characteristic time for breakdown. The concentration dependence on the breakdown was investigated for the following dopants: Cu, Co, Ni, H, and Cr. The results indicate that it is not feasible to make generalizations either

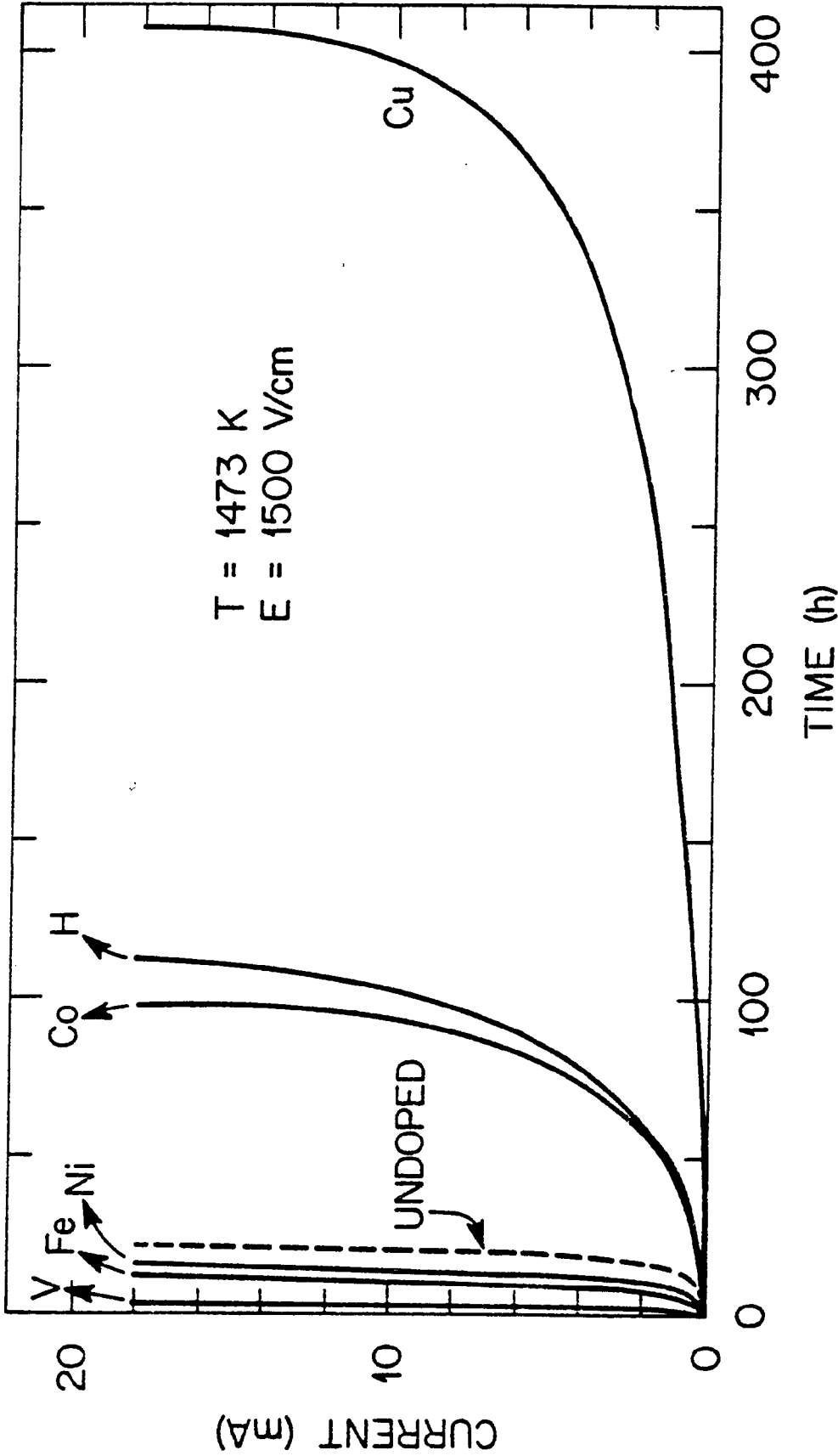


Figure 4.26 Current vs time at $T = 1473 \text{ K}$ with $E = 1500 \text{ V/cm}$ applied to doped and undoped MgO crystals. Crystals with V, Fe, or Ni have lower characteristic time for breakdown than the undoped one, but the crystals doped with Co, H, or Cu have higher characteristic time for breakdown.

for the class of dopants which serve as suppressors of breakdown or for those impurities which enhance breakdown. Each dopant needs to be considered individually.

a) Suppression of Breakdown: Cu and Co

The presence of Cu suppressed breakdown, or prolonged the lifetime of the MgO crystals. Figure 4.27 shows that high Cu concentrations were more effective in suppressing breakdown. A concentration of $1.5 \times 10^{18} \text{ cm}^{-3}$ (or 30 ppm) of Cu prolonged the lifetime of the material by a factor of 20. The characteristic time varied exponentially with the impurity concentration, as described by

$$t_c(n) = t_0 e^{\gamma n} \quad (4.7)$$

in the region between 10 and 30 ppm. Here $t_0 = 7 \text{ h}$, $\gamma = 2.6 \times 10^{-17} \text{ cm}^3$ (or 0.13 ppm^{-1}) and n is the concentration of Cu in cm^{-3} (or ppm). Note that the value of t_0 is lower than the actual 22 hours for undoped MgO, because this equation is not valid for $n < 10 \text{ ppm}$.

A similar effect was found for Co-doped MgO. The results are shown in Fig. 4.28. Equation (4.7) is valid for concentrations varying from zero to at least $1 \times 10^{20} \text{ cm}^{-3}$ (2000 ppm). The constants t_0 and γ for MgO:Co are 22 h and $1.5 \times 10^{-20} \text{ cm}^3$ ($7.3 \times 10^{-4} \text{ ppm}^{-1}$), respectively.

The concentration effect of hydrogen was not determined because hydrogen is a dynamic system with both the H_2 content in the cavities and the soluble H^+ concentrations change at 1473 K (6,25).

b) Enhancement of Breakdown: Cr and Ni

Chromium is one of several impurities which tend to enhance breakdown, or shorten the lifetime of MgO. Figure 4.29 shows that a

ORNL-DWG 82-17078

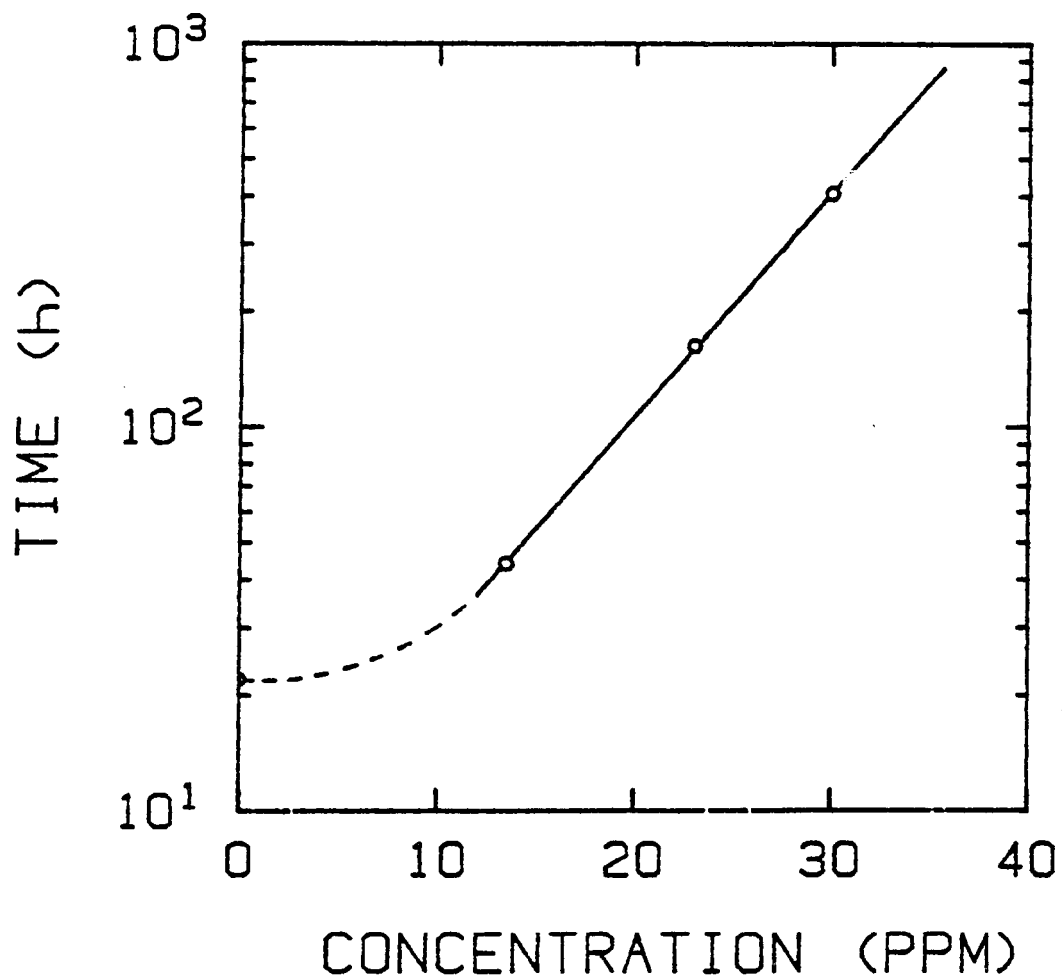


Figure 4.27 Log of the characteristic time for breakdown of MgO:Cu crystals vs dopant concentration.

ORNL-DWG 82-17075

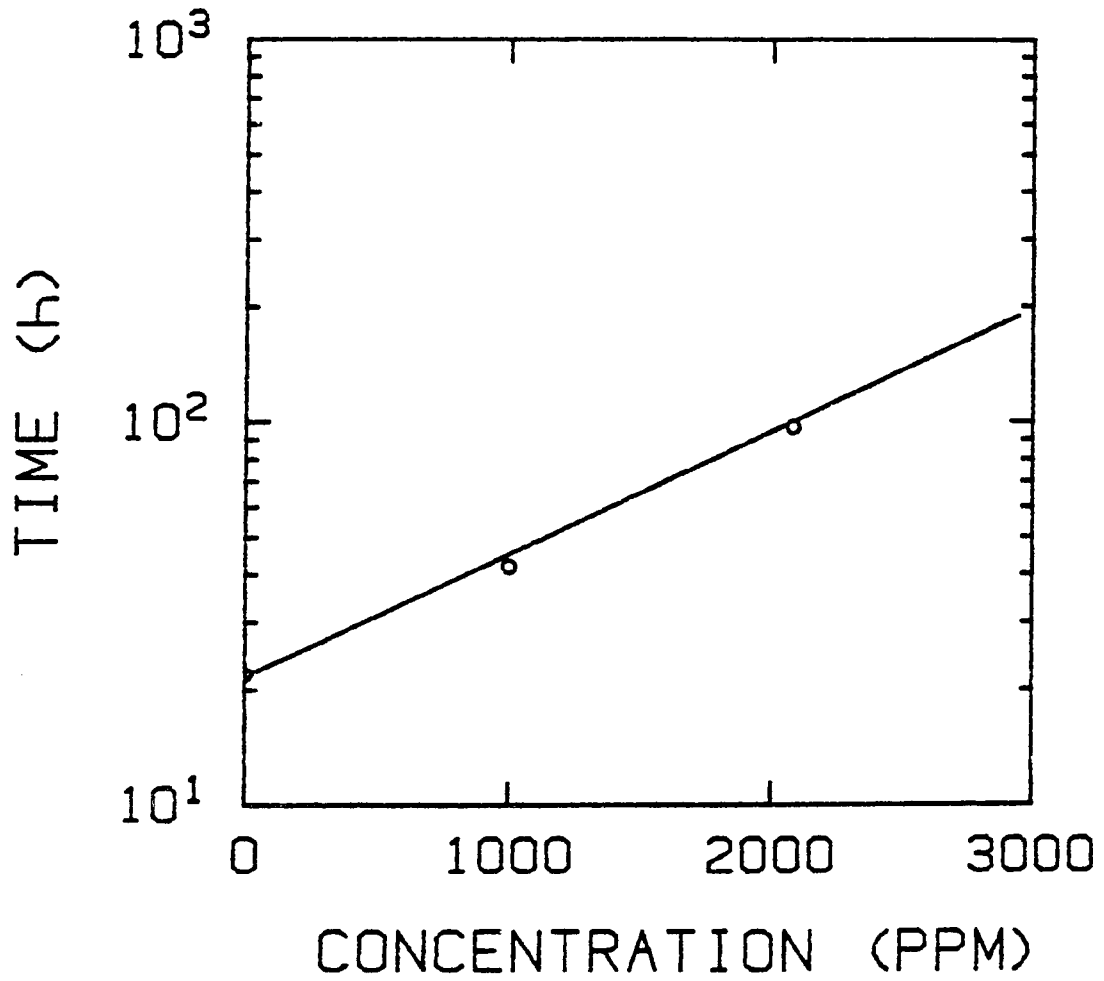


Figure 4.28 Log of the characteristic time for breakdown of MgO:Co crystals vs dopant concentration.

ORNL-DWG 82-17073

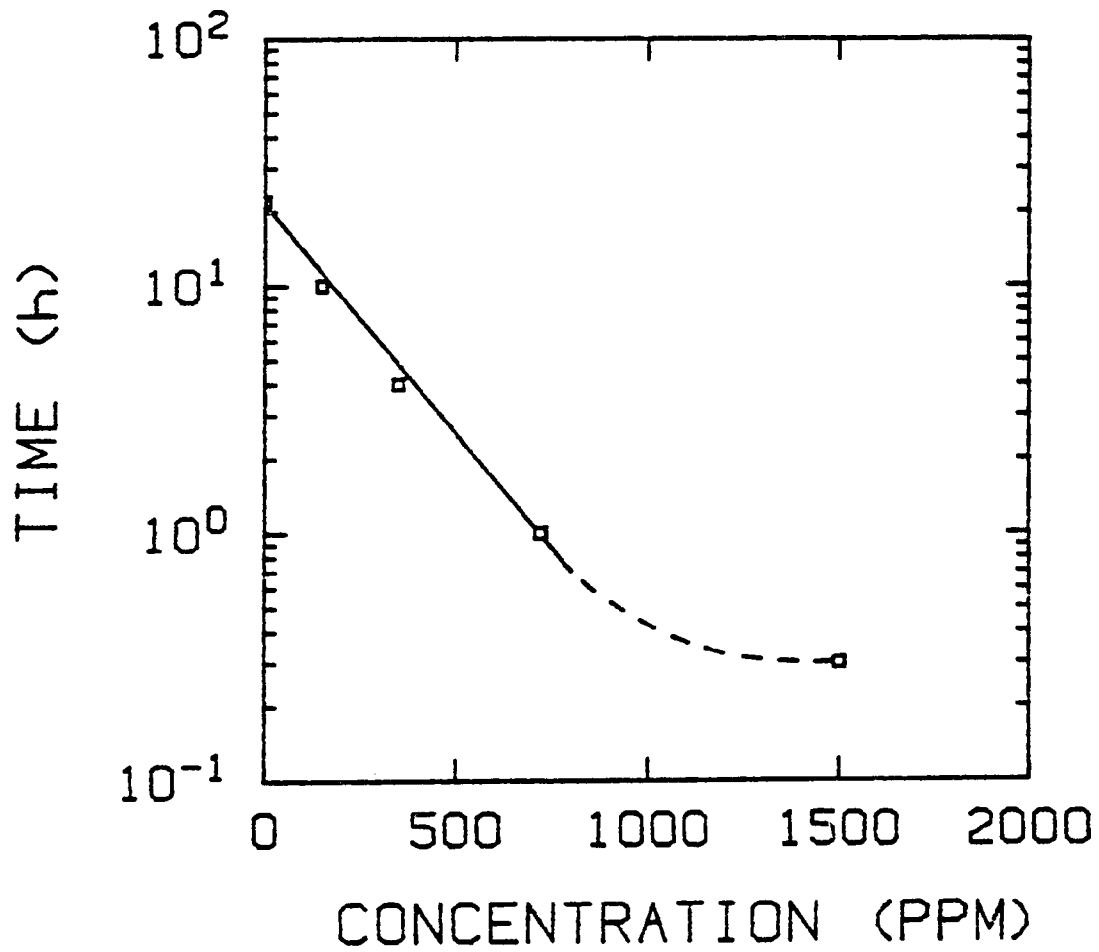


Figure 4.29 Log of the characteristic time for breakdown of MgO:Cr crystals vs dopant concentration.

higher concentration of Cr had a greater effect on enhancing breakdown. For concentrations less than $4 \times 10^{19} \text{ cm}^{-3}$ (800 ppm), the characteristic breakdown time obeyed the relationship

$$t_c(n) = t_0 e^{-\gamma n} \quad , \quad (4.8)$$

where $t_0 = 22 \text{ h}$ and $\gamma = 0.9 \times 10^{-19} \text{ cm}^3$ ($4.3 \times 10^{-3} \text{ ppm}^{-1}$). For concentrations exceeding 800 ppm, the characteristic breakdown time approached a constant.

Nickel in MgO also enhanced breakdown. However, the concentration dependence was not monotonic, as shown in Fig. 4.30. There appear to be three regions in the curve. The first region corresponds to concentrations less than $1.5 \times 10^{19} \text{ cm}^{-3}$ (300 ppm) and the value of t_c can probably be described by Eq. (4.8). The constant t_0 is 22 h, but γ could not be determined since samples with nickel concentrations less than 300 ppm were not available. The second region corresponds to concentrations between 300 to 3000 ppm, and the value of t_c can be described by Eq. (4.7). The relevant constants are $t_0 = 0.38 \text{ h}$ and $\gamma = 0.2 \times 10^{-19} \text{ cm}^3$ ($1.0 \times 10^{-3} \text{ ppm}^{-1}$). Hence, the characteristic breakdown time increases exponentially with concentration in this region. For concentrations exceeding 3000 ppm, it is projected that the characteristic breakdown time eventually reaches a saturation value of 22 h.

4.2.3 Current Behavior

a) Field Reversal

As indicated previously, polarity changes were made when the current reached 18 mA. With each field reversal, the characteristic time diminished until a minimum value was reached. Usually, several

ORNL-DWG 82-17074

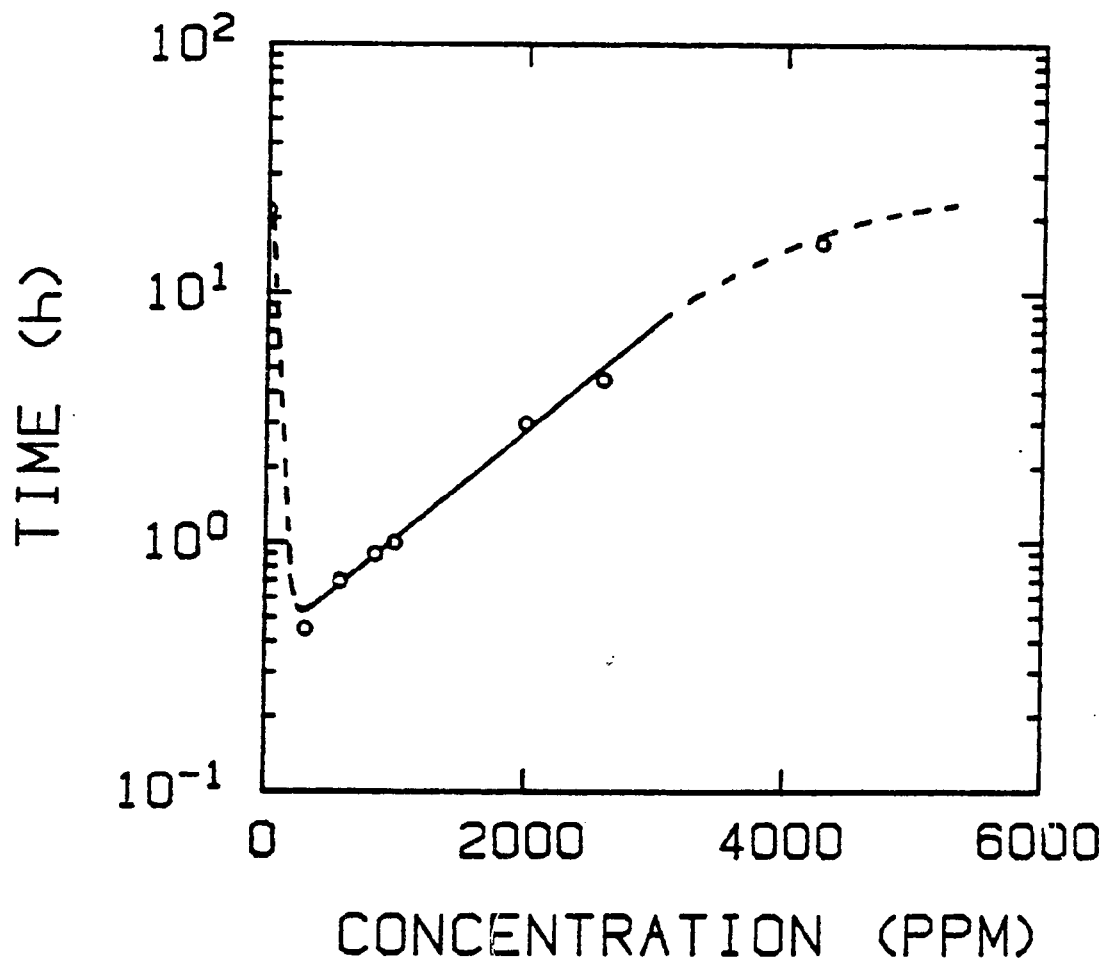


Figure 4.30 Log of the characteristic time for breakdown of MgO:Ni crystals vs dopant concentration.

reversals were made. Typically, after the tenth reversal, the characteristic time became constant. Figure 4.31 shows the current behavior in MgO:Cu (30 ppm) for the initial field application and five subsequent field reversals. The current behavior is similar to that for the MgO:Ni crystals (Fig. 4.1), except the time scales are longer.

The details in Fig. 4.31 can be described as follows: The field was applied at $t = 0$ after the sample had been heated at 1473 K for about 10 minutes to ascertain that the sample temperature had reached equilibrium. The current initially decreased from 0.1 mA to 0.03 mA in 3 hr (top inset), and then increased at an exponential rate until 18 mA was reached, requiring about 406 h. The field was then reversed. The instantaneous reversed current in the opposite direction was 15 mA. The current then decreased to a minimum value of 0.08 mA in 2.5 h (lower inset), followed by an exponential increase which was faster than that in the first cycle. The characteristic time for this cycle was only 115 h. Several more field reversals were performed subsequently. The current behavior was similar to that of the first reversal, but the characteristic time diminished with each reversal, until ultimately only 17 h were required, as shown in the top curve of Fig. 4.32.

Other samples with different dopants showed similar current-vs-time (I-t) behavior but with different characteristic times, as shown in the lower curves of Fig. 4.32. The characteristic times for the first cycle, t_{c1} , and the minimum values resulting from several subsequent reversals, t_{cf} , for different samples are tabulated in Table 4.5, respectively. In general, the initial I-t behavior was followed by predictable I-t curves upon subsequent field reversals. For example, the six representative curves shown in Fig. 4.32 behave in a similar fashion

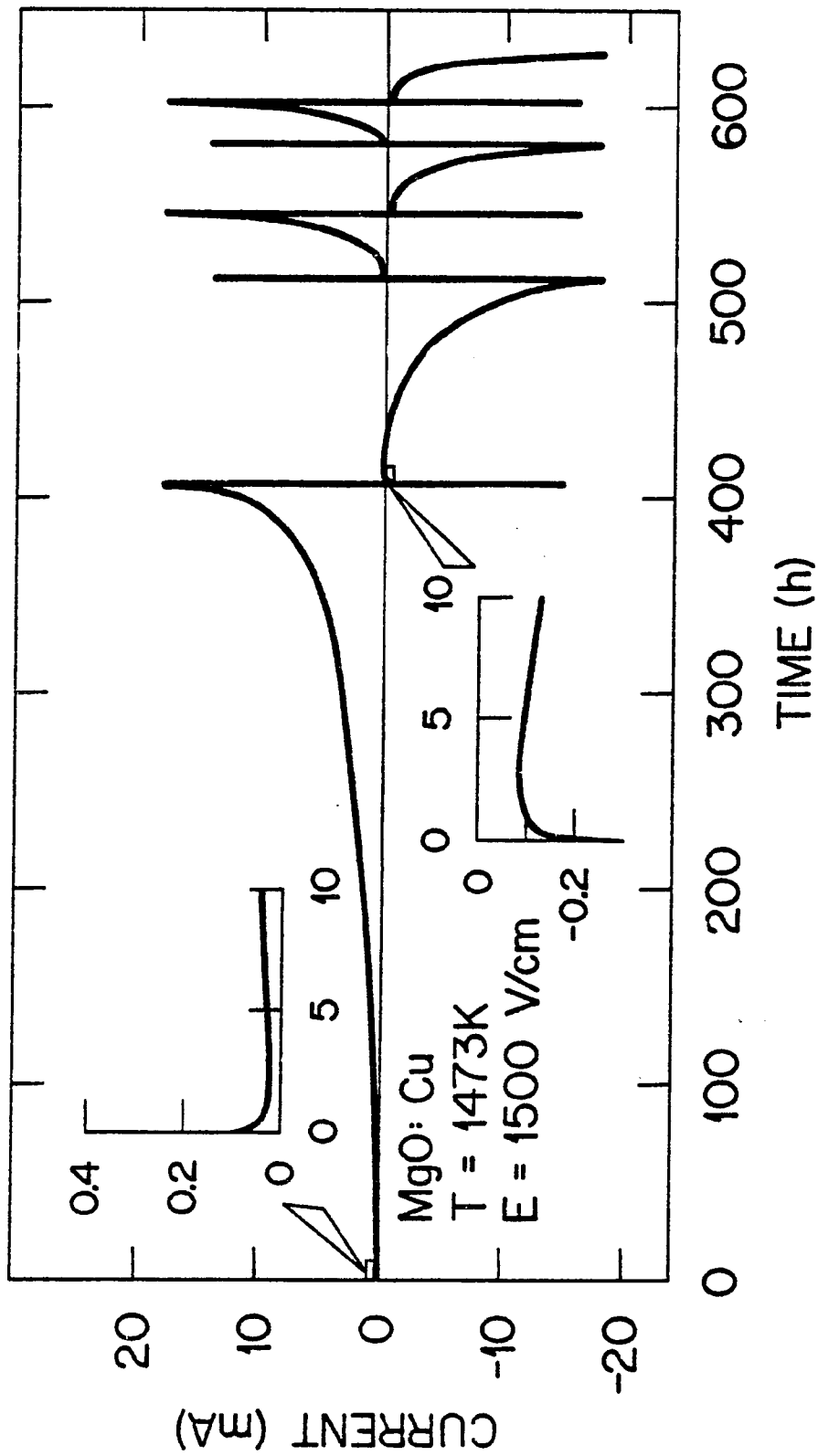


Figure 4.31 Current vs time at 1473 K with $E = 1500$ V/cm applied to MgO:Cu (30 ppm) crystal for several polarity reversals.

ORNL-DWG 82-17071

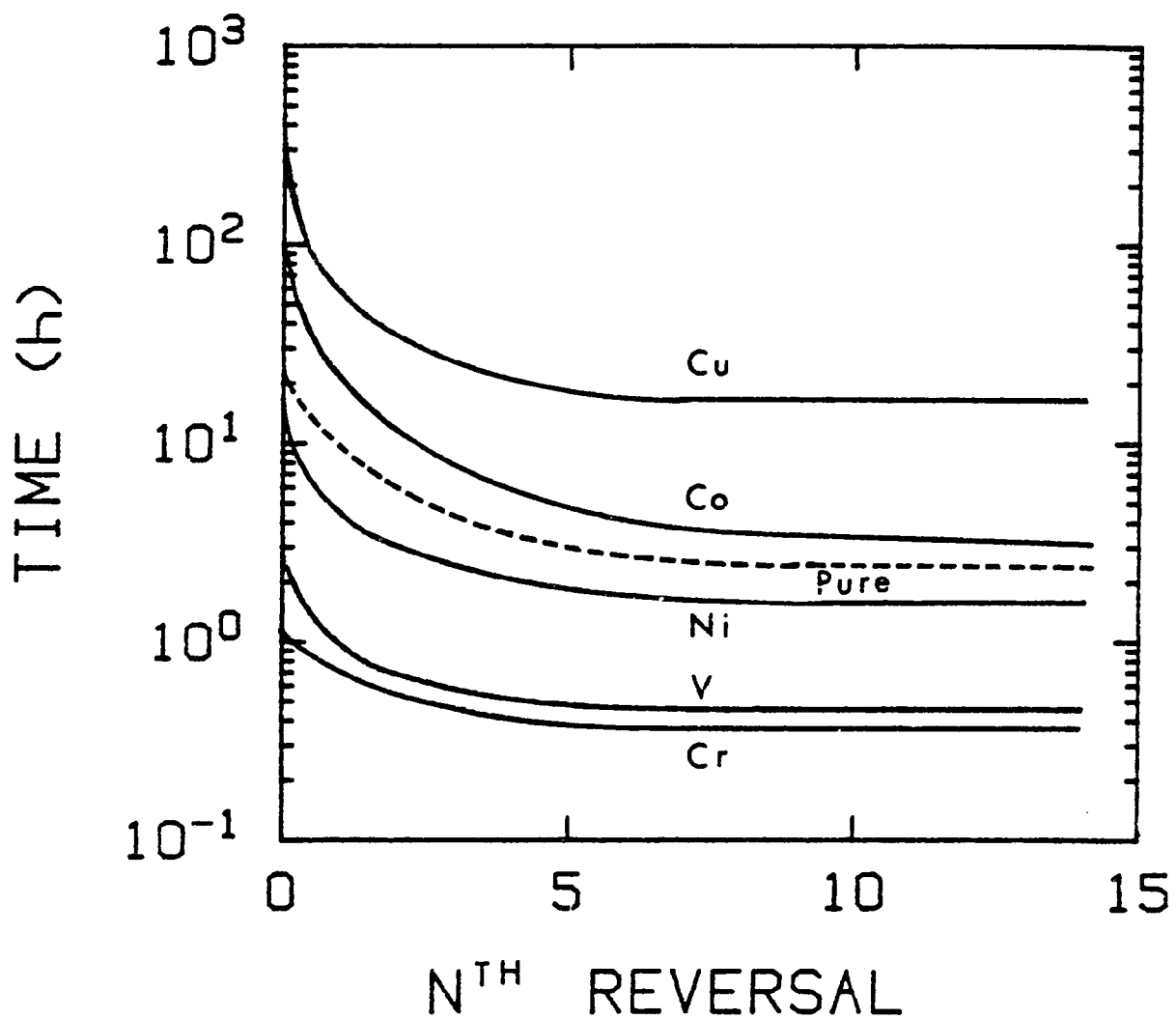


Figure 4.32 Log of the characteristic time for breakdown vs the nth field reversal for doped and undoped MgO crystals.

Table 4.5

Characteristic times for the breakdown of MgO crystals at 1473 K and 1500 V/cm. Column 2 corresponds to the concentration of dopants tabulated in column 1. Column 3 lists the characteristic times for breakdown in the first cycle, while column 4 tabulates subsequent characteristic times which had reached a minimum value.

Sample	[n](ppm)	t_{c1} (h)	t_{cf} (h)
MgO	< 100*	22	2.4
MgO:Ni	4280 1000	16 1	1.8 0.5
MgO:Fe	1000	12	1.5
MgO:Co	2080	95	3.2
MgO:Cu	30	406	17
MgO:V	350	3	0.5
MgO:Cr	720	1	0.4
MgO:H	---	110	---

*Total impurity.

and there is no indication of any crossovers. Given the initial characteristic times, it is possible to extrapolate subsequent times due to field reversals.

b) Reversed Current

The current after reversal of the applied field can be described as the sum of two exponentials, as shown in Eq. (4.1) and rewritten as follows

$$I(t) = I_{01} e^{-t/\tau_1} + I_{02} e^{t/\tau_2}, \text{ for } t < 0 \quad (4.9)$$

where I_{01} , I_{02} , τ_1 , and τ_2 are positive constants, and $I_{01} > I_{02}$, $\tau_1 < \tau_2$. The above equation shows a minimum in $I(t)$ at time denoted by t_m , which is obtained to be

$$t_m = (\tau_1 \tau_2 / \tau_1 + \tau_2) \ln(I_{01} \tau_2 / I_{02} \tau_1) \quad (4.10)$$

The relationships

$$\tau_2 \gg \tau_1 \quad (4.11)$$

and

$$I_{01} \tau_2 \gg I_{02} \tau_1 \quad (4.12)$$

are always true in the first reversed cycle (the second treatment cycle). Substituting Eqs. (4.11) into Eq. (4.10), gives

$$t_m \sim \tau_1 \ln(I_{01} \tau_2 / I_{02} \tau_1) \quad (4.13)$$

It has been also found that a higher value of τ_2 is always associated with a higher value of τ_1 and the increase of $I_{01} \tau_2$ is greater than that of $I_{02} \tau_1$. Therefore, Eq. (4.13) indicates that a higher value of τ_2 ,

that is a longer breakdown time, results in a greater value of t_m . This is true for all the doped MgO crystals, as shown in Fig. 4.33.

4.2.4 Activation Energy

The activation energy associated with the breakdown of MgO crystals was obtained by three different methods: time-constant τ_2 of $I(t)$, short-circuit current I_{SC} , and alternating current I_{AC} , as described previously in Section 4.1.2.

The activation energies obtained from MgO crystals ranged from 2.1 to 2.8 eV, as shown in Table 4.6. The methods of τ_2 and I_{SC} provide the same activation energy for each sample; the method of I_{AC} also yields the same value of activation energy except for the Cu- and Co-doped MgO crystals in which lower activation energies are measured by using either τ_2 or I_{SC} .

Impurities and their concentrations play an important role in determining the lifetime of MgO crystals against dielectric breakdown. The results can be summarized as follows (91):

- 1) The presence of Cu, Co, or H suppresses the breakdown and prolongs the lifetime of MgO crystals used as an electrical insulator at high temperatures. In the case of crystals doped with 30 ppm Cu, the characteristic time for breakdown is twenty times longer than that of the undoped crystals.
- 2) The presence of Fe, Ni, Cr, or V enhances breakdown.
- 3) The characteristic time for breakdown is determined not only by the dopant, but also its concentration.
- 4) Given the I-t behavior in the first cycle for any dopant in MgO, it is possible to make reasonable predictions on the I-t characteristics for subsequent field reversals.

ORNL-DWG 82-17072

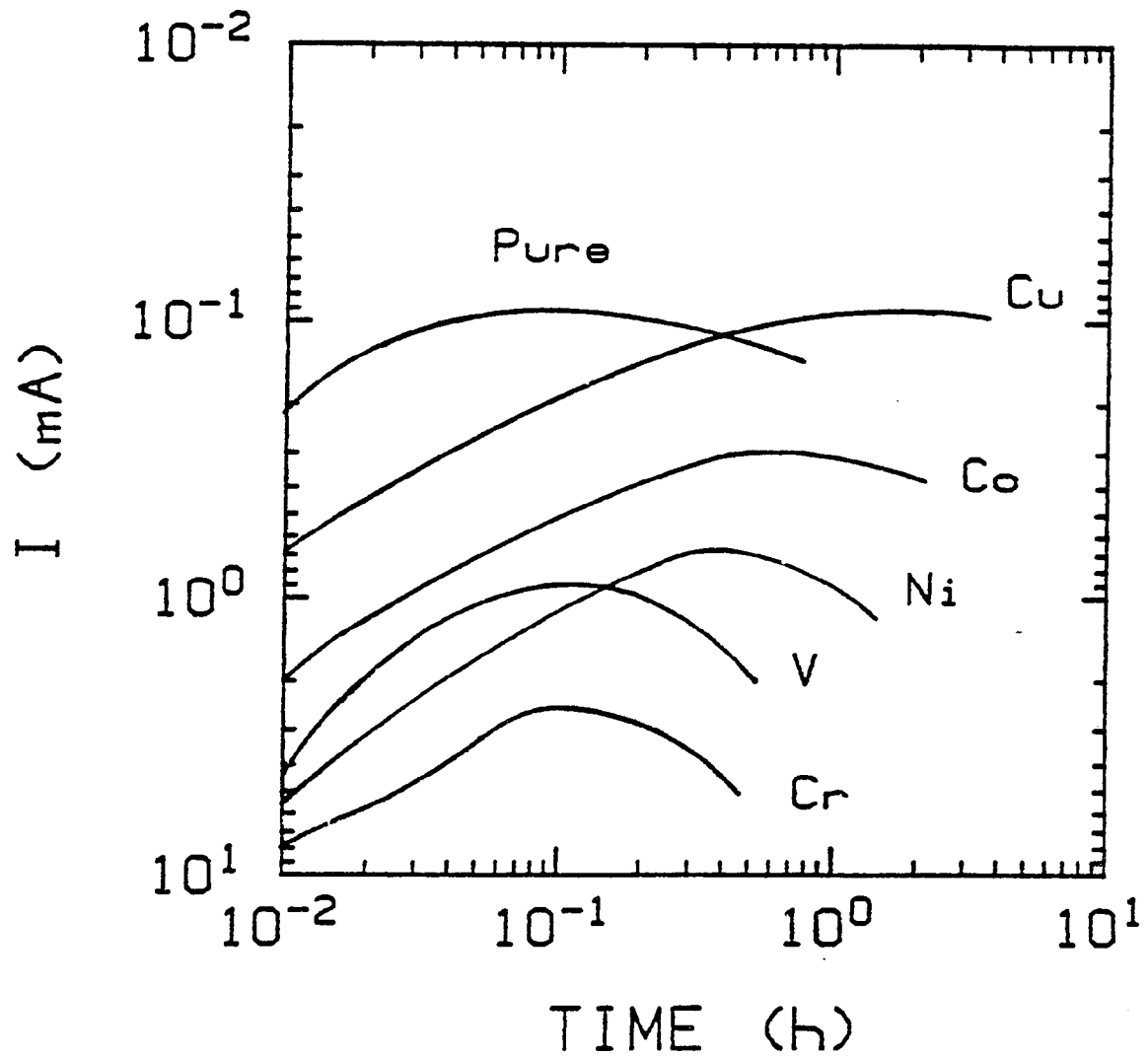


Figure 4.33 The behavior of the first reversed currents of doped and undoped MgO crystals. The applied field was reversed at $I = 18$ mA.

Table 4.6

Activation energies for the breakdown of MgO crystals. Activation energies shown were measured by three methods, short-circuit current I_{sc} , time constant τ_2 , and alternating current I_{ac} .

Sample	[n](ppm)	Activation Energy (eV)		
		I_{sc}	τ_2	I_{ac}
MgO	< 100**	2.4*	2.3	2.4
MgO:Ni	4280	2.4	2.3	2.4
	1000	2.6	---	---
MgO:Fe	1000	2.8	2.7	2.7
MgO:Co	2080	2.2	2.1	2.6
MgO:Cu	30	2.2*	2.1	2.7
MgO:V	350	2.7	2.7	2.7
MgO:Cr	720	2.6	2.6	---
MgO:H	---	2.6	---	2.5

*The values of I_{sc} are small compared with the background noise and the results are only estimated.

**Total impurity.

Chapter 5

DISCUSSION AND CONCLUSION

In this Chapter the experimental results of the dielectric breakdown of MgO crystals at high temperatures are discussed in terms of existing models described in Chapter 2. None of these models are compatible with the experimental results. However, a simple breakdown model based on this investigation and proposed by Tsang, Chen, and O'Dwyer (90) can satisfactorily explain most of the experimental results. The latter part of this chapter will be devoted to the description of this model.

5.1 Comparison with the Existing Models

There are several models which have been suggested for the dielectric breakdown of solids, as described in Chapter 2. Only two of them, thermal breakdown and space-charge-enhanced breakdown, will be discussed here because they have been the most widely accepted models.

Although thermal breakdown is possible at high temperatures, there are two experimental facts that cannot be explained by this mechanism. First, the reversed current decreases from an instantaneous current with the same magnitude as the current before the field reversal to a minimum value before its exponential increase (Fig. 4.1). This shows that the increase of the current and, therefore, the cause of the breakdown is not mainly due to the thermal effect (Joule heating). Joule heating is independent of the direction of the current and therefore reversing the

polarity should not lead to a decrease in the current. Secondly, the ac treatment did not produce the breakdown (Fig. 4.9). On the other hand, the alternating electric field should produce a faster thermal breakdown, since the power loss in a dielectric generally increases with frequency.

Undoubtedly, the Joule heating should enhance the breakdown process and eventually the material would suffer thermal breakdown. This was observed in some cases when currents were allowed to exceed the 18 mA limit; the samples broke down when the current rose an order of magnitude or more beyond 18 mA.

Assuming that the temperature dependence of the electrical conductivity at high current levels follows the Arrhenius-type law Eq.(2.2), then we can use Eq.(2.36) to estimate the current density (or electrical conductivity) required for thermal breakdown at constant voltage. Equation (2.36) is rewritten as

$$V_{OC}^2 \sim 8kk_0 T_0^2 / \phi \sigma \quad (5.1)$$

where σ is the electrical conductivity at ambient temperature. Using the known values, thermal conductivity $k = 6.5 \times 10^{-2}$ j/scm °K (24), $k_0 = 0.86 \times 10^{-4}$ eV K⁻¹, $\phi \sim 2.5$ eV, $T_0 = 1473$ K, and $V_{OC} = 375$ V, we obtain $\sigma \sim 4.5 \times 10^{-4}$ Ω cm⁻¹ at the onset of thermal breakdown. At 18 mA the conductivity σ is $\sim 4 \times 10^{-5}$ Ω ⁻¹ cm⁻¹, so that the theoretical estimate also places the onset of thermal breakdown at a current at least one order of magnitude higher than 18 mA. This gives further support that the breakdown of MgO crystals at high temperatures is not initiated by the thermal breakdown mechanism.

The space-charge-enhanced model which was proposed independently by Cooper and Elliott (11), and O'Dwyer (71) has the same difficulty with the observed behavior of the reversed current. This model subscribes that the breakdown process is due to the buildup of the ionic-space charges near the cathode, as shown by the theoretical calculation in Fig. 2.3. It indicates that if the applied field is reversed, the reversed current would be expected to be small and then increase slowly, because the ionic-space charges need to be built up near the new cathode. This is contradictory to the observed phenomena in the reversed currents in Figs. 4.1, 4.4, 4.5, and 4.6 and potential profiles in Figs. 4.19 and 4.21.

The behavior of the reversed current also revealed that the current in MgO crystals is not due to impurity conduction or thermionic emission from the colloidal particles (38-40). These two mechanisms cannot explain the field directional dependence of the current.

Clearly, there is no existing model which can describe the behavior of the pre-breakdown current. In the following, a breakdown model proposed by Tsang, Chen, and O'Dwyer (90) is described. It gives excellent explanations of most of the experimental results described in Sec. 4.1. This model at present has not been refined sufficiently to predict the effects of atmospheric conditions and impurities.

5.2 A New Model for the Dielectric Breakdown of MgO Crystals at High Temperatures

In general, the current behavior of nominally pure and nickel-doped MgO crystals is similar; the main difference between them is the time scale. We conclude therefore that the mechanism for high field conduction and dielectric breakdown in these two crystals is basically the

same. In what follows a model -- double injection with drift of ionic species or vacancies -- for the conduction process that does offer a reasonable and consistent picture of the observed phenomena is described.

In the first place, the high current levels observed (18 mA from an electrode of 0.30 cm² area corresponds to a current density of 60 mA/cm²) must be explained in terms of two carrier (electron and hole) current flow. This can be deduced as follows.

Assuming that the current is ionic, with the use of the ionic conductivity given by Eq.(2.4), the ionic current density is

$$J = \sigma E = nz^2e^2DE/k_0T \quad (5.2)$$

Taking the known values $J = 60 \text{ mA/cm}^2$, $z = 2$, $T = 1473 \text{ K}$, $E = 1500 \text{ V/cm}$, and the diffusion coefficient $D \sim 10^{-12} \text{ cm}^2/\text{sec}$ (42,97), the ion concentration is calculated to be $n \sim 10^{25} \text{ cm}^{-3}$, which is impossibly large.

If it is now assumed that the current is single-carrier (electron or hole) space charge limited, substituting reasonable values of $\mu = 10 \text{ cm}^2/\text{VS}$, $\epsilon_r = 10$, and $L = 2.5 \text{ mm}$ for the case of MgO crystals in Eq.(2.14), the voltage required to inject a current density of 60 mA/cm² is

$$\begin{aligned} V &= (8JL^3/9 \epsilon_r \epsilon_0 \mu)^{1/2} \\ &= 9730 \text{ V.} \end{aligned} \quad (5.3)$$

This is much higher than the 375 V used.

The proposed model assumes that the dielectric initially contains a concentration of n_0 relatively mobile free electrons, and an equal concentration of p_0 immobile (trapped) holes, as shown in Fig. 5.1a.

Fig. 5.1b shows the notations used in the discussion of this model. The injection rates of the charge carriers from the electrodes are denoted as n_i for electrons and p_i for holes. Charge carriers are driven out of the dielectric with drift rates for n_d electrons and p_d holes. The platinum electrodes are assumed to provide an ohmic contact for electrons and a very weakly injecting contact for holes, which means that $n_i > n_d$ for all t , and $p_i \ll n_i$. From Eq.(2.25)

$$J = AT^2 \exp\{-(\phi - \Delta\phi)/k_0 T\}, \quad (5.4)$$

the thermionic-emitted electron current density is

$$J > 700 \text{ mA/cm}^2, \quad (5.5)$$

assuming $\phi - \Delta\phi = 2.5$ eV. This value of J indicates that the cathode should have the capacity to inject electron current high enough to initiate the thermal breakdown. In the subsequent discussion electron-hole recombination is assumed to be very small.

At $t=0$, the application of a voltage then generates a current which is primarily contributed by those carriers generated thermally. Since the electron mobility is much greater than the hole mobility, the initial current density is then expressed as $J = n_0 e \mu_n E \sim p_0 e \mu_n E$. Taking an electron mobility of $10 \text{ cm}^2/\text{Vs}$, the initial current density of 0.67 mA/cm^2 then requires a trapped hole density of $2.8 \times 10^{11}/\text{cm}^3$. This is similar to the case of a trap-free insulator with thermal free carriers and low injection level, which has been solved in detail by Lampert and Mark (48). Using Eqs.(2.18) and (2.20), the dimensionless parameters w_a and u_a are calculated to be

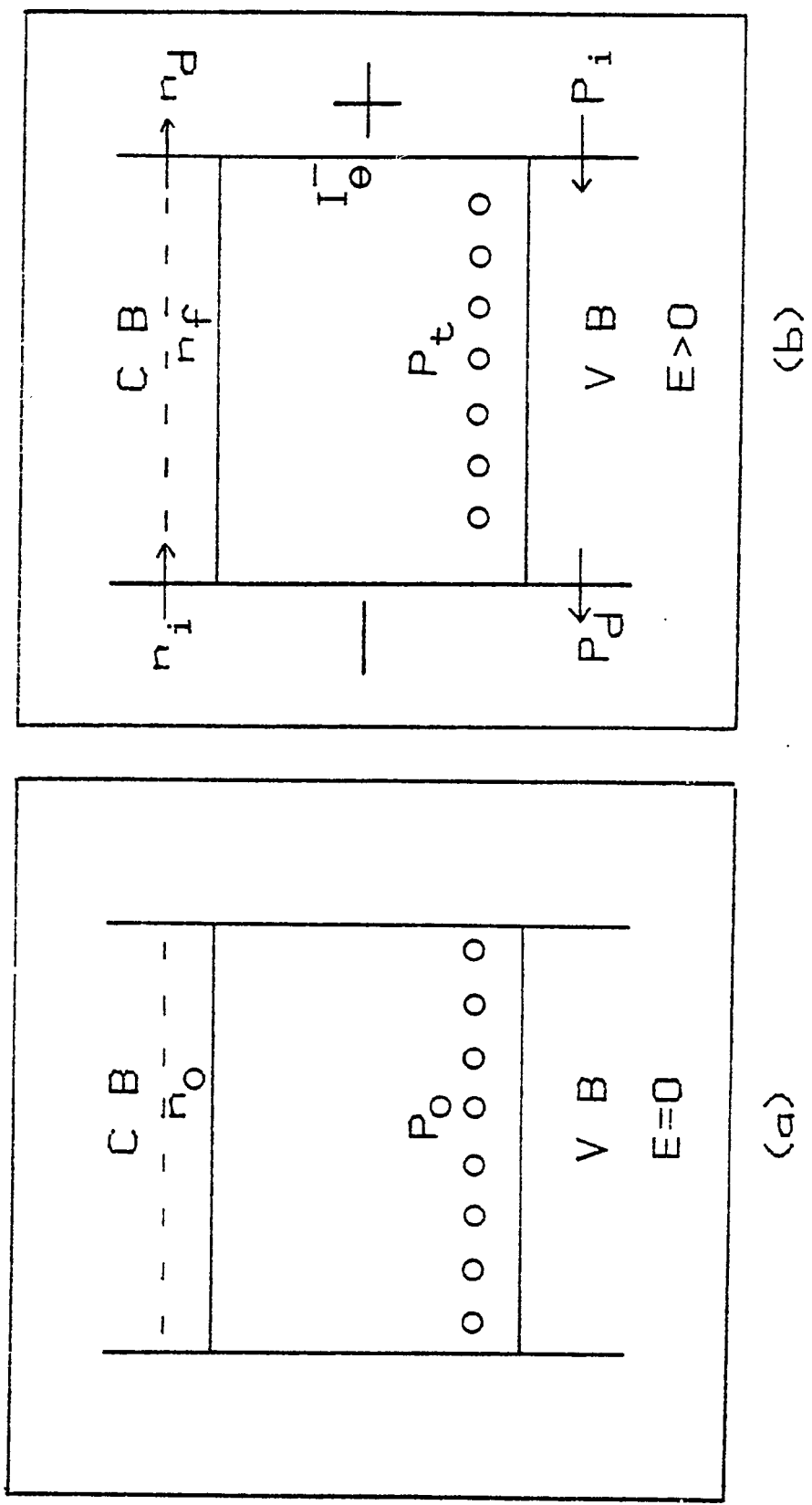


Figure 5.1 (a) Thermal equilibrium of charge carriers. The dielectric contains n_0 relatively mobile-free electrons, and an equal number of p_0 of high immobile (trapped) holes. (b) Diagram of notations used in the injection model. The injection rates of the charge carriers from the electrodes are denoted as n_i for electrons and p_i for holes. Charge carriers are driven out of the dielectric with drift rates: n_d for electrons and p_d for holes.

$$w_a = \frac{e^2 n_0^2 \mu_n L}{\epsilon J} = 8.5 \quad (5.6)$$

and

$$u_a \sim 1 \quad (5.7)$$

using a value of 10 for the dielectric constant. This value of u_a places the conduction in an Ohm's-law regime. This is also verified by the data in curve 1 of Fig. 4.17.

The subsequent variation of current with time takes place very slowly. The problem can be treated as a sequence of quasi-equilibrium states. Fig. 4.1 shows that the current decreases by a factor of 2 in about 40 min, and this requires a corresponding decrease in the trapped hole density. This is readily accounted for by a slow drift of the trapped holes (and their eventual removal at the cathode) with a concomitant failure of the anode to inject sufficient replacements, that is, $p_i < p_d$. This explanation would require a transit time for trapped holes of the order of 40 min which would correspond to a mobility of about $10^{-7} \text{ cm}^2/\text{Vs}$. The data of Fig. 4.10 showing an activation energy of 3.7 eV associated with τ_1 lead us to believe that the hole mobility is associated with this activation energy.

The subsequent large increase in current by a factor of 100 over the initial value requires, by the same argument, a similar increase in the trapped hole density. Since the increase must take place over many hours, it is proposed that hole injection from the anode is substantially increased by a slow accumulation of negatively charged ionic species (or vacancies) adjacent to that electrode. This is implied in Figs. 4.22, and 4.23. Using Poisson's equation it can be estimated that a constant ion density of $3.3 \times 10^{12}/\text{cm}^3$ in the region 25 μm thick adjacent

to the anode would double the field strength there. Checking once again with Eqs. (2.18) and (2.20), $w_a=0.085$ and $u_a \sim 0.4$. are obtained. These conditions show that the conduction departs from the Ohm's-law regime and approaches the square-law regime. This is verified by the data of Figs. 4.17 and 4.18 which show clearly a gradual transition from ohmic to square-law behavior some time after the application of an electric field of 1500 V/cm. Since Fig. 4.10 shows an activation energy of 2.3 eV associated with the time constant τ_2 , it can be assumed that the mobility of the ionic species in question is associated with the same activation energy.

The model also offers excellent explanations of the behavior on voltage reversal (Figs. 4.1 and 4.4) and removal and reapplication of voltage (Fig. 4.5). Since the trapped hole density is assumed to be quasi-steady at all times, and since it dictates the value of the free electron concentration and therefore the current, simple voltage reversal should result in the same current in the opposite direction; this is observed in the experiments illustrated in Figs. 4.1 and 4.4. Moreover, since the new anode is now only weakly injecting, the current should decay in a time of the order of the hole transit time before it builds up to a large value as the negatively charged ionic species (or vacancies) slowly accumulate near the new anode. If the voltage is removed for some time before being reapplied, it is expected that the concentration of charge carriers will decay towards its equilibrium value. Reapplication of the voltage should therefore cause a reduced current as observed in Fig. 4.5 ($I_i < I_{i0}$). Some idea of the rate of recombination that is required to explain the reduced current is given by the data shown in Fig. 4.6. If the voltage is reapplied in the same

direction, the current should subsequently increase since much of the negative ionic charge remains adjacent to the anode. For voltage reapplication in the opposite direction, the current should decrease before it again increases since the new anode now is not adjacent to the residual negative charge. These conclusions are also in agreement with the data of Figs. 4.4 and 4.5.

Both I_j and I_{SC} curves, which were both obtained after the current reached 18 mA, decayed very rapidly in the first minute and then followed by a slower decay till at $t \sim 15$ min, after that both curves decayed very slowly (Fig. 4.7). The first two decays (at $t < 15$ min) of both I_j and I_{SC} indicate that there are two types of electron-hole recombination processes. The slow decay process of either I_j or I_{SC} (at $t > 15$ min) is probably due to the relaxation of those negatively charged ionic species or vacancies accumulated near the anode. This conclusion is supported by the activation energy 2.4 eV obtained from I_{SC} at $t > 15$ min (Fig. 4.11) and that 2.3 eV from the time constant τ_2 of $I(t)$ (Fig. 4.10), which is responsible for the increase of the current leading to the breakdown.

Application of an ac voltage causes a current that is of similar magnitude to the initial current in the dc case; this is just what we would expect since the time of a voltage reversal is so short that none of the effects described above have time to begin. Fig. 4.12 shows that the ac conductivity follows an Arrhenius type law with an activation energy of 2.4 eV.

The activation energies obtained for different doped MgO crystals are believed to be partly related to the work functions of the charge carriers injected from electrodes into the dielectrics. This conclusion

is supported by the data shown in Table 4.5 where different values of activation energy have been obtained with the use of different electrode materials.

The idea that the ionic conduction resulted from the migration of Mg vacancies created by trivalent impurities (81-83) seems to be consistent with the results shown in Fig. 4.29. A higher concentration of Cr, which is mostly Cr^{3+} in MgO, has a greater effect on enhancing breakdown, since a high concentration of trivalent impurities produces a high concentration of Mg vacancies. A high concentration of Mg vacancies results in a greater field distortion near the anode and hence a higher hole injection level. Therefore, a higher concentration of trivalent impurities enhances the breakdown. The change in slope of the characteristic time for breakdown is assumed to result from association of the Cr ion with a free vacancy to form a less mobile associate. This is similar to that observed in the Sc-doped sample in Sempolinski's work (81). The suppression of the breakdown due to Cu or Co impurity may be explained by the following. Copper and cobalt impurities are in a divalent state in MgO crystals, which are usually reduced to a monovalent or zero state at high temperatures in the presence of an electric field. This reduction is called electrolytic coloration (2,79). The Mg vacancies will probably either associate with the reduced monovalent impurities and become relatively immobile species or be eliminated by this reduction process. The existence of Cu or Co impurity can effectively reduce the number of the Mg vacancies, and therefore suppresses the breakdown. This conclusion is not consistent with the results shown in Fig. 4.30. The existence of Ni impurity enhances the breakdown but

the enhancement of the breakdown is not monotonically proportional to its concentration.

5.3 Summary

The phenomenon of dielectric breakdown of MgO crystals at high temperatures (~ 1500 K) has been investigated with the use of a moderate electric fields (~ 1500 V/cm). The time dependence of the prebreakdown current behaviour has been determined to be represented by simple equation (Eq. 4.1) and the parameters of the equation have been determined (Eqs. 4.2, 4.3, and 4.5) and found to be very reproducible. The activation energies (Table 4.6) obtained from these parameters should be very useful for future theoretical calculations. The effect of various physical parameters associated with the breakdown, such as temperature, impurity concentration, sample thickness, electrode material, atmospheric conditions, electric field, and field strength, have been determined for the first time. A new model is proposed for the dielectric breakdown of MgO crystals at high temperatures. This model provides an excellent explanation of the main features of the experimental results. It has been found that the lifetime of MgO crystals, used as an electrical insulator at high temperatures, can be greatly prolonged by slightly doping MgO with Cu impurity (Fig. 4.27).

5.4 Suggestions for Future Work

The model proposed offers excellent explanations of the major features of the experimental results. Nevertheless, there are some questions which still remain unanswered, such as (1) how a specific impurity and its concentration affect the breakdown, and (2) how the breakdown process is affected by different atmospheres. In order to

answer these questions and verify the proposed model, some future experiments are suggested below:

(1) The measurement of the potential profiles should be refined. Primarily, more data points for each profile are needed. The potential profile must be determined accurately near the electrodes. In order to do this, a different experimental technique may be required.

(2) Studies to examine the effect of impurities on the breakdown should be extended to a wider range of dopants and should include some of the other transition metal impurities, such as Al, Sc, or Zn.

(3) A special technique, for example, high-temperature Electron Paramagnetic Resonance (EPR), must be used to investigate the existence of trapped electrons or holes in MgO crystals at high temperatures.

(4) Transmission electron microscopy (TEM) must be employed to study the microchange of the dielectric during the current growth.

(5) Experiments investigating the effect of atmosphere on the breakdown process should be repeated using a wider range of partial pressures of oxygen, for example, from 1 to 10^{-12} atm.

APPENDIX A

The temperature of the dielectric is described by the lattice energy balance equation Eq. (2.26)

$$C_V \frac{dT}{dt} - \text{div}(k\Delta T) = \sigma E^2 \quad . \quad (\text{A.1})$$

As mentioned in Sec. 2.1, the general solution of Eq. (A.1) is impossible to address. However, we are only interested in the simplified limiting case with the following assumptions:

(i) There is an infinite dielectric slab sandwiched by two parallel electrodes. This is a one-dimensional problem in which the coordinate x is measured from one electrode to the other.

(ii) The current is continuous inside the dielectric.

(iii) The electric field is uniform inside the dielectric. This condition gives the greatest temperature increase in the center of the dielectric, which will be discussed later.

(iv) The ambient temperature is zero.

Equation (A.1) is then reduced to

$$C_V \frac{\partial T}{\partial t} - k \frac{\partial^2 T}{\partial x^2} = I(t)V \quad (\text{A.2})$$

with two boundary conditions

$$T(0,t) = 0 \text{ and } T(\lambda,t) = 0 \quad (\text{A.3})$$

where $I(t)$ is the current at time t , V the applied voltage, λ the

spacing distance between two electrodes, and the value of $I(t)V$ is the energy gained per unit volume.

Taking into account the boundary conditions Eq. (A.3), we obtain, with the use of the method of separation of variables (32), the general homogeneous solution of Eq. (A.2) to be

$$T(x,t) = \sum a_n \exp(-n^2 \pi^2 kt / C_V \ell) \sin(n\pi x / \ell) , \quad (A.4)$$

where a 's are constants to be determined by initial conditions.

The solution of Eq. (A.2) can then be obtained with the use of the method of variation of parameters (32), that is to replace the constants a_n by unknown functions $C_n(t)$ and then determine these functions to satisfy both Eq. (A.2) and initial conditions. Since the exponential function of t can be absorbed into $C_n(t)$, we let the solution to Eq. (A.2) be

$$T(x,t) = \sum_{n=1}^{\infty} C_n(t) \sin(n\pi x / \ell) , \quad (A.5)$$

where

$$C_n(t) = \frac{2}{\ell} \int_0^{\ell} T(x,t) \sin(n\pi x / \ell) dx , \quad (A.6)$$

then the rest of the problem is to evaluate the values of $C_n(t)$.

Taking the time derivative of $C_n(t)$, we have

$$\frac{dC_n(t)}{dt} = \frac{2}{\ell} \int_0^{\ell} \frac{\partial T}{\partial t} \sin(n\pi x / \ell) dx . \quad (A.7)$$

Substituting Eq. (A.2) for $\frac{\partial T}{\partial t}$ into Eq. (A.7), we have

$$\frac{dC_n(t)}{dt} = \frac{2k}{\ell C_V} \int_0^{\ell} \frac{\partial^2 T}{\partial x^2} \sin \frac{n\pi x}{\ell} dx + \frac{2V}{\ell C_V} \int_0^{\ell} I(t) \sin \frac{n\pi x}{\ell} dx \quad (\text{A.8})$$

Integrating the right hand side terms of Eq. (A.8) individually by parts, we obtain

$$\frac{dC_n(t)}{dt} + \frac{k(n\pi)^2}{\ell^2 C_V} C_n(t) = \frac{4I(t)V}{n\pi C_V}, \quad n = \text{odd} \quad (\text{A.9})$$

which has the solution

$$C_n(t) = a_n e^{-n^2 t/\lambda} + \frac{4V}{n\pi C_V} \int_0^t I(\tau) e^{-n^2(t-\tau)/\lambda} d\tau \quad (\text{A.10})$$

where a's are constants, and $\lambda = \ell^2 C_V / \pi^2 k$.

From Eq. (4.1), we have

$$I(t) \sim I_0 2 \exp(t/\tau_2) \quad (\text{A.11})$$

at $t \gg 0$, as described in Sec. 4.1.1. Substituting Eq. (A.11) for $I(t)$ into Eq. (A.10), we obtain

$$C_n(t) = a_n e^{-n^2 t/\lambda} + \frac{4VI_0 2\lambda}{n\pi C_V [n^2 + (\lambda/\tau_2)]} \{e^{t/\tau_2} - e^{-n^2 t/\lambda}\} \quad (\text{A.12})$$

where $n = \text{odd number}$. At $t=t_0 \gg 0$, Eq. (A.12) is reduced to

$$C_n(t_0) < 4\lambda VI(t_0) / \pi C_V n^3 \quad (\text{A.13})$$

since $\lambda/\tau_2 \sim 10^{-5}$. Therefore, we obtain the maximum temperature at $t=t_0$ in the center of the dielectric

$$T(\ell/2, t_0) < 4\ell^2 I(t_0) V / \pi^3 k \sum_n (-1)^{(n-1)/2} / n^3 \quad (\text{A.14})$$

where $n = \text{odd number}$.

Let $I(t_0) = 18 \text{ mA}$, then Eq. (A.14) shows that the maximum temperature raised due to the joule heating inside the dielectric is

$$T(\frac{\ell}{2}, t_0) < 10 \text{ K} \quad (\text{A.15})$$

with the use of all the known values. Taking into account the nonuniform distribution of the electric field (Fig. 4.19) and the finite dimension of the dielectric, the maximum temperature increased inside the dielectric is expected to be much lower than 10 K which is less than 1% of the ambient temperature (1473 K) of the experiment. However, Eq. (A.14) indicates that the maximum temperature increased inside the dielectric is directly proportional to the current value. When the current is higher than 18 mA, the temperature in the dielectric would be significantly increased and the experimental condition would be also greatly changed.

LIST OF REFERENCES

1. Abraham, M. M., Butler, C.T., and Chen, Y. "Growth of High-Purity and Doped Alkaline Earth Oxides: I. MgO and CaO." *J. Chem. Phys.* 55, 3752-6, 1971.
2. Boatner, L. A., Modine, F. A., Abraham, M. M., Christie, W. H., and Negas, T. "Electrolytic Coloration of MgO at High Temperatures." *Bull. Am. Phys. Soc.* 24, 413, 1979.
3. Briggs, A. "Hydroxyl Impurity and the Formation and Distribution of Cavities in Melt-Grown MgO Crystals." *J. Mat. Sci.* 10, 729-36, 1975.
4. Calderwood, J. H., and Cooper, R. "Variation of the Electric Strength of KCl and NaCl Crystals with Temperature." *Proc. Phys. Soc. Lond.* B66, 74-80, 1953.
5. Callen, H. B. "Electric Breakdown in Ionic Crystals." *Phys. Rev.* 76, 1394-1402, 1949.
6. Chen, Y., Abraham, M. M., Templeton, L. C., and Unruh, W. P. "Role of Hydrogen and Deuterium on the V⁻Center Formation in MgO." *Phys. Rev.* B11, 881-90, 1975.
7. Chen, Y., Dudney, N., Narayan, J., and Orera, V. M. "Sub-Threshold [Li]^o Formation and Decoration of Strained Regions in Crystalline MgO." *Phil. Mag.* A44, 63-72, 1981.
8. Chen, Y., and Sibley, W. A. "Study of Ionization-Induced Radiation Damage in MgO." *Phys. Rev.* 154, 842-50, 1967.
9. Chen, Y., Trueblood, D. L., Schow, O. E., and Tohver, H. T. "Color Centers in Electron Irradiated MgO." *J. Phys.* C3, 2501-8, 1970.
10. Copple, C., Hartree, D. R., Porter, A., and Tyson, H. "The Evaluation of Transit Temperature Distributions in a Dielectric in an Alternating Field." *Inst. Elect. Engrs.* 85, 56-66, 1939.
11. Cooper, R., and Elliott, C. T. "Formative Process in the Dielectric Breakdown of Potassium Bromide." *Brit. J. Appl. Phys.* 17, 481-8, 1966.
12. Cooper, R., Grossart, D. T., and Wallace, A. A. "Directional Effects in the Electric Breakdown of Single Crystals of KCl and NaCl." *Proc. Phys. Soc., Lond. B* 70, 169-76, 1957.

13. Cooper, R., Higgin, R. M., and Smith, W. A. "The Influence of Ionic Conductivity on the Electric Strength of KCl and NaCl." Proc. Phys. Soc. Lond. B 76, 817-25, 1960.
14. Cooper, R., and Pulfrey, D. L. "Discharge Propagation Through Single Crystals of KBr." J. Appl. Phys. D4, 292-7, 1971.
15. Cooper, R., and Smith, W. A. "The Electric Breakdown of Sodium Chloride." Proc. Phys. Soc. Lond. B 78, 734-42, 1961.
16. Davies, M. O. "Transport Phenomena in Pure and Doped Magnesium Oxide." J. Chem. Phys. 38, 2047-55, 1963.
17. Emtage, P. R., and O'Dwyer, J. J. "Richardson-Schottky Effect in Insulator." Phys. Rev. 16, 356-8, 1966.
18. von Fock, V. "Zur Warmetheorie des Elektrischen Durchschlages." Arch. Elektrotech. 19, 71-81, 1927.
19. Forlani, F., and Minnaja, N. "Thickness Influence in Breakdown Phenomena of Thin Dielectric Films." Phys. Stat. Sol. 4, 311-24, 1964.
20. Fowler, R. H., and Nordheim, L. "Electron Emission in Intense Electric Fields." Proc. R. Soc. A 119, 173-81, 1928.
21. Frohlich, H. "Theory of Electrical Breakdown in Ionic Crystals." Proc. R. Soc. A 160, 230-41, 1937.
22. Frohlich, H. "On the Theory of Dielectric Breakdown in Solids." Proc. R. Soc. A 188, 521-32, 1947.
23. Frohlich, H., and Paranjape, B. V. "Dielectric Breakdown in Solids." Proc. Phys. Soc. Lond. B69, 21-32, 1956.
24. Goldsmith, A., Waterman, T. E., and Hirschborn, H. J. "Handbook of Thermophysical Properties of Solid Metals: Vol. III. Ceramics." Revised ed. p157-72, The Macmillan Co., New York, 1961.
25. Gonzalez, R., Chen, Y., and Tsang, K. L. "Diffusion of Deuterium and Hydrogen in Doped and Undoped MgO Crystals." Phys. Rev. B 26, 4637-45, 1982.
26. Good, R. H., and Muller, W. "Field Emission," Handbuch der Physik, 21, 176-231, 1956.
27. Hanscomb, J. R. "High Temperature Electrical Breakdown in Sodium Chloride." Aust. J. Phys. 15, 504-12, 1962.
28. Hanscomb, J. R. "Thermal Breakdown Caused by Field-Enhanced Conduction in Alkali Halides." J. Appl. Phys. D2, 1327-38, 1969.
29. Hanscomb, J. R. "Impurity and Time Effects in the Electrical Breakdown of Alkali Halides." J. Appl. Phys. 41, 3597-3604, 1970.

30. Hanscomb, J. R., Kao, K. C., Calderwood, J. H. O'Dwyer, J. J., and Emtage, P. R. "High-Field Conduction in Alkali Halide Crystals." *Proc. Phys. Soc.* 88, 425-35, 1966.
31. Hartman, T. E., and Chivian, J. S. "Electron Tunneling Through Thin Aluminum Oxide Films." *Phys. Rev. A* 134, 1094-1101, 1964.
32. Hildebrand, F. B. Advanced Calculus for Applications. 484-90, Prentice-Hall Inc., New Jersey, 1963.
33. von Hippel, A. "Der elektrische Durchschlag in Gasen und festen Isolatoren." *Ergebn, Exakt. Naturw.* 14, 79-129, 1935.
34. von Hippel, A., and Alger, R. S. "Breakdown of Ionic Crystals by Electron Avalanches." *Phys. Rev.* 76, 127-33, 1949.
35. Hughes, A. E., and Jain, S. C. "Metal Colloids in Ionic Crystals." *Adv. Phys.* 28, 717-828, 1979.
36. Inouye, H., Liu, C. T., and Donnelly, R. G. "New Platinum-Rhodium-Tungsten Alloys for Space Isotopic Heat Sources." ORNL-4813, 19-22, 1972.
37. Iverson, M. V., Windscheif, J. C., and Sibley, W. A. "Optical Parameters for the MgO:Ni²⁺ Laser System." *Appl. Phys. Lett.* 36, 183-4, 1980.
38. Jain, S. C., and Jain, V. K. "Optical and Electrical Studies of Colloidal and F-Aggregate Centers in Highly Pure KBr Crystals." *Phys. Rev.* 181, 1312-8, 1969.
39. Jain, S. C., and Sootha, G. D. "Electronic Conduction in Additively Colored KCl Crystals." *J. Phys. Chem. Solids* 26, 267-72, 1965.
40. Jain, S. C., and Sootha, G. D. "Optical, Electron-Spin-Resonance, and Electrical Studies of Colloidal and F-Aggregate Centers in Highly Pure KCl Crystals. I. Colloidal Centers." *Phys. Rev.* 171, 1075-82, 1968.
41. Kantrowitz, A. "The First 20 Years of MHD Development." ANL-77-21, 289-92, 1977.
42. Kingery, W. D., Bowen, H. K., and Uhlman, D. R. Introduction to Ceramics. 2nd ed. 217-57, Wiley, New York, 1976.
43. Lamb, D. R. Electrical Conduction Mechanisms in Thin Insulating Films. 1-114, Methuen, London, 1967.
44. Lampert, M. A. "Simplified Theory of Space-Charge-Limited Currents in an Insulator with Traps." *Phys. Rev.* 103, 1648-56, 1956.
45. Lampert, M. A. "Simplified Theory of One-Carrier Currents with Field-Dependent Mobilities." *J. Appl. Phys.* 29, 1082-90, 1958.

46. Lampert, M. A. "Double Injection in Insulators." *Phys. Rev.* 125, 126-41, 1962.
47. Lampert, M. A. "Volume-Controlled Current Injection in Insulators." *Rep. Progr. Phys.* 27, 329-67, 1964.
48. Lampert, M. A., and Mark, P. Current Injection in Solids. 1-351, Academic Press, New York, 1970.
49. Lampert, M. A., and Rose, A. "Volume-Controlled, Two-Carrier Currents in Solids: The Injected Plasma Case." *Phys. Rev.* 121, 26-37, 1961.
50. Lenzlinger, M., and Snow, E. H. "Fowler-Nordheim Tunneling into Thermally Grown SiO₂." *J. Appl. Phys.* 40, 278-83, 1969.
51. Lewis, T. J., and Wright, A. J. "The Electrical Conductivity of Magnesium Oxide at Low Temperatures." *J. Appl. Phys.* D1, 441-7, 1968.
52. Lewis, T. J., and Wright, A. J. "The Electrical Conductivity of Magnesium Oxide at High Fields." *J. Appl. Phys.* D3, 1329-39, 1970.
53. Liu, C. T., and Inouye, H. "Study of Iridium-Tungsten Alloys for Space Radioisotopic Heat Sources," ORNL-5240, 30-7, 1976.
54. McClure, D. S. "Optical Spectra of Transition-Metal Ions in Corundum." *J. Chem. Phys.* 36, 2757-79, 1962.
55. Miller, A., and Abrahams, E. "Impurity Conduction at Low Concentrations." *Phys. Rev.* 120, 745-55, 1960.
56. Milnes, A. G. Deep Impurities in Semiconductors. 300, Wiley, New York, 1973.
57. Mitoff, S. P. "Electrical Conductivity of Single Crystals of MgO." *J. Chem. Phys.* 31, 1261-9, 1959.
58. Mitoff, S. P. "Electronic and Ionic Conductivity in Single Crystals of MgO." *J. Chem. Phys.* 36, 1383-9, 1962.
59. Mitoff, S. P. "Bulk Versus Surface Conductivity of MgO Crystals." *J. Chem. Phys. Lett.* 41, 2561-2, 1964.
60. Mochizuki, S., and Sakurai, T. "Electrical Conduction of MgO Doped with Cr at High Temperatures in Oxidizing Atmosphere." *Phys. Stat. Sol.* 41, 411-5, 1977.
61. Modine, F. A. "Magneto-Optical Study of a Charge-Transfer Band in Vanadium-Doped MgO." *Phys. Rev.* B8, 854-63, 1973.
62. Modine, F. A., Boatner, L. A., Abraham, M. M., Unruh, W. P., and Bunch, R. "Optical Studies of Electrolytically-Colored MgO." *Bull. Am. Phys. Soc.* 24, 413, 1979.

63. Moon, P. H. "The Theory of Thermal Breakdown of Solid Dielectrics." *Trans. Am. Inst. Elect. Engrs.* 50, 1008-21, 1931.
64. Mott, N. F. "On the Transition to Metallic Conduction in Semiconductors." *Canad. J. Phys.* 34, 1356-68, 1956.
65. Mott, N. F. "The Transition to the Metallic State." *Phil. Mag.* 6, 287-309, 1961.
66. Mott, N. F., and Gurney, R. W. Electronic Process in Ionic Crystals. 109-197, Oxford Univ. Press, Oxford, London, 1948.
67. Mycielski, J. "Mechanism of Impurity Conduction in Semiconductors." *Phys. Rev.* 122, 99-103, 1961.
68. Narayan, J., and Chen, Y. "Characterization of Defects in Nickel-Doped MgO Crystals." *J. Appl. Phys.* 51, 1242-3, 1980.
69. Narayan, J., Chen, Y., and Moon, R. M. "Nickel Colloids in Reduced Nickel-Doped Magnesium Oxide." *Phys. Rev. Lett.* 46, 1491-4, 1981.
70. Narayan, J., Weeks, R. A., and Sonder, E. "Aggregation of Defects and Thermal-Electric Breakdown in MgO." *J. Appl. Phys.* 49, 5977-81, 1978.
71. O'Dwyer, J. J. "The Theory of Avalanche Breakdown in Solid Dielectrics." *J. Phys. Chem. Solids* 28, 1137-44, 1967.
72. O'Dwyer, J. J. The theory of Electrical Conduction and Breakdown in Solid Dielectrics. 1-309, Oxford Univ. Press, Oxford, London, 1973.
73. Oishi, Y., and Kingery, W. D. "Oxygen Diffusion in Periclase Crystals." *J. Chem. Phys.* 33, 905-6, 1960.
74. Osburn, C. M., and Vest, R. W. "Electrical Properties of Single Crystals, Bicrystals, and Polycrystals of MgO." *J. Am. Ceram. Soc.* 54, 428-35, 1971.
75. Paracchini, C. "Light Emission at a Metal-Insulator Contact under High Electric Fields." *Phys. Rev.* B4, 2342-7, 1971.
76. Pollack, S. R. "Schottky Field Emission Through Insulating Layers." *J. Appl. Phys.* 34, 877-80, 1963.
77. Rose, A. "An Outline of Some Photoconductive Processes." *RCA Rev.* 12, 362-414, 1951.
78. Rose, A. "Space-Charge-Limited Currents in Solids." *Phys. Rev.* 97, 1538-44, 1955.
79. Schulman, J. H., and Compton, W. D. Color Centers in Solids. 34-8, McMillan Co., New York, 1962.

80. Seitz, F. "On the Theory of Electron Multiplication in Crystals." *Phys. Rev.* 76, 1376-93, 1949.
81. Sempolinski, D. R. "The High Temperature Electrical Properties of Single Crystalline Magnesium Oxide." Ph.D. Thesis. Massachusetts Institute of Technology, 1979.
82. Sempolinski, D. R., and Kingery, W. D. "Ionic Conductivity and Magnesium Vacancy Mobility in Magnesium Oxide." *J. Am. Ceram. Soc.* 63, 664-9, 1980.
83. Sempolinski, D. R., Kingery, W. D., and Tuller, H. L. "Electronic Conductivity of Single Crystalline Magnesium Oxide." *J. Am. Ceram. Soc.* 63, 669-75, 1980.
84. Smith, J. L., and Budenstein, P. P. "Dielectric Breakdown in Thin Evaporated Films of CaF_2 , MgF_2 , NaF , and LiF ." *J. Appl. Phys.* 40, 3491-8, 1969.
85. Sonder, E., Kelton, K. F., Pigg, J. C., and Weeks, R. A. "The Effect of Electric Current on the Conductivity of MgO Single Crystals at Temperatures above 1300K." *J. Appl. Phys.* 49, 5971-6, 1978.
86. Soshea, R. W., Dakker, A. J., and Sturtz, J. P. "X-Ray-Induced Color Center in MgO ." *J. Phys. Chem. Solids* 5, 23-33, 1958.
87. Stratton, R. "The Theory of Dielectric Breakdown in Solids." *Progr. Dielectrics* 3, 235-90, 1961.
88. Stratton, R. "Volt-Current Characteristics for Tunneling Through Insulating Films." *J. Phys. Chem. Solids* 23, 1177-90, 1962.
89. Surplice, N. A., and Jones, R. P. "The Thermoelectric Power and Electrical Conductivity of Calcium and Magnesium Oxides." *Brit. J. Appl. Phys.* 15, 639-42, 1964.
90. Tsang, K. L., Chen, Y., and O'Dwyer, J. J. "High Field Conduction and Dielectric Breakdown in Nominally Pure and Nickel-Doped MgO Crystals at High Temperatures." *Phys. Rev.* B26, 6909-17, 1982.
91. Tsang, K. L., and Chen, Y. "Suppression of Dielectric Breakdown in MgO Crystals at High Temperatures by Impurity Doping." Submitted to *J. Appl. Phys.* Mar. 1983.
92. Walther, G. C. and Hench, L. L. "Dielectric Breakdown of Ceramics." from Physics of Electronic Ceramics. Part A, 539-64, Marcel Dekker, Inc., New York, 1971.
93. Watson, D. B., and Heyes, W. "Time Lags in the Breakdown of NaCl at High Temperatures." *J. Phys. Chem. Solids* 31, 2531-7, 1970.

94. Weeks, R. A., Narayan, J., and Sonder, E. "Electric Breakdown in MgO Crystals at Elevated Temperatures." *Phys. Stat. Sol.* 70, 631-9, 1982.
95. Weeks, R. A., Sonder, E., Pigg, J. C., and Kelton, K. F. "Reduction of Impurity Ions in MgO by Current Flow at High Temperature." *J. Phys. Suppl.* C7, 411-4, 1976.
96. Whitehead, S. Dielectric Breakdown of Solids. 115-162, Oxford Univ. Press, Oxford, London, 1951.
97. Wuensch, B. J., and Vasilos, T. "Diffusion of Transition Metal Ions in Single-Crystal MgO." *J. Chem. Phys.* 36, 2917-22, 1962.
98. Zener, C. "A Theory of the Electrical Breakdown of Solid Dielectrics." *Proc. R. Soc.* A145, 523-9, 1934.

VITA

PERSONAL DATA:

NAME: KING-LONG TSANG; SEX: Male
BORN: Taiwan, Republic of China, December 15, 1949
MARITAL STATUS: Married to JEAN SHU-TZ CHIEN on March 7, 1980
CHILDREN: ANGELA YU-ZU TSANG

EDUCATION:

1980-83 University of Alabama in Birmingham, Ph.D. (Physics)
1978-80 University of Alabama in Birmingham, M.S. (Physics)
1977-78 Florida Institute of Technology, (Physics, Computer Science)
1973-77 Soo-Chow University, Taipei, Taiwan, B.S. (Physics)

HONORS:

1980-82 Ph.D. Thesis Research, Oak Ridge National Laboratory
1980 The Best Student of the Year, Physics Dept., U. A. B.
1980- Member of the Alabama Academy of Science
1979-83 Fellowship sponsored by the Graduate School of U. A. B.
1978-79 Teaching Assistantship, Physics Dept., U. A. B.
1977-78 Teaching Assistantship, Physics Dept., F. I. T.
1974-77 Tuition Scholarship, Soo-Chow University, Taiwan

RESEARCH AND PROFESSIONAL EXPERIENCES:

1980-83: Solid State Division, Oak Ridge National Laboratory

1. The Dielectric Breakdown of MgO Crystals at High Temperatures.
2. Hydrogen and Deuterium Diffusion in Oxides (MgO, TiO₂, LiNbO₃, Spinel, Cordierites, etc.).
3. Optical and Diffusive Properties of MgO and LiNbO₃ Crystals.
4. Radiation Damages on Oxides.
5. TEM Study on MgO Crystals.
6. Computer Simulation of Electro-Optical Images.

1979-80 Research Assistant: Optimum Electrode Design for R. F. Hyperthermia Therapy. Department of Physics, U. A. B.
1978-79 Teaching Assistant: Responsible for teaching undergraduate labs and General Physics. Department of Physics, U. A. B.
1977-78 Teaching Assistant: Responsible for teaching undergraduate labs. Department of Physics, F. I. T.
1973-77 Part-time tutor

VITA (continued)

PUBLICATIONS:

1. K. L. Tsang and Y. Chen, "Electrothermal Breakdown of MgO Crystals at High Temperatures," ORNL-5850, 185-7, 1981.
2. R. Gonzalez, Y. Chen, K. L. Tsang, and G. P. Summers, "The Diffusion of Deuterium and Hydrogen in Crystalline LiNbO_3 ," Appl. Phys. Lett. 41, 739-41, 1982.
3. R. Gonzalez, Y. Chen, and K. L. Tsang, "Diffusion of Deuterium and Hydrogen in Doped and Undoped MgO Crystals," Phys. Rev. B, 26, 4637-45, 1982.
4. K. L. Tsang, Y. Chen, and J. J. O'Dwyer, "High Electric Field Conduction and Dielectric Breakdown of MgO Crystals at High Temperatures," Phys. Rev. B26, 6909-17, 1982.
5. K. L. Tsang and Y. Chen, "Suppression of the Dielectric Breakdown in MgO Crystals at High Temperatures by Impurity Doping," to be published in J. Appl. Phys., Aug., 1983.
6. Y. Chen, R. Gonzalez, and K. L. Tsang, "Diffusion of Deuterium and Hydrogen in TiO_2 Crystals Enhanced by Ionizing Radiation and Electric Field," (To be submitted for publication in Phys. Rev. Lett.).
7. R. Gonzalez, K. L. Tsang, and Y. Chen, "Diffusion of Deuterium and Hydrogen in Amorphous Cordierites," (To be submitted for publication in J. Am. Ceram. Soc.).

MEETINGS AND CONFERENCES:

1. Y. Chen, J. Narayan, and K. L. Tsang, "Threshold Temperature for Formation of Metallic Nickel Colloids in MgO Crystal," Bull. Am. Phys. Soc. 26, 268, 1981.
2. J. L. Boldu, K. L. Tsang, and Y. Chen, "Optical Studies on Irradiated Ni-Doped MgO Crystals," Bull. Am. Phys. Soc. 26, 1200, 1981.
3. K. L. Tsang and Y. Chen, "Mechanism for Electrothermal Breakdown in Nickel-Doped MgO Crystals at High Temperatures," Bull. Am. Ceram. Soc. 61, 414, 1982.
4. Y. Chen, R. Gonzalez, and K. L. Tsang, "Radiation and Electric Field Induced Diffusion of Deuterium and Hydrogen in TiO_2 at Low Temperatures," Bull. Am. Phys. Soc. 28, 494, 1983.

GRADUATE SCHOOL
UNIVERSITY OF ALABAMA IN BIRMINGHAM
DISSERTATION APPROVAL FORM

Name of Candidate King-Long Tsang

Major Subject Physics

Title of Dissertation THE DIELECTRIC BREAKDOWN OF MgO CRYSTALS
AT HIGH TEMPERATURES

Dissertation Committee:

Fred T. T. T. T., Chairman _____

Ivan A. Pterovich _____

Edward L. Hill _____

Donald Eisen _____

John N. Namy
Director of Graduate Program _____

Dean, UAB Graduate School John N. Namy

Kenneth Gozzen

Date Dec 10/82